

# Prosthetic Control and Sensory Feedback for Upper Limb Amputees

THÈSE N° 8816 (2018)

PRÉSENTÉE LE 19 JUILLET 2018

À LA FACULTÉ DES SCIENCES ET TECHNIQUES DE L'INGÉNIEUR  
LABORATOIRE DE CIRCUITS INTÉGRÉS  
PROGRAMME DOCTORAL EN MICROSYSTÈMES ET MICROÉLECTRONIQUE

ÉCOLE POLYTECHNIQUE FÉDÉRALE DE LAUSANNE

POUR L'OBTENTION DU GRADE DE DOCTEUR ÈS SCIENCES

PAR

Huaiqi HUANG

acceptée sur proposition du jury:

Prof. C. Dehollain, présidente du jury  
Prof. C. Enz, Prof. V. M. Koch, directeurs de thèse  
Dr J. Farserotu, rapporteur  
Prof. C. Antfolk, rapporteur  
Dr C. Bruschini, rapporteur



ÉCOLE POLYTECHNIQUE  
FÉDÉRALE DE LAUSANNE

Suisse  
2018



Wings are a constraint that makes  
it possible to fly.  
— Robert Bringhurst

To my parents...



# Acknowledgements

First of all, I would like to thank my thesis adviser and co-adviser, Prof. Christian Enz and Prof. Volker M. Koch, who have given me continuous support throughout my thesis work. They have motivated me and taught me critical thinking.

During my research, I must also thank Dr. Claudio Bruschini, who has been most patient and encouraging, and guided my work throughout these years.

Moreover, I would also like to thank Prof. Christian Antfolk, who helped me to start this new direction in my research and kept providing me with fresh research ideas and offered me a chance to visit his lab in Lund University to conduct experiments.

Then, I want to thank the whole WiseSkin team: Prof. John Farserotu, Prof. Jean-Dominique Decotignie, Prof. Stephanie Lacour, Prof. Jörn Justiz, Dr. Hadrien Michaud, Camilo Rojas, Dr. Tao Li, Dr. Elena Daskalaki and Dr. Vladimir Kopta. The WiseSkin team has fully supported me for the system integration and the testing.

I would also like to thank my colleagues and friends from ICLAB and Biomedical Engineering Lab: Alessandro, Antonino, Arnout, Adrien, Anurag, Assim, Chunming, Farzan, Francesco, Jérémy, Maria-Anna, Mattia, Vladimir, Vincent, Romain, Raghav, and Raffaele, for their support, help, and friendship. I am also appreciating all the administrative help I received from Lysiane Bourquin, Sandrine Piffaretti, Lucie Auberson, Sylvie Nobs, Christine Treutner, and Marie Halm.

Finally, I would like to thank my parents, who has given me life and unconditional love. Last but not the least, I want to thank my husband, Oliver Spang, who fills my life with joy.

*Neuchatel, 11.05 2018*

Huaiqi Huang.



# Abstract

Hand amputation could dramatically degrade the life quality of amputees. Many amputees use prostheses to restore part of the hand functions. Myoelectric prosthesis provides the most dexterous control. However, they are facing high rejection rate. One of the reasons is the lack of sensory feedback. There is a need for providing sensory feedback for myoelectric prosthesis users. It can improve object manipulation abilities, enhance the perceptual embodiment of myoelectric prostheses and help reduce phantom limb pain. This PhD work focuses on building bi-directional prostheses for upper limb amputees.

In the introduction chapter, first, an overview of upper limb amputee demographics and upper limb prosthesis is given. Then the human somatosensory system is briefly introduced. The next part reviews invasive and non-invasive sensory feedback methods reported in the literature. The rest of the chapter describes the motivation of the project and the thesis organization.

The first step to build a bi-directional prostheses is to investigate natural and robust multifunctional prosthetic control. Most of the commercial prostheses apply non-pattern recognition based myoelectric control methods, which offers only limited functionalities. In this thesis work, pattern recognition based prosthetic control employing three commonly used and representative machine learning algorithms is investigated. Three datasets involving different levels of upper arm movements are used for testing the algorithm effectiveness. The influence of time-domain features, window and increment sizes, algorithms, and post-processing techniques are analyzed and discussed.

The next three chapters address different aspects of providing sensory feedback. The first focus of sensory feedback process is the automatic phantom map detection. Many amputees have referred sensation from their missing hand on their residual limbs (phantom maps). This skin area can serve as a target for providing amputees with non-invasive tactile sensory feedback. One of the challenges of providing sensory feedback on the phantom map is to define the accurate boundary of each phantom digit because the phantom map distribution varies from person to person. Automatic phantom map detection methods based on four decomposition support vector machine algorithms and three sampling methods are proposed. The accuracy and training/ classification time of each algorithm using a dense stimulation array and two coarse stimulation arrays are presented and compared.

The next focus of the thesis is to develop non-invasive tactile display. The design and psychophysical testing results of three types of non-invasive tactile feedback arrays are presented: two with vibrotactile modality and one with multi modality. For vibrotactile, two types of

## Acknowledgements

---

miniaturized vibrators: eccentric rotating masses (ERMs) and linear resonant actuators (LRAs) were first tested on healthy subjects and their effectiveness was compared. Then the ERMs are integrated into a vibrotactile glove to assess the feasibility of providing sensory feedback for unilateral upper limb amputees on the contralateral hand. For multimodal stimulation, miniature multimodal actuators integrating servomotors and vibrators were designed. The actuator can be used to deliver both high-frequency vibration and low-frequency pressures simultaneously. By utilizing two modalities at the same time, the actuator stimulates different types of mechanoreceptors and thus has the potential to increase the band width to transfer tactile information.

The tactile displays are then integrated into sensory feedback systems, which consist of pressure sensors, processing units, communication modules, and the tactile feedback arrays. Pilot experiments have been conducted with amputees and/or healthy subjects in both passive multi-site tactile stimuli discrimination tasks and active objects manipulation tasks. Experimental results demonstrate that the tactile sensory feedback system have positive impacts on the functionality of the hand prosthesis.

Key words: Sensory feedback, Myoelectric prosthetic control, Pattern recognition, Non-invasive sensory substitution, Hand amputees, Upper Limb Prostheses

# Zusammenfassung

Eine Handamputation kann die Lebensqualität von Amputierten dramatisch verschlechtern. Viele Amputierte verwenden Prothesen, um einen Teil der Handfunktionen wiederherzustellen. Myoelektrische Prothese bieten zwar die beste Kontrolle, jedoch besteht immer noch eine hohe Ablehnungsrate. Einer der Gründe ist die fehlende sensorische Rückmeldung. Ein funktionierendes sensorisches Feedback für Nutzer von myoelektrischen Prothesen kann die Objektmanipulationsfähigkeiten verbessern, die wahrnehmbare Verkörperung von der Prothese verbessern und dazu beitragen, Phantomschmerzen zu reduzieren. Diese Doktorarbeit konzentriert sich auf den Aufbau von bidirektionalen Prothesen für Amputierte der oberen Gliedmaßen.

Im Einführungskapitel wird zunächst ein Überblick über die Demographie von Amputierten der oberen Extremitäten gegeben und die verschiedenen Arten von Armprothese behandelt. Außerdem wird das menschliche somatosensorische System kurz vorgestellt. Der nächste Teil behandelt invasive und nicht-invasive sensorische Feedback-Methoden, die in der Literatur beschrieben werden. Der Rest des Kapitels beschreibt die Motivation des Projekts und die Organisation der Arbeit.

Der erste Schritt zum Aufbau einer bidirektionalen Prothese ist die zuverlässige und robuste multifunktionale prothetische Kontrolle. Die meisten kommerziellen Prothesen verwenden keine mustererkennungsbasierten myoelektrischen Steuerverfahren, die nur begrenzte Funktionalitäten bereitstellen. In dieser Arbeit wird die prothetische Kontrolle auf der Grundlage von Mustererkennung, unter Verwendung von drei häufig verwendeten und repräsentativen Algorithmen für das maschinelle Lernen, untersucht. Drei Datensätze mit verschiedenen Ebenen der Oberarmbewegungen werden zum Testen der Algorithmuswirksamkeit verwendet. Der Einfluss von Zeitbereichsmerkmalen, Fenster- und Inkrementgrößen sowie Algorithmen wird analysiert und diskutiert.

Die nächsten drei Kapitel befassen sich mit verschiedenen Aspekten der sensorischen Rückmeldung. Der erste Schwerpunkt des sensorischen Feedbackprozesses ist die automatische Phantomkartenerkennung. Viele Amputierte haben die Empfindung ihrer fehlenden Hand auf ihren verbleibenden Gliedmaßen übertragen (Phantomkarte). Dieser Bereich des Armes kann genutzt werden, Amputierten nicht-invasive fühlbare sensorische Rückkopplungen zu geben. Eine der Herausforderungen von sensorischem Feedback auf der Phantomkarte besteht darin, die genaue Grenze jedes Phantombereichs zu definieren, da die Phantomkartenverteilung von Person zu Person variiert. Es werden automatische Phantomkartenerkennungsverfahren vorgeschlagen, die auf vier „decomposition support vector machine“ Algorithmen und drei

## Acknowledgements

---

Abtastverfahren basieren. Die Genauigkeit und Trainings- / Klassifizierungszeit jedes Algorithmus, der ein dichtes und zwei grobe Stimulationsarrays verwendet, werden präsentiert und verglichen.

Ein weiterer Schwerpunkt der Arbeit ist die Entwicklung eines nicht-invasiven taktilen Rückmeldesystems. Das Design und die psychophysischen Testergebnisse von drei Arten von nichtinvasiven taktilen Feedback-Arrays werden vorgestellt: zwei mit vibrotaktilen Verfahren und eines mit multimodaler Stimulation. Für die Vibrationsverfahren wurden zwei Arten von miniaturisierten Vibratoren getestet: exzentrisch rotierende Massen (ERMs) und linear resonant Aktuatoren (LRAs) wurden zuerst an gesunden Probanden getestet und ihre Wirksamkeit wurde verglichen. Danach wurden die ERM in einen vibrotaktilen Handschuh integriert, um die Möglichkeit einer sensorischen Rückmeldung für einseitig Oberarmamputierte an der kontralateralen Hand zu beurteilen. Für die multimodale Stimulation wurden miniaturisierte multimodale Aktuatoren mit Servomotoren und Vibratoren entwickelt. Der Aktuator kann verwendet werden, um sowohl hochfrequente Vibrationen als auch niederfrequente Drücke gleichzeitig zu erzeugen. Durch die simultane Verwendung von zwei Modalitäten stimuliert der Aktuator verschiedene Arten von Mechanorezeptoren und hat somit das Potenzial, die Bandbreite zu erhöhen, um taktile Informationen zu übertragen.

Die taktilen Rückmeldesysteme wurden im Rahmen dieser Arbeit in sensorische Feedback-Systeme integriert. Das sensorische Rückmeldesystem besteht aus Drucksensoren, Verarbeitungseinheiten, Kommunikationsmodulen und den taktilen Feedback-Arrays. Es wurden Pilotexperimente mit Amputierten und/oder gesunden Probanden sowohl für passive Tastsimulationsaufgaben als auch für Manipulationsaufgaben mit aktiven Objekten durchgeführt. Experimentelle Ergebnisse zeigen, dass das taktile sensorische Rückkopplungssystem positive Auswirkungen auf die Funktionalität der Handprothese hat.

**Stichwörter:** Sensorische Rückkopplung, Myoelektrische prothetische Kontrolle, Mustererkennung, nicht-invasive sensorische Substitution, Handamputierte, Prothesen der oberen Extremitäten

# Contents

<b>Acknowledgements</b>	<b>i</b>
<b>Abstract (English/Français/Deutsch)</b>	<b>iii</b>
<b>List of figures</b>	<b>xi</b>
<b>List of tables</b>	<b>xvii</b>
<b>1 Introduction</b>	<b>1</b>
1.1 Upper limb amputees and upper limb prostheses . . . . .	1
1.2 Somatosensory system . . . . .	6
1.2.1 The sense of touch . . . . .	7
1.2.2 Proprioceptive sensory system . . . . .	7
1.3 Sensory feedback: state-of-the-art . . . . .	8
1.3.1 Invasive sensory feedback . . . . .	8
1.3.2 Targeted muscle reinnervation . . . . .	11
1.3.3 Non-invasive sensory feedback . . . . .	11
1.3.4 Thermal feedback . . . . .	15
1.3.5 Proprioceptive sensory feedback . . . . .	16
1.4 WiseSkin . . . . .	16
1.5 Thesis organization . . . . .	16
<b>2 Myographic Signal Pattern Recognition for Prosthetic Control</b>	<b>19</b>
2.1 Introduction . . . . .	19
2.2 EMG classification algorithms . . . . .	24
2.2.1 Linear discriminant analysis . . . . .	24
2.2.2 Support vector machines . . . . .	25
2.2.3 Deep belief network . . . . .	26
2.3 Decomposition methods to construct multiclass classifiers . . . . .	26
2.4 Methods . . . . .	27
2.4.1 Datasets description . . . . .	27
2.4.2 Classification setup . . . . .	28
2.4.3 Evaluation methods . . . . .	30
2.5 Classification results . . . . .	31

## Contents

---

2.5.1	Feature selection . . . . .	31
2.5.2	Influence of window and increment sizes . . . . .	31
2.5.3	Influence of classification algorithms . . . . .	35
2.5.4	Techniques to improve classification accuracy with unbalanced training data . . . . .	35
2.5.5	Influence of principle component analysis . . . . .	36
2.5.6	Post-processing . . . . .	38
2.6	Summary . . . . .	39
<b>3</b>	<b>Automatic Hand Phantom Map Generation and Detection</b>	<b>41</b>
3.1	Hand phantom map introduction . . . . .	41
3.2	Hand phantom map databases . . . . .	44
3.2.1	Hand phantom map model generation . . . . .	44
3.2.2	Database from reported phantom map images . . . . .	46
3.3	Sampling methods . . . . .	47
3.3.1	Random sampling (RS) . . . . .	48
3.3.2	Systematic sampling (SS) . . . . .	48
3.3.3	Majority pooling sampling (MPS) . . . . .	48
3.4	Support vector machines in phantom map detection . . . . .	50
3.4.1	Fuzzy support vector machine . . . . .	50
3.4.2	Active learning support vector machine . . . . .	53
3.5	Results and discussion . . . . .	54
3.5.1	Simulation setup . . . . .	55
3.5.2	Accuracy . . . . .	56
3.5.3	Timing . . . . .	64
3.6	Conclusion . . . . .	65
<b>4</b>	<b>Non-invasive Tactile Display: Design and Testing</b>	<b>71</b>
4.1	Introduction . . . . .	71
4.1.1	Non-invasive tactile display: state-of-the-art . . . . .	71
4.1.2	Psychophysical measurement methods . . . . .	73
4.2	Psychophysical investigation of two types of vibrotactile devices . . . . .	75
4.2.1	Experimental materials . . . . .	76
4.2.2	Subjects . . . . .	77
4.2.3	Experimental procedure . . . . .	77
4.2.4	Results . . . . .	79
4.2.5	Discussion . . . . .	82
4.2.6	Summary . . . . .	86
4.3	Multimodal tactile display . . . . .	86
4.3.1	Multimodal stimulation device . . . . .	86
4.3.2	Experimental procedure . . . . .	87
4.3.3	Experimental results and discussion . . . . .	88
4.3.4	Summary . . . . .	89

4.4	Summary . . . . .	90
<b>5</b>	<b>Sensory feedback system: design and testing</b>	<b>91</b>
5.1	Introduction . . . . .	91
5.1.1	Proprioceptive and exteroceptive sensing for prostheses . . . . .	91
5.1.2	Non-invasive sensory feedback outcome measures . . . . .	95
5.2	WiseSkin: a vibrotactile sensory feedback system with a wireless sensor network	97
5.2.1	System description . . . . .	97
5.2.2	Experiments . . . . .	102
5.2.3	Summary . . . . .	103
5.3	Multi-modal, multi-site sensory feedback system for upper limb amputees . . .	104
5.3.1	System integration . . . . .	104
5.3.2	Experiments . . . . .	109
5.3.3	Summary . . . . .	111
5.4	Single-site vibrotactile sensory feedback system . . . . .	111
5.4.1	System description . . . . .	111
5.4.2	Solenoid actuator . . . . .	113
5.4.3	Experiments . . . . .	113
5.4.4	Summary . . . . .	117
5.5	Conclusion . . . . .	117
<b>6</b>	<b>Conclusions</b>	<b>119</b>
6.1	Summary of the thesis work . . . . .	119
6.1.1	EMG classification . . . . .	119
6.1.2	Automatic phantom map detection . . . . .	120
6.1.3	Non-invasive tactile displays . . . . .	120
6.1.4	Sensory feedback system integration and testing . . . . .	121
6.2	Outlook . . . . .	121
	<b>Curriculum Vitae</b>	<b>149</b>



# List of Figures

1.1	Illustration of amputation levels [2] . . . . .	2
1.2	Examples of (a) a cosmetic prosthesis, (b) a body-powered prosthesis [7], and (c) a myoelectric prosthesis [21] . . . . .	3
1.3	Classifications of myoelectric control methods . . . . .	5
1.4	State diagram of i-Limb prostheses control [49]. The architecture consists of six states corresponding to the six target postures, excluding hand gestures (resting phase). E represents extension, F represents flexion, and T represents a trigger command (combined flexion and extension EMG signals that is greater than a tuned threshold). A trigger (T) iteratively changes states in a specified order. . . . .	5
1.5	Procedure of pattern recognition based prosthetic control. . . . .	6
1.6	The mechanoreceptors in the human skin [60]. . . . .	7
1.7	The tradeoff of invasiveness and selectivity of some commonly used implantable electrodes for bidirectional interfacing with the prostheses. FINE is short for flat interface nerve electrode, LIFE is short for longitudinal intrafascicular electrode, TIME is short for transverse intrafascicular multichannel electrode, and MEA is short for microelectrode array [81]. . . . .	10
1.8	The schematic of targeted muscle reinnervation surgery. The reinnervated nerves residing on the chest provide both the control sites and the sensory feedback stimulation sites. . . . .	11
1.9	The graphical representation of (a) mechanotactile, (b) vibrotactile, and (c) electrotactile sensory feedback modalities. Courtesy of C. Antfolk . . . . .	12
1.10	WiseSkin system diagram. The hand gloves are embedded with miniaturized sensors. The sensor data is communicated wirelessly to a master node. Then the information is processed and used to drive actuators embedded in the socket. . . . .	17
2.1	Examples of (a) a gelled EMG electrode and (b) a dry EMG electrode. Courtesy of Covidien (Medtronic) and Ottobock. . . . .	20
2.2	A typical EMG collection scheme consisting of surface EMG electrodes. In this case, the collection channel is 16. Reprinted with permission from [135]. . . . .	21
2.3	EMG data segmentation with (a) the adjacent technique and (b) the overlapping or sliding technique. . . . .	21
2.4	Illustration of the majority voting processing. The voting size is 9. The number inside the window represents the class label. . . . .	23

## List of Figures

---

2.5	The deep belief network architecture used in the current study. It consists of two stacked autoencoders and a softmax classifier at the output. . . . .	26
2.6	The EMG electrodes placement used in the EMG acquisition for the three datasets used in this study. (a) The individual finger movement dataset [135] was collected through 16 EMG channels. (b) The CapgMyo dataset [157] was collected through an 128 (8 strips of 16 channels) high density EMG channels. (c) The MEC dataset [158] was collected through 8 channels. The stars represent the reference electrodes. . . . .	29
2.7	The accuracy and real-time metrics of different features and feature combinations. The x-axis represents the number of features. The chosen window size is 150 ms with 50 ms increment size. The used dataset is the individual finger movement dataset. . . . .	32
2.8	The accuracy and real-time metrics when using different window sizes. The increment size is fixed at 10 ms. The x-axis is the window size. The dataset shown is the individual finger movement. Two types of features were used: MAV (plotted in red) and TDAR(6) (plotted in blue). . . . .	33
2.9	The accuracy and real time performance results of EMG classification. The example dataset is the individual finger movement. The window size is fixed at 150 ms. The feature set is TDAR(6). The other feature sets and different window sizes have shown similar trends. The error bars represent the standard derivatives. . . . .	34
2.10	The accuracy and real-time metrics of different algorithms and four feature/feature combinations of individual finger movement dataset. The error bars indicate the standard derivatives. The applied window size is 150 ms with 50 ms increment size. . . . .	36
2.11	The accuracy and real-time metrics of different algorithms and four feature/feature combinations of CapgMyo (hand gesture) dataset. The error bars indicate the standard derivatives. The applied window size is 150 ms with 50 ms increment size. . . . .	37
2.12	The accuracy and real-time metrics of individual finger movement data set after majority voting. . . . .	38
3.1	Penfield map i.e. a human body representation in the brain [172]. On the Penfield map, the area representing the hand in the brain is bordered by the face and arm regions. . . . .	42
3.2	Automatic phantom map detection flow. The detection algorithm includes: sampling, training, and classification. The final output is the predicted phantom map. In this work, the amputees are assumed to always give the right answer. . . . .	43

3.3	Two real phantom map examples. Left: a complete phantom map with five phantom digits: D1 to D5 represent thumb, index, middle, ring, and little phantom finger, respectively. The phantom map shapes were detected by palpation [170]. Right: a complete phantom map with either shared phantom fingers or indistinguishable phantom fingers under testing conditions (touching with a pen). D0 represents tested areas without phantom sensation. D23 and D235 represent shared phantom sensation areas [168]. . . . .	44
3.4	Phantom map generation flow graph. The generation consists of four steps: define a window, select points within the window, connect the points, and assign the phantom finger. . . . .	45
3.5	Phantom sensation coverage control: average $C_{PS}$ of 5 fingered phantom maps generated by varying $a$ and $b$ within $0 < a, b \leq 60$ . . . . .	46
3.6	$C_{PS}$ distribution of 400 generated phantom maps (100 samples of each type). x-axis: $C_{PS}$ , y-axis: number of phantom maps. . . . .	47
3.7	Examples of generated phantom map models. . . . .	48
3.8	Examples of transformed phantom map images from the reported phantom map images. . . . .	49
3.9	Graphical representations of sampling methods. The number of samples is 100. The stars represent sampled points (enlarged for better visualization). . . . .	50
3.10	The architecture of an OVA-SVM in classifying a complete phantom map. Zero(0) to five(5) represent no phantom sensation, thumb, index, middle, ring, and little phantom finger, respectively. $D_{i,\bar{i}}$ represents a binary SVM (a decision function) in classifying class $i$ and the rest of the classes. . . . .	51
3.11	The OVO-SVM architecture in classifying a complete phantom map. Zero to five represent no phantom sensation (0), thumb (1), index (2), middle (3), ring (4), and little phantom finger (5). $D_{i,j}(\vec{x})$ represents a binary SVM (a decision function) in distinguishing class $i$ and class $j$ . . . . .	51
3.12	The DAG-SVM architecture in classifying a complete phantom map. Zero to five represent no phantom sensation (0), thumb (1), index (2), middle (3), ring (4), and little phantom finger (5). $D_{i,j}(\vec{x})$ represents a binary SVM for classifying between class $i$ and class $j$ . $\bar{i}$ on the branch represents the decision function output that the testing point does not belong to any class $i$ . . . . .	52
3.13	A BT-SVM architecture for classifying a complete phantom map. Zero to five represent no phantom sensation (0), thumb (1), index (2), middle (3), ring (4), and little phantom finger (5). $D_{(\vec{i}),(\vec{j})}(\vec{x})$ represents a binary SVM in distinguishing between classes included in $\vec{i}$ and classes included in $\vec{j}$ . $(\vec{i})$ represents the decision function output that the data does not belong to any of the classes included in $\vec{i}$ . . . . .	52
3.14	Two types of stimulation devices: (a) mechanotactile stimulation device and (b) multi-modal stimulation device, principally used for providing sensory feedback for upper limb amputees. An array consisting of $3 \times 5$ multi-modal stimulation devices are also shown (c). . . . .	55

## List of Figures

---

3.15	Graphical representations of coarse array sampling. The blue stars represent sampling points, enlarged for better visualization. (a) Multi-modal stimulation array: $3 \times 5$ sampling size with $15 \times 9$ pooling size. (b) Mechanotactile stimulation array: $4 \times 6$ sampling size with $7 \times 7$ pooling size. . . . .	56
3.16	Examples of generated phantom maps, predicted phantom maps, their confusion matrices, absolute error rates ( $E_A$ ), functional error rates ( $E_F$ ), redundancy error rates ( $E_R$ ), insufficiency error rates ( $E_I$ ), and precision error rates ( $E_P$ ) using (a) BT-SVM with $3 \times 3$ majority pooling and (b) OVA-SVM with $3 \times 3$ majority pooling. . . . .	58
3.17	Examples of (a) the photos of phantom maps drawn on the remaining stumps ((1)[170], (2)[177], (3) [176], (4)[176], (5)[177]), (b) the down-sampled phantom map matrices based on the photos, (c) the predicted phantom maps using OVO-SVM with majority pooling (pooling size = $2 \times 2$ ), and (d) the predicted phantom maps using BT-SVM with majority pooling (pooling size = $2 \times 2$ ). The phantom maps predicted using OVO-SVMs better represent the original shapes of the phantom fingers than the ones using BT-SVMs. Due to the architecture of BT-SVM, the phantom fingers tend to become attached to each other. . . . .	60
3.18	Grand average error rates and phantom sensation coverage ratios over (a) all 400 generated phantom maps and (b) five reported phantom map images and their corresponding transformed images. For $2 \times 2$ majority pooling, $\overline{E_{MP}} = 5.35\%$ for generated phantom maps and $\overline{E_{MP}} = 4.27\%$ for reported phantom map images. The grand average accuracy is influenced both by the sampling methods and SVM algorithms used. For both generated and reported phantom maps, OVO-SVM produces the smallest error rate. Even though the absolute error rate ( $E_A$ ) for reported phantom maps is higher than for the generated ones, the more critical metric (function error rate $E_F$ ) is still within an acceptable range. . . . .	66
3.19	Absolute error rate $E_A$ vs. $C_{PS}$ using different sampling methods for OVO-SVM. The phantom map models used are 100 complete phantom maps with 5 fingers. . . . .	67
3.20	Learning curves for different batch sizes and different initial sizes using MS selection strategies. The x-axis is the size of training data sets. The y-axis is the absolute error rate. The absolute error rate was averaged over 400 phantom maps. The used algorithm is OVA-SVM with random sampling. The stop criterion is when the number of sampling times reaches 100. . . . .	67
3.21	Examples of using coarse stimulation arrays to detect phantom map distributions. The array types used and algorithms are (a) OVO-SVM, $3 \times 5$ multi-modal coarse array (corresponding to $15 \times 9$ majority pooling), and (b) BT-SVM, $4 \times 6$ mechanotactile coarse array (corresponding to $7 \times 7$ majority pooling). . . . .	68
3.22	Examples of shifting error caused by a lateral socket shift. . . . .	68
3.23	Absolute error rate $E_A$ and functional error rate $E_F$ vs. phantom sensation coverage $C_{PS}$ caused by different degrees of shifting. The phantom map models used are 100 complete phantom maps with five fingers (Fig. 3.6(a)). The algorithm used was OVO-SVM with $2 \times 2$ majority pooling. . . . .	68

3.24	Error rates ( $E_A$ : red, $E_F$ : green, $E_R$ : blue, and $E_I$ : Magenta, $E_P$ : black) as functions of different degrees of shifting (no shift, 2 % shift, and 5 % shift). The rectangle spans the first and third quartile of the error rate. The line inside each rectangle shows the median value. The two whiskers above and below each rectangle show the minimum and the maximum. The phantom map models used are 100 complete phantom maps with five fingers (Fig. 3.6(a)). The algorithm used was OVO-SVM with $2 \times 2$ majority pooling. . . . .	69
4.1	Selected illustrations of some psychophysical methods: (a) the constant stimuli method, (b) the staircase method, and (c) signal detection theory. . . . .	75
4.2	The custom-designed stimulation array consisting of 9 ERMs or 9 LRAs embedded in the thin silicone plates. The LRA vibrates vertically. The ERM rotates around its axis. In order to avoid the cross-talks between each actuator, there is a ditch surrounding each actuator (shown in the zoom in). The vibrators are arranged to provide different distances. . . . .	77
4.3	The experimental setup: The participant rested the arm on a cushion placed on the table and followed the instruction shown in the computer screen. During all the experiments, the participant wore a headphone with white noise. The tactile display was fixed by a blood pressure cuff. . . . .	78
4.4	The boxplot of minimal detectable level of LRAs and ERMs. . . . .	80
4.5	The JNDCI plot of (a) LRA and (b) ERM at different starting levels when $w = 0.3$ . St stands for standard stimulus. JNDCI stands for just noticeable difference confidence index, defined in (4.2). . . . .	81
4.6	The designed multimodal tactile display device. This multimodal tactile stimulation device consists of a servo motor, an ERM vibrator, and a custom-made, 3D printed casing. . . . .	87
4.7	The average detection accuracy of mechanotactile (Me) and multimodal (Mu) stimulation devices in localization (Lo), force level detection (F), intensity level detection (I), and combined (C) tests. . . . .	88
5.1	The system illustration of the WiseSkin sensory feedback. . . . .	97
5.2	Wireless sensor node (courtesy of CSEM). (a) wireless sensor node PCB, containing a barometric sensor, a micro-controller, and a wireless transmitter. (b) Schematic view of the process of manufacturing the wireless sensor node. . . .	98
5.3	Power distribution system. a) General view of the power distribution system. Wireless sensor nodes are embedded in a silicone scaffold and sandwiched between two metallized planes that power the sensor nodes and form a waveguide for wireless communication. b) Wireless sensor nodes and relay antenna inserted into a 3D printed silicone scaffold. (c) Skin flexibility demonstration. Scale bar is 20 mm. . . . .	99
5.4	a) Output of a sensor as a function of applied force. 10 loading and unloading cycles are represented. b) Output of five sensors as a function of applied force. Error bars represent standard deviation ( $n=10$ ). . . . .	100

## List of Figures

---

5.5	Communication flow chart of the sensory feedback system. . . . .	101
5.6	The phantom map drawn by the amputee. . . . .	102
5.7	During the localization test, the subject was blindfolded, wearing a noise isolating headset, and fitted with the sensory feedback system. The experimenter pressed the robotic finger and the subject answered which finger he felt being touched. . . . .	103
5.8	Block diagram of the sensory feedback system integrated on a myoelectric prosthesis, consisting of five tactile sensors on the tip of the phalanges, processing and communication modules, . . . . .	104
5.9	(a) Each tactile sensor PCB, covered with a silicone layer, was attached to a 3D printed cap and mounted on the robotic hand fingertip. (b) Normalized sensor output <i>vs.</i> applied vertical force. S1 to S5 represent the sensors mounted on the robotic hand from thumb to little finger, respectively. (c) The sensor response (empty blue dots) and the applied force (empty red dots) plotted against time. (d) The sensor response (empty blue dots) and the applied force (empty red dots) in one testing circle. . . . .	106
5.10	(a) The design concept of the multi-modal sensory feedback device: two servo motors (A) push one cylindrical vibrator (B). (b) The multi-modal device integrated in a 3D printed casing. (c) The multi-modal sensor feedback array arranged to match the phantom map distribution of one test-case amputee. . . . .	107
5.11	The recognition rate of three amputees (A1, A2, and A3) and the averaged recognition rate during three sub-experiments. . . . .	110
5.12	Schematic of the single-site vibrotactile sensory feedback system . . . . .	112
5.13	The diagram of the sensory feedback system control. . . . .	112
5.14	Five equisized cubes: four sponges with different deformability and a wooden block. . . . .	114
5.15	The error scores in the absolute deformability testing with and without sensory feedback. . . . .	115
5.16	The confusion matrix of the comparative deformability test (a) with sensory feedback and (b) without sensory feedback. . . . .	116

# List of Tables

1.1	Comparison between body-powered and myoelectric prostheses . . . . .	3
1.2	Properties of mechanoreceptors [60] . . . . .	8
1.3	Overview of the main sensory feedback approaches . . . . .	9
1.4	Comparison of different vibrotactile actuators . . . . .	14
2.1	Summary of the three EMG datasets used in this study. . . . .	29
3.1	Multi-class SVM classifiers: number of binary SVMs required for the four main decomposition methods. . . . .	51
3.2	Simulation setup using dense ( $100 \times 100$ ) and coarse arrays (multi-modal and mechanotactile) for different sampling methods. . . . .	56
3.3	Absolute error rates of active learning SVMs using different query strategies, diversity criteria, initial and batch sizes. The algorithm used is OVA-SVM with $2 \times 2$ majority-pooling sampling. For ABD, the trade-off parameter $\lambda = 0.5$ . . .	62
3.4	Grand average accuracy results over all 400 generated phantom maps using coarse stimulation arrays (Fig. 3.14). . . . .	63
3.5	Grand average training time $\overline{T}_t$ and classification time $\overline{T}_c$ of all 400 generated phantom maps using a dense array (100 samples) and two coarse (stimulation) arrays ( $3 \times 5$ and $4 \times 6$ actuators, corresponding to simulation pooling sizes of $15 \times 9$ and $7 \times 7$ ). . . . .	64
4.1	Comparison of four non-invasive tactile modalities. . . . .	72
4.2	The characteristics of the LRAs [97] and the ERMs [227] used in this study. . . .	76
4.3	The standard stimuli for LRAs and ERMs . . . . .	79
4.4	The average minimal detectable activation levels of ERM and LRA of all participants over the 4 sessions. . . . .	80
4.5	The average minimal detectable activation levels of ERM and LRA during each session . . . . .	80
4.6	The average correct answer percentage of LRAs and ERMs during the two point discrimination experiments. . . . .	82
4.7	The tactile information transfer of mechanotactile and multimodal in localization, intensity identification, and combined tests. . . . .	89
5.1	Summary of reported sensors used in prosthetic hands . . . . .	92

## List of Tables

---

5.2	Summary of reported sensors used in prosthetic hands . . . . .	94
5.3	Average power consumption of a single ERM vibrator used in the current system	101
5.4	Specifications of the multi-modal actuator . . . . .	107
5.5	Average power consumption of the actuators under three stimulation intensities	108
5.6	Stimulation intensity overview. The current was measured and the amplitude and frequency were calculated from the datasheet. . . . .	110
5.7	Characteristics of the manufactured solenoid actuator . . . . .	113
5.8	Experiment summary of single-site vibrotactile sensory feedback . . . . .	113
5.9	Time needed to move the fragile objects for 10 times. . . . .	116

# 1 Introduction

This thesis describes different aspects in bi-directional control and feedback for upper limb prosthetic users. The problems with current prostheses and challenges for increasing prosthesis acceptance rates are first highlighted, and then the pattern-recognition based prosthetic control methods are depicted. The rest of the thesis focuses on different non-invasive sensory feedback methods.

## 1.1 Upper limb amputees and upper limb prostheses

Hand amputation is a dramatic event that can greatly degrade the life quality of the amputee. The major causes of upper extremity amputation are trauma, dysvascularity, and neoplasia [1]. Depending on the amputation level, upper extremity amputation can be classified into partial hand amputation, wrist disarticulation, transradial (below elbow), transhumeral (above elbow), shoulder disarticulation, and forequarter amputations (Fig. 1.1).

About 80 % of upper limb amputees are reported to use prostheses [3]. A hand/arm prosthesis is a device that aims to replace, at least partially, the functionality of the missing hand and/or arms. The upper limb prostheses can be categorized into passive prostheses and active prostheses. Passive or cosmetic prostheses mainly serve an aesthetic purpose and sometimes help to balance the body to avoid spinal misalignment (Fig. 1.2(a)) [4]. Active prostheses offer active grasping functions.

Within the active prostheses, the body-powered (BP) prostheses can be open and closed through a harness and cable system worn on the shoulder (Fig. 1.2(b)). Depending on their mode of operation, BP prostheses are further divided into a voluntary opening type and a voluntary closing type [5]. Experiments have indicated that voluntary closing prostheses have a faster operation speed compared to that of voluntary opening prostheses, when tested with standard clinical outcome measures. However, the most highly desired BP prosthesis control combines both voluntary closing and voluntary opening, so that the user can switch between the two operation modes for different tasks [6]. BP prostheses are simple to use, robust, and

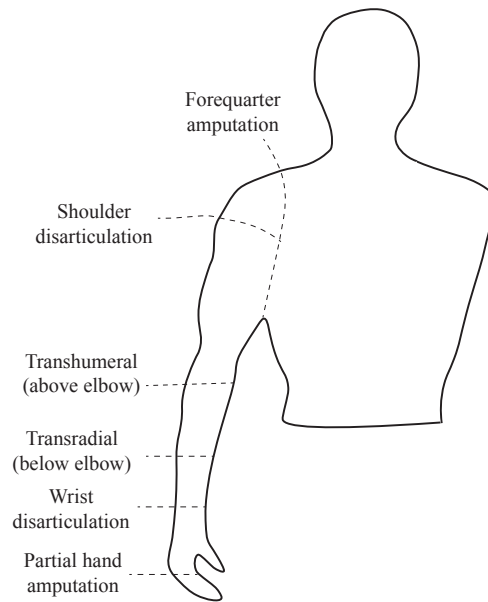


Figure 1.1 – Illustration of amputation levels [2]

inexpensive. However, their drawbacks include high energy expenditure from the user and a limited control interface: most BP prostheses only offer one degree-of-freedom (DoF) at a time [7].

The other type of active prostheses are externally powered ones. In previous research, hydraulic and pneumatic prostheses have both been proposed. In the current market, however, electrically powered prostheses are the main form of externally-powered active prostheses. Electrically powered prostheses can be controlled through brain-machine interfaces [8, 9, 10] and peripheral interfaces [11, 12, 13, 14, 15, 16], or electromyographic (EMG) signals. Most commercial prostheses are controlled through EMG signals. These types of prostheses are referred as myoelectric prostheses (Fig. 1.2(c)). EMG signals represent the muscle generated electrical currents during contraction, and describe neuromuscular activities [17]. Commercial myoelectric prostheses generally apply two EMG electrodes over the flexor and extensor muscles of the forearm for transradial amputees, or over the biceps and triceps for transhumeral amputees, or over the pectoral muscle and deltoid for shoulder disarticulation amputees. In the current research, the number of EMG electrodes used ranges from two to 32 [18, 19]. The myoelectric prostheses provide the most dexterous and intuitive control [2]. A survey with prosthetic users have shown that amputees prefer to use body-powered prosthesis while conducting tasks of manual labor. The myoelectric prostheses are preferred by the users while doing office work [20]. The comparison of the two types of active prostheses are listed in Table 1.1.

Despite some drawbacks of myoelectric prostheses, clinical surveys have shown that myoelectric prostheses have the highest user acceptance rate: 82 % for transradial amputees, 86 % for transhumeral amputees, and 100 % for shoulder disarticulation amputees [22].

## 1.1. Upper limb amputees and upper limb prostheses

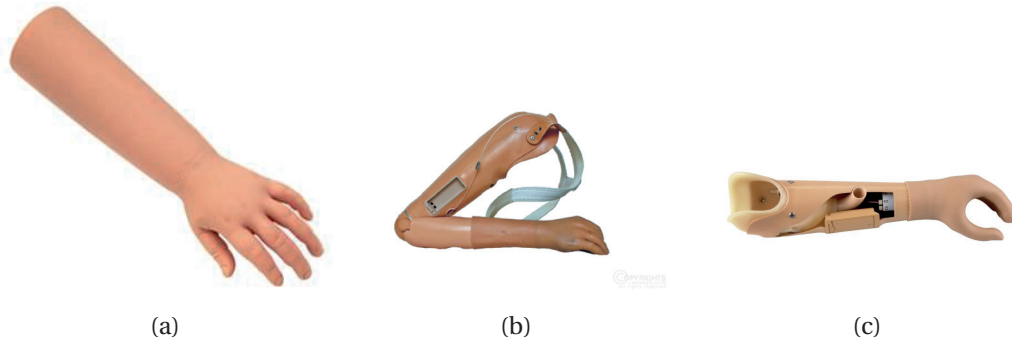


Figure 1.2 – Examples of (a) a cosmetic prosthesis, (b) a body-powered prosthesis [7], and (c) a myoelectric prosthesis [21]

Table 1.1 – Comparison between body-powered and myoelectric prostheses

Aspects	Body-powered	Myoelectric
Function	Less influenced by the temperature Some proprioception Intuitive control	Strong pinch force Secure grasp Fine pinch possibility Minimal body-movement Minimal physical effort Larger range of motions
Appearance	Less natural with the harness	More natural looking No large control motions
Comfort	Less heavy Soft flexible inner liner inside the socket	No harness attached to the body
Others	Low cost Do not need to charge batteries More durable Robustness Less training required Less environment sensitive	Easy to put on and off

Current advanced myoelectric prostheses can have several movable joints and a large range of movement patterns (for example: iLimb Hand from Touch Bionics, UK [23], Michelangelo hand from Otto Bock Health Care Products, Germany [21], bebionic hand from RSL Steeper, UK (recently acquired by Otto Bock) [24], Vincent Hand from Vincent Systems, Germany [25], ToMPAW [26] and Luke Arm from Mobius Bionics LLC, US [27] ).

The actuators used in commercial prostheses are direct-current (DC) motors. Both brushed and brushless motors are used. Brushless motors have a higher torque/weight ratio but also need a more complicated control system. They are more commonly used in research hands. Most of the multi-grasp commercial hands provide rotating thumbs because thumb movements were reported to contribute, arguably, to 40 % of all hand movements [28]. The weights of commercial prostheses range from 350 g to 615 g [29], which is comparable to the

## Chapter 1. Introduction

---

weight of a human hand. However, because the prostheses are attached to soft tissues, it felt heavier. One of the design changes required by the amputees is to reduce the prosthetic weight [2].

There are also a wide range of research hands developed in universities or research institutes: SmartHand [30], Vanderbilt multigrasp hand [31], Pisa/IIT SoftHand [32], TBM Hand [33], Remedi Hand [34], Manus Hand [35], to name a few. Because many of the research hands focus on a certain feature and not on the entire system, it is difficult to compare directly the research hands with the commercial ones.

Many of the research hands and some of the commercial prostheses have used the design concept of underactuation to reduce the weight and increase the degree-of-freedom [29]. The principle of underactuation is that the number of actuators is lower than the number of usable degrees-of-freedom [36].

One of the emerging trends for prosthetic design and fabrication is the application of additive manufacturing for customized prosthesis design. Additive manufacturing is also referred to as 3D-printing. In one-way of 3D-printing, the objects are constructed by depositing thermoplastics in layers [37]. The 3D-printed prostheses are customizable. It is especially attractive for amputated children because of their constant growth and the need to replace prostheses or parts of the prosthesis regularly. There are some 3D-printed myoelectric prosthesis platforms: Open Bionics (electrically powered) [38], previously known as the Open Hand project, and Tact hand (can be electrically powered) [39] for transradial amputees, as well as Limbitless solutions [40] and Cyborg Beast [41], focusing on 3D-printed prostheses for children. The website e-NABLE also provides several body-powered hand designs [42].

### Control of Myoelectric Prostheses

Both intramuscular EMG (iEMG) and surface EMG (sEMG) signals were reported to be used to control prostheses [43, 44, 45]. The iEMG signals are collected through percutaneous wire or needle electrodes or wireless implanted recording electrodes. Compared to sEMG, iEMG has less crosstalks and higher selectivity [46]. The sEMG records the muscle activities on the skin surface. Although it suffers from crosstalk and it is sensitive to electrode displacement and contact condition changes, it is still preferred by all commercial prosthetic providers because of its non-invasive nature. The sEMG signal also offers a global overview of the muscle contraction activities. Thus, the rest of the section will only discuss the control strategies using sEMG, even though some of the control methods could also apply to iEMG signals. The myoelectric prosthetic control methods can be divided into non-pattern recognition based methods and pattern recognition based methods (Fig. 1.3).

**Non-pattern recognition based methods** For hook-like myoelectric prostheses (normally with 1 DoF), the on-off control and the proportional control are generally used to open or close

Non-pattern recognition based methods	Pattern recognition based methods
On-off control	Neural network
Onset analysis	Linear discriminate analysis
Proportional control	Fuzzy logic
Finite state machine control	Gaussian mixture models
	Support vector machines

Figure 1.3 – Classifications of myoelectric control methods

the hand. For the on-off control, muscle flexion closes the hand and muscle extension opens the hand, or vice versa. In addition to on-off control, the proportional control incorporates speed or force control: the opening and closing of the prosthetic hand is proportional to the magnitude of the EMG signal. The onset control is also reported to control the 1-DoF prosthesis by detecting the start and ending of the EMG activation signals [47]. For multi-grasp prostheses, finite-state-machine (FSM) control is widely used in commercial prostheses (e.g. i-Limb [23] and bebionic [24]) as well as in some research hands (e.g. Southampton REMEDI hand [48] and Vanderbilt hand [31]). For FSM control, each state represents a targeted hand gesture and the muscle flexion and closing changes within each state. Muscle contraction switches between states in a predefined sequential order (Fig. 1.4).

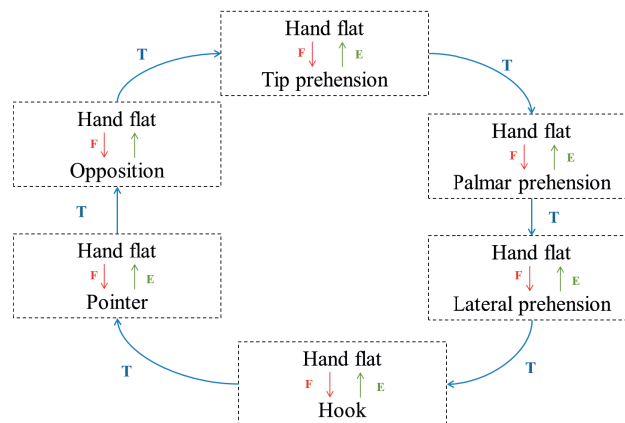


Figure 1.4 – State diagram of i-Limb prostheses control [49]. The architecture consists of six states corresponding to the six target postures, excluding hand gestures (resting phase). E represents extension, F represents flexion, and T represents a trigger command (combined flexion and extension EMG signals that is greater than a tuned threshold). A trigger (T) iteratively changes states in a specified order.

The non-pattern recognition based methods (sometimes also referred as direct control methods) are: simple, primitive and robust. However, the control interfaces of those methods are limited and often unnatural.

**Pattern recognition based methods** Pattern recognition based control strategy relies on machine learning algorithms to detect and classify EMG signals. For pattern-recognition-based control, the procedure consists of three steps: data acquisition, data pre-processing and classification (Fig. 1.5). The raw EMG data is collected by the EMG electrodes channels (Fig. 1.5:A). Then the data is filtered, amplified, and digitized (Fig. 1.5:B). During the classification phase (Fig. 1.5:C), the digitized data is first segmented into time windows. Within each window, features are extracted. Both time-domain (TD) and frequency-domain (FD) features are proposed in the literature. The commonly used features include mean absolute values (MAV), zero-crossings (ZC), slope sign changes (SSC), waveform length (WL), median frequency (MF), power spectrum density (PSD), and signal-to-noise ratio (SNR). The extracted features or feature combinations are used for classification by a classifier. Commonly used classifiers include artificial neural networks [50, 51, 52], fuzzy logic algorithms [53, 54], support vector machines [55], and so on. Pattern recognition based methods can be intuitive but the drawbacks of this method include sensitivity to noise (socket shifting, limb movement, etc.) and the delay caused by data segmentation. More details on pattern recognition based prosthetic control can be found in Chapter 2.

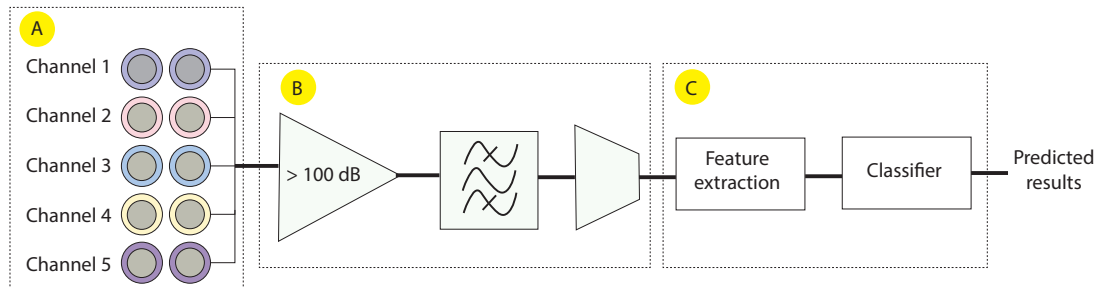


Figure 1.5 – Procedure of pattern recognition based prosthetic control.

## 1.2 Somatosensory system

The somatosensory system provides information of touch, pain, temperature, position, movement, and vibration [56]. This section mainly focuses on two modalities in the somatosensory system: the sense of touch and proprioception. Both types of sensations are important for prosthetic control and prosthetic embodiment. The sense of touch includes perceptions of contact, pressure, vibration, and fluttering. The proprioceptive sensory system provides information regarding limb orientation, position, and movement [57].

### 1.2.1 The sense of touch

Mechanoreceptors are responsive to mechanical pressure or distortions applied to the skin. There are four types of mechanoreceptors in the glabrous (hairless) skin (Fig. 1.6): Meissner's corpuscles, Pacinian corpuscles, Merkel disks, and Ruffini endings [58]. There is one more receptor in hairy skin. Meissner's corpuscles are the shallowest mechanoreceptors and they are sensitive to low-frequency vibration and texture changes. Pacinian corpuscles are the largest mechanoreceptors. They are responsible for high frequency vibration perception. Their response frequency ranges from 40 to 800 Hz, but are most sensitive between around 200 and 300 Hz. The Merkel disks (also known as Merkel nerve endings) detect sustained pressure. The Ruffini endings detect tension deep in the skin and fascia (Table 1.2) [59]. Receptors in hair follicles sense when a hair changes position.

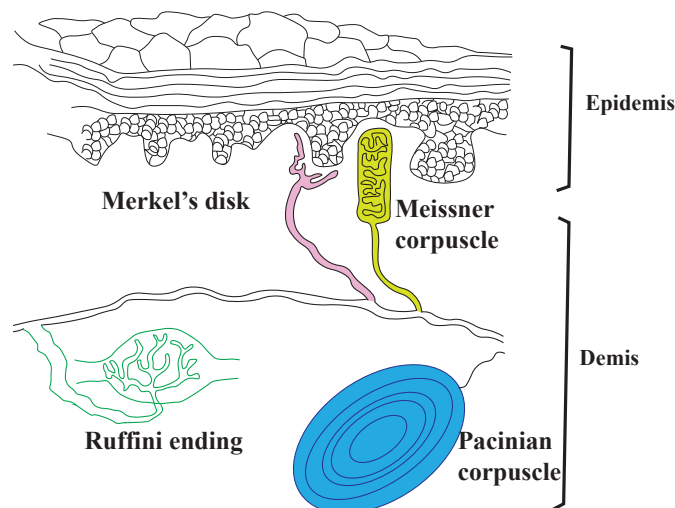


Figure 1.6 – The mechanoreceptors in the human skin [60].

### 1.2.2 Proprioceptive sensory system

Proprioception sensation conveys the information of the movement and position of limbs. Proprioception is important in the sensory system because it enables the humans' awareness to move purposely [61]. Lack of proprioceptive information can result in uncoordinated finger movements, coarse and exaggerated grasping behaviors, as well as an incapacity to plan limb movement dynamics [62]. The proprioceptive signals are transmitted by the large muscle afferent to the motor cortex via the dorsal columns [63] and to the cerebellum via spinocerebella tracts [64]. Proprioceptors are found in muscles, joints, and skin. Different proprioceptors are reported to sense muscle strength, muscle stretch velocity, and tension in the tendon. Proprioception is a compound sense, relying on simultaneous information related to changes in the angle, direction, and velocity of joint movements.

Table 1.2 – Properties of mechanoreceptors [60]

Receptor name	Receptor type	Adaptation rate	Receptive field	Function
Meissner's corpuscles	FA I (RA)	Rapid	Small	Light touch, dynamic pressure (5 to 10 Hz)
Pacinian corpuscles	FA-II (PC)	Rapid	Large	Vibration (250 to 350 Hz), fine surface texture
Merkel's disks	SA-I	Slow	Small	light pressure (<5 Hz, shape and edge detection, rough texture
Ruffinin ending	SA-II	Slow	Large	Slippage detection, skin conformation or stretch
Hair follicle	RA	Rapid	?	Stroking, fluttering

RA represents rapid adapting

SA represents slow adapting

### 1.3 Sensory feedback: state-of-the-art

Although design of prostheses has made significant progress in the past decades, restoring natural control and feeling remains to be achieved. Only one commercial prosthetic hand (Vincent Hand evolution 2 [25]) has been equipped with a sensory feedback system: one vibrator to represent the grasping force [25]. Surveys with amputees have shown that most active prosthetic users desire to feel the grasping force and to sense temperature. Pylatiuk's survey even listed sensory feedback as the most desired design priority for upper limb prostheses [65]. Providing sensory feedback could enhance object manipulation ability [66], increase the embodiment feeling [67, 68, 69], reduce phantom limb pain [70, 71], and decrease the cognitive load while using the prostheses[72, 73].

The methods for providing sensory feedback can be roughly organized into two main categories: invasive and non-invasive methods. The invasive approach stimulates either the central nervous system using cortical electrodes [74, 75, 69], or the peripheral nervous system using cuff electrodes [11, 76], intrafascicular electrodes [12], microelectrode array [77], or sieve electrodes [78]. Non-invasive feedback systems apply stimuli on the surface of the skin. The stimuli can be electrical currents (electrotactile), vibrations (vibrotactile), mechanical pushing force (mechanotactile), or multi-modal stimulation on the skin to elicit sensations. The overview of the main sensory feedback approaches are presented in Table 1.3.

#### 1.3.1 Invasive sensory feedback

Invasive sensory feedback is often coupled together with prosthetic control using neural interfaces. The implanted electrodes serve both as signal collecting devices and stimulation devices. Based on the implantation sites, invasive sensory feedback can be categorized into

### 1.3. Sensory feedback: state-of-the-art

Table 1.3 – Overview of the main sensory feedback approaches

Methods		Advantages	Limitations
<b>Invasive methods</b>			
Periphery stimulation	Extraneural	Simple implementation Well understood	Higher stimulation current Hard to focus on the certain nerves Potentially evoke paresthesias
	Intraneural	Introduce more natural feeling	Higher risk for nerve damage
Central nervous system stimulation		High surgical risk	Potential richer information
<b>Targeted muscle reinnervation</b>			
Targeted sensory reinnervation		No implants, Easier surgical procedure, Long-term stability, Natural sensation	Limited sensation capacity Non-somatotopically organized limb representation
<b>Non-invasive methods</b>			
Mechanotactile		High power consumption Large size Slow response	Modality-matching
Vibrotactile		Small Light weighted Easy to control	Modality-mismatched Wave propagation
Electrotactile		Thinness Mechanical robustness	Interference with EMG signal Stability issue
Multi-modal		Richer haptic information	Can cause confusion

central nervous system stimulation and peripheral nerve stimulation.

The development of central nervous stimulation is still at an early stage. Penfield has first demonstrated that electrical stimulation applied to the brain could elicit somatosensory perception [79]. Flesher *et al.* implanted two microelectrode arrays in the primary somatosensory cortex of one participant with spinal cord injuries [80]. The results suggested that intracortical microstimulation can potentially provide natural somatosensory feedback. The study done by Collins *et al.* demonstrated that electrical brain stimulation could also induce body ownership feeling towards an artificial limb [69]. Because of its high surgical risks and invasiveness, it is sometimes not justified to apply brain implants for prosthetic users. Central nervous stimulation is not widely applied to amputees, but rather to high-level tetraplegics.

Peripheral stimulation approaches can be further classified into intraneural stimulation and extraneural stimulation. The reported peripheral neural interfaces include cuff electrodes, flat interface nerve electrodes, longitudinal intrafascicular electrodes, transverse intrafascicular electrodes, microelectrode stimulation arrays, and regenerative (or sieve) electrodes. The selectivity and invasiveness of peripheral nerve stimulation are normally in direct relationship: the higher the selectivity, the higher the invasiveness - and usually the greater the surgical difficulty (Fig 1.7).

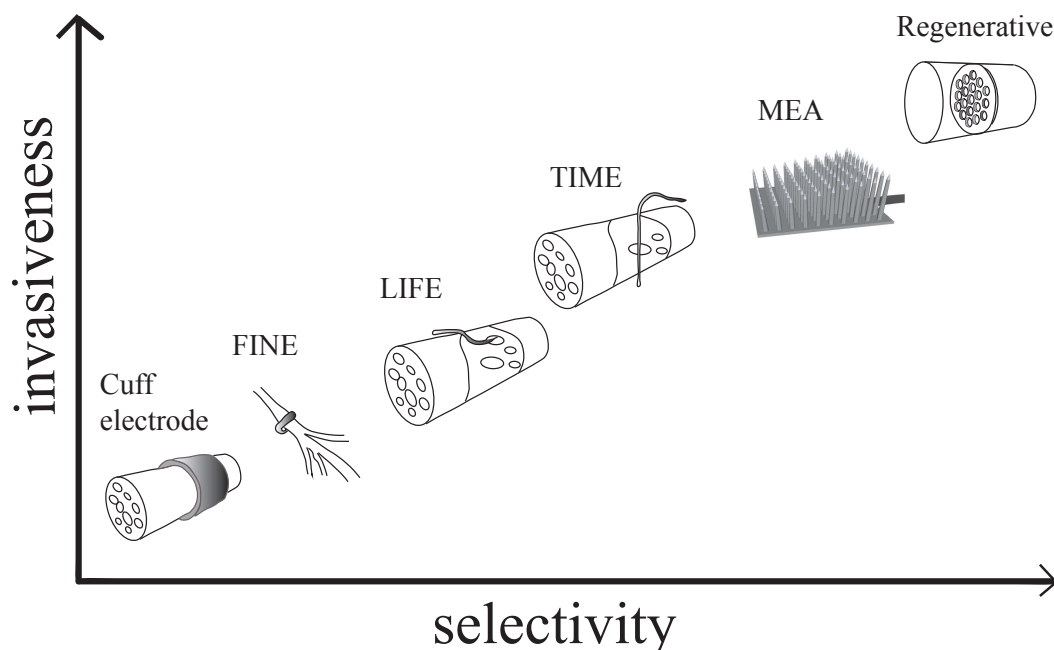


Figure 1.7 – The tradeoff of invasiveness and selectivity of some commonly used implantable electrodes for bidirectional interfacing with the prostheses. FINE is short for flat interface nerve electrode, LIFE is short for longitudinal intrafascicular electrode, TIME is short for transverse intrafascicular multichannel electrode, and MEA is short for microelectrode array [81].

For extraneural stimulation, the implants are in the subcutaneous field and target not a particular nerve, but a bundle of nerves. The implanted cuff electrodes fit around the outside of the nerve bundles. They have low invasiveness, compared to intraneural stimulation, and their biocompatibility/ stability have been proven by several mid- or long-term studies [82, 76]. Another type of extraneural electrodes are flat interface nerve electrodes (FINE) [83]. As with the cuff electrodes, the FINE was implanted around the nerves, but it flattens the nerve to increase contact surface, thus increasing selectivity. The biocompatibility and stability of FINE implanted in humans are yet to be investigated.

For intraneural stimulation, the implanted stimulation leads penetrate the nerves either longitudinally or transversely. Raspopovic *et al.* stimulated the fascicles of the median and ulnar nerve of a transradial amputee by implanting transversal multichannel intrafascicular electrodes. The sensory feedback enabled the amputee to adjust grasping forces and discriminate the stiffness and shapes of three different objects [12].

### 1.3.2 Targeted muscle reinnervation

Targeted muscle reinnervation (TMR) surgery transfers the residual arm nerves to a spare target muscle [84]. The target muscles are normally in the residual limb or the thorax. After surgery, sensory feedback devices are applied to the surface of the skin over the target muscle. The sensory feedback part is still done in a non-invasive manner. Sensation capacity is therefore limited, compared to that of invasive approaches. Kim *et al.* designed a tactor incorporating tapping, static and dynamic pressure, vibration, and shear force for providing sensory feedback for a TMR amputee [85]. The results indicate significant improvements in grip force control with sensory feedback. As mentioned before, sensory feedback can also introduce embodiment feeling. Marasco *et al.* investigated tactile feedback and introduced embodiment on targeted reinnervation amputees. They concluded that by providing physiologically relevant haptic feedback, the amputee could incorporate the prosthesis as part of the body, instead of regarding it just as a tool [67]. TMR is beneficial for both transhumeral amputees and disarticulation amputees by increasing the number of myoelectric input sites for prosthesis control [86, 87], as well as providing a larger area for sensory feedback.

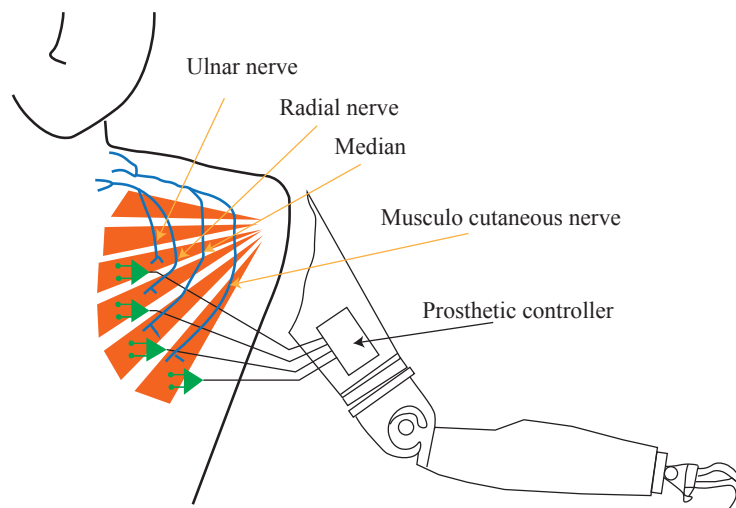


Figure 1.8 – The schematic of targeted muscle reinnervation surgery. The reinnervated nerves residing on the chest provide both the control sites and the sensory feedback stimulation sites.

### 1.3.3 Non-invasive sensory feedback

Despite the successful examples of invasive sensory feedback, high surgical risks still impose concerns for many amputees. In various cases, non-invasive sensory feedback is a more practical way of providing sensory feedback for amputees. As mentioned before, main non-invasive approaches include three single modalities: mechanotactile, vibrotactile, and electrotactile, as well as combined multi-modalities. A graphical representation of the three single modalities is shown in Fig. 1.9. Other less frequently reported sensory feedback methods include

auditory feedback [88, 89, 90, 91] and skin stretch. Auditory feedback explores the possibility to modulate the frequency, volume and rhythm of sound to represent grasping force or arm-reaching trajectory. It has shown good performance when the presented information is limited. For skin stretch feedback, devices need at least two reliable points of contact on the skin. Maintaining the robust contact without slipping is the main challenge. The major challenges for non-invasive sensory feedback device design include: small size to fit in the socket, light weight, low power consumption, natural sensation, and ease of integration.

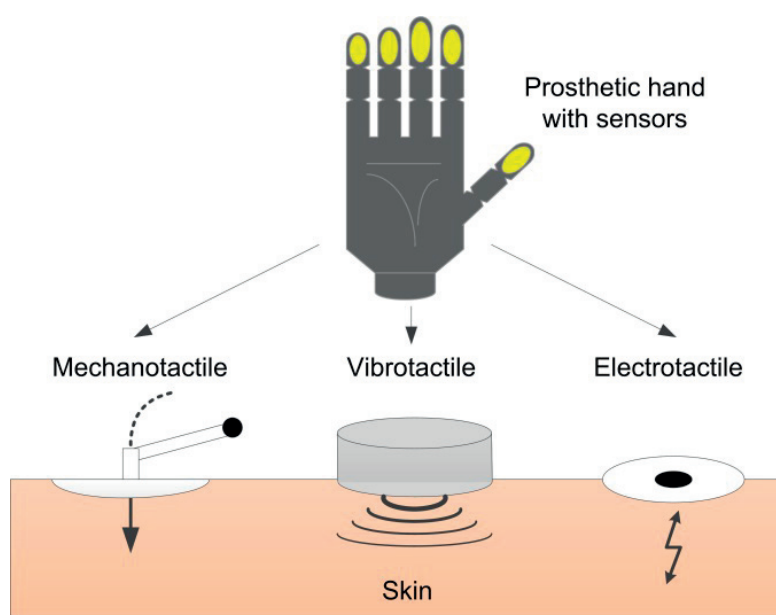


Figure 1.9 – The graphical representation of (a) mechanotactile, (b) vibrotactile, and (c) electrotactile sensory feedback modalities. Courtesy of C. Antfolk

### Mechanotactile

Mechanotactile stimulation applies normal force on the skin, and is a modality-matched feedback method for providing force feedback. The devices used for providing mechanotactile feedback include, but are not limited to: servo motors, voice coil, hydraulic systems, and pneumatic systems [92, 93, 94, 72].

Meek *et al.* implemented a single motor-driven pusher to provide proportional force feedback [95]. The testing results with 10 subjects have shown improved manipulation and grip control with the sensory feedback system.

Patterson *et al.* developed a hydraulic pressure cuff to provide modality-matched sensory feedback and compared the pressure-to-pressure system with vibrotactile and vision feedback in the force matching task. Grasping pressure replication errors and error variability shown to be reduced with the presence of a sensory feedback system.

Antfolk *et al.* has implemented a passive air-mediated pressure sensory feedback system. The system consists of three silicone pairs. Each pair consists of one silicone bulb, as a force sensor, and one silicone pad, placed on the remaining stump of amputees or forearm of healthy subjects, for providing sensory feedback. When pressure is applied on the silicone bulb, the silicone pad will bulge and create pressure sensory feedback. This passive pneumatic system is flexible and light-weighted. The system has proved efficient in localization and force level identification tests [93].

#### **Vibrotactile**

Vibrotactile sensory feedback is widely used because of its compact size, ease of use, relatively fast response speed, and low power consumption [94]. The vibrotactile modulating parameters include frequency, amplitude, location, beat interference, and timing. Commonly used vibrotactile devices include linear electromagnetic actuators (e.g. solenoid, voice coil, linear resonant actuator), rotary electromagnetic actuators (e.g. eccentric rotating mass), and non-electromagnetic actuators.

The linear electromagnetic actuators (LEA) are used to create a fast tapping sensation. Commonly used types include solenoid, voice coil, and linear resonant actuators. The working principle of LEAs is electromagnetism. The actuator can be simplified as a conductive wire coil and a magnet. When a current flows through the coil, a magnetic field is created and thus the magnet is moved from or to the coil. By applying an oscillating current to the coil, a bobbing movement is created. The working principle of the LEAs is the same as in audio speakers. A solenoid is a piece of ferromagnetic material enclosed in a coil while a voice coil is a piece of permanent magnet enclosed in a coil. Some commercial coin type voice coils are designed for haptic rendering: C2 tactor (Engineering Acoustics, Inc [96]) and the pancake linear resonant actuators (LRAs) from Precision Microdrives [97].

Most rotary electromagnetic actuators consist of an off-center mass fixed to the output shaft. These devices are called eccentric rotating masses (ERMs). The frequency and amplitude are coupled together, proportional to the applied direct current (DC) voltages. There is a wide range of commercial ERMs to choose from, both shafted (cylindrical) and shaftless (coin or pancake) types.

The nonelectromagnetic actuators are based on object shape deformation. Actuators based on piezoelectric effect and shape memory effect are used for haptic rendering. Piezoelectric effect is the ability of certain materials to vibrate when a voltage is applied, or to generate current when mechanical stress or vibration is applied. A disk or a beam consisting of several piezoelectric transducers are used for vibrotactile display [98]. Shape memory alloys are a type of material that changes their shape when heated and return to their original form when the heat is removed. The heat can be induced through Joule heating. Shape memory alloys have been proposed for use as an artificial muscle [99] and sensory feedback device [100]. The main drawback of the two above-mentioned non-electromagnetic actuators is that their

## Chapter 1. Introduction

small deformation is not perceivable on hairy human skin. Many of the non-electromagnetic actuators require high voltage (in the range of 1000 V) or produce only small amplitude (can only be perceived on the finger tip, but not on the arm or any other part of the body). Thus, the applications of non-electromagnetic actuators on wearable sensory feedback devices are limited.

A qualitative comparison of the above mentioned actuators is shown in Table 1.4.

Table 1.4 – Comparison of different vibrotactile actuators

Actuator	Advantages	Disadvantages
Linear electromagnetic actuators	High expressiveness Low power	Heating Complex driving circuit
Eccentric rotating masses	Simplicity Reliability Low power	Coupled frequency Starting delay
Piezoelectric	Reverse effect Compact size Fast response time (< 5 ms) High acceleration	Small deformation
Shape memory alloy	Small High power-to-weight ratio	Temperature sensitive Slow response time (>100 ms) Large hysteresis High energy consumption

Vibrotactile sensory feedback systems have been used for providing information regarding hand aperture [66], grasping force [101], contact location [102], and so on. Besides using single vibrators, Cipriani *et al.* stacked pancake type vibrators to provide stimuli with modulate amplitude, frequency, and beat interface. The devices were tested on healthy subjects and the testing results indicated high discrimination accuracy of force levels, locations, and stimulation patterns [103]. Despite being a modality-mismatched feedback method, vibrotactile sensory feedback has also been reported to introduce body ownership feeling to prosthetic users [104, 105].

### Electrotactile

The electrotactile method is also a form of modality-mismatched stimulation. It activates the sensory nerves under the skin by applying a surface electrical current, delivered through the surface electrodes made of conductive plates. The evoked sensations range from pressure, vibration, tickling, to slight pain. Compared to the other two non-invasive sensory feedback methods, electrotactile stimulation devices have the advantages of thinness and contact robustness. But the electrotactile method has several issues that need to be solved: maintaining the strength of the sensation felt, providing natural sensation, and the pain caused by the stimulation.

Electrotactile stimulation can be modulated either by the current pulse amplitude or by the current pulse frequency [106]. AM stimulation is more intuitive while FM stimulation takes time to learn. For a trained subject, both modulation methods can provide five or six discrete levels (recognition rate  $\geq 75\%$ ). Other modulation parameters include stimulation sites, the number of pulses, the number of stimulation channels and interleaved time between channels.

Shannon *et al.* has applied electrical stimuli above the median nerve on amputees fitted with myoelectric prosthesis [107]. The pulse frequency is proportional to the sensed pinch force. The amputees reported an increase in confidence while using their prosthesis. Scott *et al.* has investigated the compatibility of EMG with electrotactile sensory feedback [108]. Anani *et al.* has compared amplitude modulated (AM) electrotactile stimulation with frequency modulated (FM) electrotactile stimulation on transradial amputees [106]. They concluded that AM afferent electrical nerve stimulation can be used to convey sensory feedback provided training and stable electrodes are available. Choi *et al.* used single electrode and different modulation to create both feelings of vibration and tapping [109]. There are still several issues related to electrotactile stimulation that need to be solved: providing natural tactile sensation, minimizing the evoked pain, and stabilizing stimulation strength [110].

#### Multi-modal sensory feedback

Besides the aforementioned three modalities, there are also attempts to combine different modalities for sensory feedback. Several researchers have attempted to compare the effectiveness when combining visual feedback with other modalities, and the results indicate better performance when visual feedback is present [111, 101]. Other researchers have also combined several aforementioned feedback methods to increase psychophysics performances [112, 113] or to increase feedback modalities [114].

#### 1.3.4 Thermal feedback

Thermal feedback is less investigated because it is not crucial to most activities of daily living (ADLs). But it is important for safety and material identification, as well as personal comfort and emotions. Moreover, the temperature information cannot be attained through vision. Most thermal sensory feedback systems are based on thermoelectric devices, also known as Peltier elements. Ho and Jones' paper has reported a thermal display based on Peltier elements and a semi-finite body model [115]. The display was tested on able-bodied subjects' fingertips and showed that they were able to identify different objects with limited visual cues. Ueda *et al.* has reported a Peltier based temperature feedback device. This device was incorporated into a myoelectric prosthesis and tested on ten healthy subjects with an average 88 % success rate in an identification test at five temperature levels [116].

Some research has also incorporated thermal feedback with other modalities [117, 118]. Kim

*et al.* has incorporated Peltier elements in a tactor, providing thermal feedback besides normal force, shear force, and vibration feedback [118]. Jimenez *et al.* has incorporated a Peltier element in a tactile feedback system that can be worn on the arm. One upper limb prosthetic user has tested the system and could distinguish between three different temperature levels [114]. Nakatani *et al.* has improved the design by providing four units of Peltier devices for sensory feedback applications [117].

### 1.3.5 Proprioceptive sensory feedback

Proprioception plays a crucial role in prosthetic control as well as embodiment. Without proprioceptive information, prosthetic users can rely solely on visual feedback, which is tiring and sometimes impractical. By incorporating proprioceptive information, the prosthetic control accuracy can be improved in non-sighted, even sometimes in sighted conditions [61]. Different types of proprioceptive information have been reported to feed back to the prosthetic users, including elbow angle, hand aperture, relative position of the arm, and so on. One of the first attempts to provide proprioceptive feedback is to couple the motion of a prosthetic joint to the motion of an intact joint [119, 120]. Sensory substitution methods using vibrotactile [121, 122, 123] and skin stretch have also been explored. Witteveen *et al.* has applied an array of pancake type vibrators to the lower arm, to indicate the hand aperture. The location of each of the eight vibrators indicate a discrete aperture value [122]. Bark *et al.* has implemented a bench-top skin stretch device with two contact points. The contact points rotate within  $\pm 45^\circ$  to apply skin stretch [123].

## 1.4 WiseSkin

The WiseSkin project aims at providing natural and intuitive sensory feedback to upper arm amputees. The WiseSkin system includes a) wireless sensory nodes embedded in stretchable artificial skin, b) a reliable short-range communication protocol, and c) a vibrotactile stimulation array and driving system (Fig. 1.10). The artificial skin is attached to a robotic hand. It works as a capsule for the wireless sensory nodes, waveguide, and powering system. The communication protocol is an event-driven protocol. The vibrotactile stimulation array is arranged according to the phantom map shape distribution. More details of the project will be introduced in Chapter 5.

## 1.5 Thesis organization

To improve the usability of upper extremity prostheses, both feed-forward control and feedback designs have to be considered. In this thesis, firstly, novel pattern recognition based myoelectric control is proposed and the testing results on three EMG datasets are presented in Chapter 2.

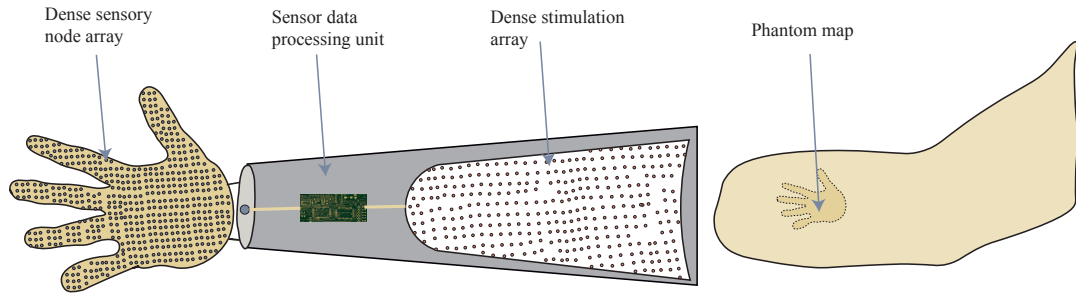


Figure 1.10 – WiseSkin system diagram. The hand gloves are embedded with miniaturized sensors. The sensor data is communicated wirelessly to a master node. Then the information is processed and used to drive actuators embedded in the socket.

The rest of the thesis focuses on providing non-invasive sensory feedback. The design process of a sensory feedback system consists of the following steps: defining the area to place the stimulation devices, designing stimulation devices and testing the suitable stimulation parameters, and incorporating the stimulation devices into the whole sensory feedback systems. The rest of the thesis is organized according to the sensory feedback system design flow. In Chapter 3, the automatic hand phantom map detection algorithms are proposed and tested on both reported phantom maps and generated phantom maps. In Chapter 4, the design and testing of non-invasive sensory feedback arrays are described, as well as the experimental results tested on healthy subjects and amputees. In Chapter 5, we focus on sensory feedback system integration and experimental results.

In the final chapter, the PhD work is summarized and the outlook of the work is depicted.



## 2 Myographic Signal Pattern Recognition for Prosthetic Control

The previous chapter included a short introduction of the issues related to upper limb amputees, state-of-the-art prostheses, and sensory feedback for upper limb prostheses. The control and the sensory feedback, together with the prosthetic user, form the closed-loop control of the prosthetic hand.

This chapter focuses on the pattern recognition-based control of the upper limb prostheses, i.e., the forward path. First, a short introduction of myoelectric signals is given and pattern recognition-based myoelectric prosthetic control methods are reviewed in Section 2.1. Then, in Section 2.2, three algorithms used in our study for EMG classification are introduced. The techniques to extend binary classifiers into multi-class ones are described in Section 2.3. To test the effectiveness of proposed algorithms, three EMG datasets representing different types of upper limb movements were used for classification (Section 2.4) and the results are presented and discussed in Section 2.5. Finally, this study is summarized in Section 2.6.

### 2.1 Introduction

The EMG signal is a measure of the muscle generated electrical currents during contraction [17]. It has a wide range of applications in the field of biomedical engineering (e.g., motor disability rehabilitation [124, 125], human machine interfaces [126, 127], neurology [128], and ergonomics [129]).

Electromyography (EMG) signals collected from the amputees' residual muscles have long been proposed to be used for prosthesis control [130, 131, 132]. One of the critical questions to increase the functionality of myoelectric prosthesis is to advance EMG signal processing and to incorporate more control patterns. Prosthetic control should be mentally undemanding, user friendly, simultaneous, and able to provide independently multi-functional movements[133].

Most of the current commercial prostheses are equipped with only two EMG sensors, and the control methods are normally non-pattern recognition-based (e.g. on-off control or finite-state-machine control). Non-pattern recognition-based control methods have already been

reviewed in Chapter 1.

Pattern-recognition based control strategies have the potential to make control easier and more natural for prosthesis users. A typical pattern recognition EMG control system consists of signal detection and pre-processing, feature extraction, classification, and sometimes, post-processing. Surface EMG signals are collected by electrodes placed on the skin. The collected signals are then amplified, filtered, and digitized. After pre-processing, EMG signals are segmented into time-windows. Within each window, the features will be extracted and fed to the classifier. After the classifier produces a decision, sometimes, post-processing is applied to increase the classification accuracy.

### EMG data acquisition and pre-processing

Surface EMG signals are collected through one or more differential electrodes on the surface of the skin. Surface EMG electrodes can be gelled electrodes (Fig. 2.1(a)) or dry electrodes (Fig. 2.1(b)). Gelled electrodes contain an interface between the electrode and the skin, made of a gelled electrolytic substance. They are commonly used in research EMG collection. A typical research EMG collection is shown in Fig. 2.2. Dry electrodes can directly detect EMG signal without a specific interface. In most cases, the signal tuning circuits are already integrated together with the electrodes [134]. Normally, the electrode placement matches a certain muscle. The signal is then amplified to differentiate small signals of interest. Generally, a band-pass filter is applied to remove motion artifacts (at high frequency) and noise (at low frequency). Commonly adopted lower and upper cut-off frequencies are 20 Hz and 500 Hz, respectively.



Figure 2.1 – Examples of (a) a gelled EMG electrode and (b) a dry EMG electrode. Courtesy of Covidien (Medtronic) and Ottobock.

### Feature extraction

One of the important procedures of EMG classification is feature extraction. Representative features can determine the quality of classification results. The feature extraction process transforms raw EMG data into a set of reduced representations, called features. Feature extraction can eliminate or reduce irrelevant information and noise in the raw EMG data.

The first step of feature extraction is data segmentation. A data segment is a time window

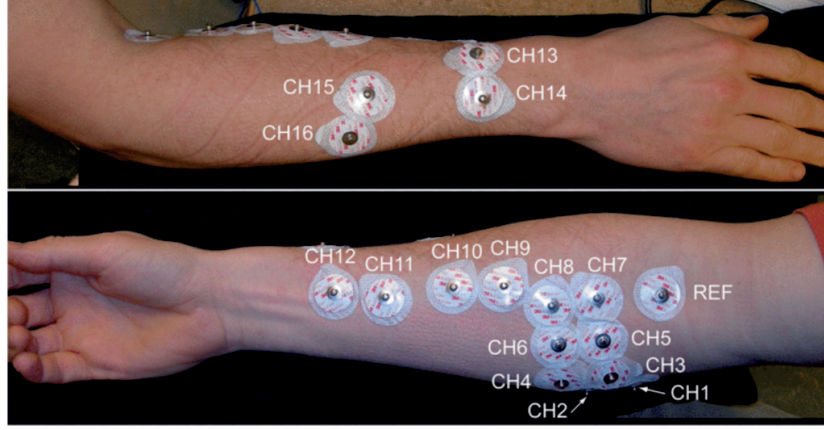


Figure 2.2 – A typical EMG collection scheme consisting of surface EMG electrodes. In this case, the collection channel is 16. Reprinted with permission from [135].

within which the features are calculated. The first proposed data segmentation scheme is the disjoint segmentation, where each data segment is arranged one after another without overlapping. Overlapping window segmentation produces a decision stream as dense as possible. Decisions are made more frequently than the required response time of a prosthesis. The filtered EMG data is then divided into different time windows (Fig. 2.3).

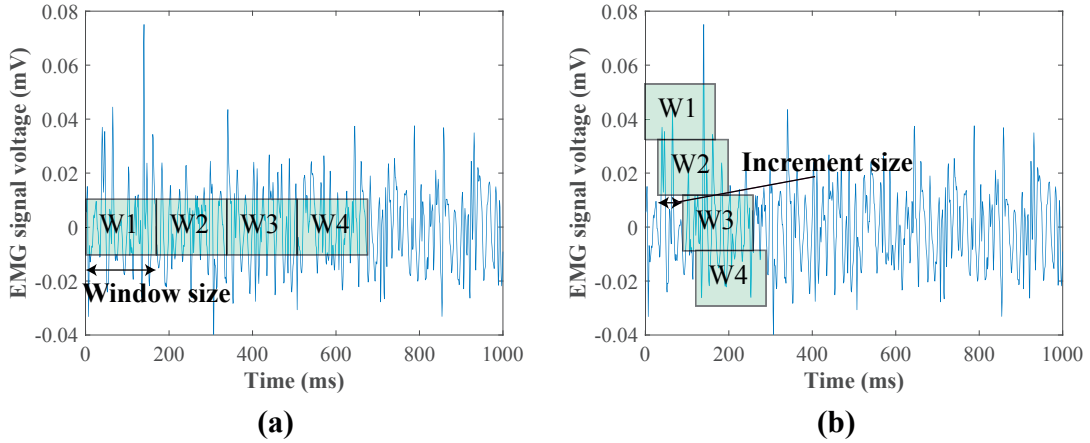


Figure 2.3 – EMG data segmentation with (a) the adjacent technique and (b) the overlapping or sliding technique.

EMG features can be classified into three categories: time-domain (TD) features, frequency-domain (FD) features, and time-frequency domain (TFD) features. TD features are preferred for real-time classification because no additional transformations are needed. FD features are based on the power spectral density of the EMG signal.

Commonly used time domain features include: mean absolute values (MAV), root mean square (RMS), zero crossings (ZC), slope sign change (SSC), waveform length (WL), auto-

## Chapter 2. Myographic Signal Pattern Recognition for Prosthetic Control

---

regression (AR) and their combinations [136, 137].

The calculations of the seven time-domain features are shown below from Eq. (2.1) to Eq. (2.8). For all the time-domain feature definitions (from (2.1) to (2.8)),  $N$  is the length of the signal and  $x_n$  is the segmented signal in the time window.

The mean absolute value (MAV) is calculated by taking the average of the absolute value of the sEMG signal and the two commonly used MAV values are: first, the standard MAV, defined as:

$$\text{MAV} = \frac{1}{N} \sum_{n=1}^N |x_n|, \quad (2.1)$$

and then modified mean absolute value: weighted MAV type I (MAV1) is defined as:

$$\text{MAV1} = \frac{1}{N} \sum_{n=1}^N w_n |x_n|, \quad (2.2)$$

where  $w_n$  is the assigned weight to improve the feature's robustness.

The root mean square (RMS) feature is the root mean square value of the EMG amplitude within the defined window. The RMS value reflects the physiological activity in the motor unit during contraction.

$$\text{RMS} = \sqrt{\frac{1}{N} \sum_{n=1}^N |x_n|^2}, \quad (2.3)$$

Zero crossing (ZC) is the number of occurrences the amplitude value of sEMG signal crosses the zero y-axis and is defined as:

$$\text{ZC} = \sum_{n=1}^{N-1} \text{sgn}(x_n \times x_{n+1}) \cap |x_n - x_{n+1}| \geq \text{threshold}, \quad (2.4)$$

$$\text{where } \text{sgn}(x) = \begin{cases} 1 & \text{if } x \geq \text{threshold}, \\ 0 & \text{otherwise.} \end{cases} \quad (2.5)$$

Waveform length (WL) is the summation of all the waveform lengths within the time segment. WL is related to the waveform amplitude, frequency, and time. It is defined by:

$$\text{WL} = \sum_{n=1}^{N-1} |x_{n+1} - x_n|. \quad (2.6)$$

Slope sign change (SSC) is the number of changes between positive and negative slope among

three consecutive segments. It is defined as:

$$SSC = \sum_{n=2}^{N-1} |(x_n - x_{n-1}) \times (x_n - x_{n+1})|. \quad (2.7)$$

Auto-regressive (AR) coefficients  $a_i$  is calculated when considering the current sample of EMG signal  $x_n$  as a linear combination of its previous samples  $x_{n-i}$  adding a white noise error  $w_n$ . AR coefficients  $a_i$  is defined by

$$x_n = \sum_{i=1}^m a_i x_{n-i} + w_n, \quad (2.8)$$

where  $m$  is the order of AR coefficients. A commonly used order is 4 or 6 [131].

### Classification

As mentioned in Chapter 1, many pattern recognition based methods have been proposed for EMG signal classification, such as: artificial neural networks (ANN) [138, 50, 51, 52], support vector machines (SVM) [139, 140, 55], linear discriminant analysis [141, 142], and k-nearest neighbors [143, 144], to name a few.

### Post-processing

The overlapping window scheme produces dense decision outputs and provides opportunities for post-processing. Post-processing has been proven to be efficient to eliminate spurious classifications. The simplest and most-widely used post-processing method is majority-voting [145]. For a given point, the majority voting considers the previous and future  $n$  points and outputs the prediction results that has the most occurrences (Fig. 2.4). Majority voting produces a smoother result and eliminate the unwanted transient jumps [55]. The choice of voting size  $n$  depends both on the processing time  $T_{pro}$  and the acceptable delay time  $T_{delay}$ .

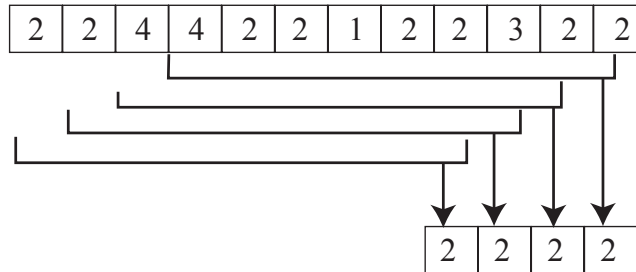


Figure 2.4 – Illustration of the majority voting processing. The voting size is 9. The number inside the window represents the class label.

## 2.2 EMG classification algorithms

Three algorithms are applied in this study: linear discriminant analysis (LDA), support vector machines (SVMs), and deep belief network. The three algorithms are chosen because they are widely used in EMG classification and they represent different types of machine learning algorithms.

The LDA is a linear machine learning algorithm. It is among fastest machine learning algorithms and the results do not depend on the selection of model parameters. LDAs are used to analyze the effects of feature selection and window/increment sizes without the bias from the model parameters.

A SVM is a non-probabilistic classifier based on the max margin principle. SVMs can efficiently perform non-linear classification problems and are suitable for large feature space classification. It is also reported to be a very robust and accurate algorithm [146, 139, 55]. It can be used as a benchmark for other algorithms. Moreover, SVMs have a relatively low number of parameters (typically two) for tuning.

A deep belief network is a special case of deep neural networks. A deep neural network is among the most commonly used machine learning algorithms in the biomedical field because it can potentially model very complex distributions and each layer within the network helps the dimension reduction of the feature space. Deep belief networks have a faster training speed compared to conventional deep neural networks and therefore are chosen for the real-time EMG classification application.

### 2.2.1 Linear discriminant analysis

The linear discriminant analysis (LDA) maximizes the ratio of the between-class variance to the within-class variance (the Fisher criterion) in any particular dataset, thereby ensuring maximal separability [147, 148]. For a binary classification problem, the Fisher criterion is defined as:

$$J(\mathbf{w}) = \frac{(\mathbf{m}_1 - \mathbf{m}_2)^2}{s_1^2 + s_1^2}, \quad (2.9)$$

where  $\mathbf{m}_1 = \frac{1}{N_1} \sum_{n \in C_1} \mathbf{x}_n$  and  $\mathbf{m}_2 = \frac{1}{N_2} \sum_{n \in C_2} \mathbf{x}_n$ .  $\mathbf{x}_n$  is the  $n^{th}$  feature vector in  $C_1$  (class 1) and  $C_2$  (class 2) with  $N_1$  samples in class  $C_1$  and  $N_2$  samples in class  $C_2$ , and  $s_1^2$  and  $s_1^2$  are the within-class variances.

The Fisher criterion can be extended to multi-classes. In a  $k$ -class classification problem ( $k > 2$ ), the Fisher criterion is defined as

$$J(\mathbf{w}) = Tr\{(\mathbf{W}\mathbf{S}_W\mathbf{W}^T)^{-1}(\mathbf{W}\mathbf{S}_B\mathbf{W}^T)\}, \quad (2.10)$$

where  $\mathbf{W}$  is the projection matrix,  $\mathbf{S}_W$  is the within-class variance, and  $\mathbf{S}_B$  is the between class covariance matrices [148]. Although an LDA can be used as a multi-class classifier, in this study, an LDA is also considered as a binary classifier and used to construct different types of multi-class classifiers using the decomposition techniques described below in Section 2.3. In total, five types of LDAs are tested: multi-class LDA, LDA-OVA, LDA-OVO, LDA-DAG, LDA-BT.

### 2.2.2 Support vector machines

An SVM is a non-probabilistic binary linear classifier, based on the maximum margin principle. The basic idea behind an SVM is to minimize the classification error rate while maximizing the geometric margin between two classes [149].

In a binary-class classification problem, given  $M$  training datasets:

$\mathbf{T}_r = \{(\mathbf{x}_1, y_1), (\mathbf{x}_2, y_2), \dots, (\mathbf{x}_M, y_M)\}$ , where  $\mathbf{x}_i \in \mathbf{R}^n$ ,  $i = 1, 2, \dots, M$ ,  $\mathbf{x}_i$  is the feature of the  $i^{th}$  training dataset,  $\mathbf{R}^n$  is the feature space,  $n$  is the feature dimension, and  $y_i$  is the training class label in the  $i^{th}$  training dataset, whereby  $c_i \in \{-1, +1\}$ ,  $i = 1, 2, \dots, M$ . The SVM training consists in solving the following optimization problem:

$$\begin{aligned} \min \quad & \frac{1}{2} \|\boldsymbol{\omega}\|^2 + C \sum_{i=1}^M \zeta_i, \\ \text{s.t.} \quad & c_i(\boldsymbol{\omega}^T \mathbf{p}_{tr} + b) \geq 1 - \zeta_i, \\ & \text{and } \zeta_i \geq 0, i = 1 \dots M, \end{aligned} \tag{2.11}$$

where  $b$  is the bias of the hyperplane,  $C$  is the penalty parameter, and  $\zeta_i$  is the slack variable.

Because the relationship between class labels (phantom digit number) and attributes (the location of sampling points) is non-linear, a non-linear kernel function is used to map the input space into a feature space for higher classification accuracy. In this paper, a radial basis function (RBF) kernel

$$K(p_i, p_j) = \exp\left(-\frac{\|p_i - p_j\|^2}{2\gamma^2}\right) \tag{2.12}$$

is chosen, because it maps the input space into Hilbert space (an infinite hyperplane) and provides more flexibility [150]. In (2.12),  $p_i$  and  $p_j$  are the features from the  $i^{th}$  and  $j^{th}$  training or classification datasets.

In general, the penalty parameter  $C$  defines the ‘softness’ of an SVM. A large  $C$  gives a high penalty for non-separable points. It tends to overfit, exaggerating minor fluctuations or noise in the data. On the other hand, if  $C$  is too small, the SVM tends to underfit, meaning that the SVM is not able to find the main trend of the underlying data. The RBF kernel parameter  $\gamma$  defines the influence of a single training dataset: a large  $\gamma$  value implies that a single example exerts great influence on the whole SVM model. Both overfitted SVMs and underfitted SVMs

produce poor prediction performance.

### 2.2.3 Deep belief network

A deep belief network (DBN) is a class of deep neural networks, consisting of multiple layers between the input and the output layers [151]. Each layer is connected, but the units within each layer are not. Each hidden layer is an unsupervised model (e.g. an autoencoder or a restricted Boltzman machine). The training of a DBN comprises a pre-training phase and a fine tuning phase. In the pre-training phase, a deep belief network generates a multi-layer connected model. The autoencoders are trained using an unsupervised learning method. The hidden layer also works as dimensionality reduction. Compared to other deep neural network architectures, DBN has a faster training speed because of the layerwise-greedy training, instead of whole network optimization. After pre-training, the fine tuning is processed using back propagation. In the current study, autoencoders were chosen as hidden layers.

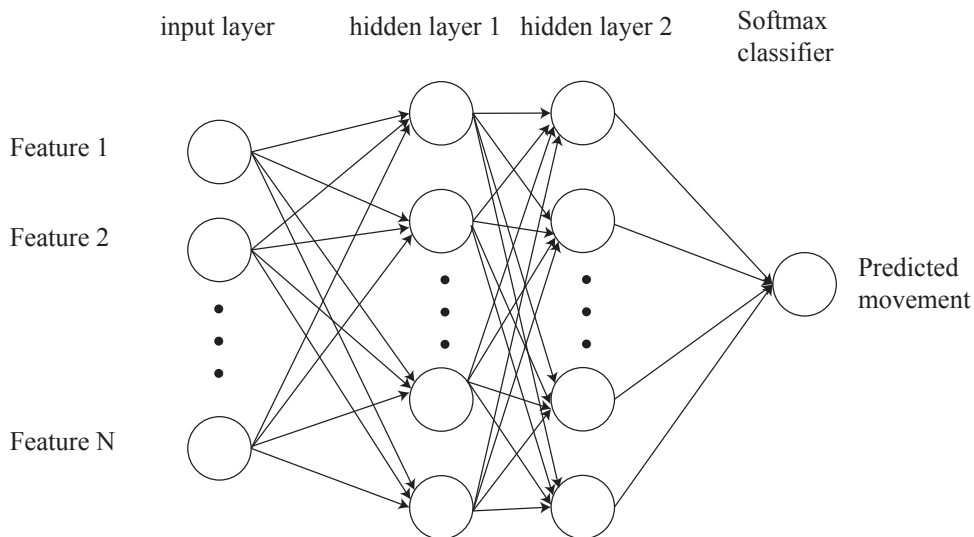


Figure 2.5 – The deep belief network architecture used in the current study. It consists of two stacked autoencoders and a softmax classifier at the output.

## 2.3 Decomposition methods to construct multiclass classifiers

Decomposition method is an effective approach to extend binary classifiers into multi-class classifiers. This method decomposes a multi-class classification problem into several binary problems [152]. Four main decomposition methods are proposed: the one-VS-all (OVA), the one-VS-one (OVO), the directed acyclic graph (DAG), and the binary tree (BT) method.

**OVA** The principle of OVA is to train each class against all the rest of the classes [153]. When training the  $i^{th}$  class, all the training samples belonging to  $i^{th}$  class is assigned positive labels; while the others are assigned negative labels. After training all the binary classifiers, the final predicted class is the one with the highest output margin.

**OVO** For OVO, all the classes are trained against each other [154]. For a  $k$ -class classification problem, each binary classifier determines a preferred class. After training all the  $k(k-1)/2$  classifiers, the predicted class is the one that has the most votes.

**DAG** The training of a DAG multi-class classifier is the same as an OVO multi-class classifier [155]. In the classification phase, the  $k(k-1)/2$  classifiers are arranged according to a directed acyclic graph (DAG). A test sample starts from the root node and goes to either the left or the right child node until a leaf node is reached and a class label is decided.

**BT** The basic idea of a BT-SVM is to partition the multi-class problems hierarchically [156]. Each partition results in a binary classification problem between two meta-classes. For a  $k$ -class classification problem, a BT multi-class classifier needs to train  $k-1$  binary classifiers. During classification phase, an evenly-distributed BT multi-class classifier needs only  $\log_2 k$  binary classifier to decide the class label of a testing sample.

## 2.4 Methods

In this section, we first introduce three datasets, including different aspects of upper limb movement used in this study. Then the classification setup including descriptions of three classification experiments is given. The last part describes the evaluation methods.

### 2.4.1 Datasets description

Three datasets were tested to cover different types of movement: individual finger movement [135], hand movement (CapgMyo dataset [157]), and wrist movement (MEC dataset [158]). Ten classifiers were evaluated for each subject in each datasets: LDA, LDA-OVA, LDA-OVO, LDA-DAG, LDA-BT, SVM-OVA, SVM-OVO, SVM-DAG, SVM-BT, and DBN. Classifiers were trained on the extracted features introduced in Section 2.1.

#### Individual finger movement

Five able-bodied and three transradial upper limb amputees participated in the data collection. The EMG signal was collected using a modified version of a custom-made amplification and acquisition system [135] and a LabView program. The sEMG signal were collected through 16

channels (Fig. 2.6 (a)), sampled at 1.6 kHz per channel, with a band-pass filter between 0.5 Hz and 800 Hz. The individual finger movement dataset consists of 12 finger movements and a rest class. The movements used for classification in this study include: thumb flexion, index finger flexion, middle finger flexion, ring finger flexion, little finger flexion, thumb opposition, thumb extension, index finger extension, middle finger extension, ring finger extension, little finger extension, and thumb abduction. This means flexion and extension of each individual finger as well as thumb adduction/abduction.

### CapgMyo

The CapgMyo dataset [157] was collected using a 128 ( $8 \times 16$ ) channel high-density matrix-type differential sEMG electrode array (Fig. 2.6 (b)). Eight hand gestures and one resting phase were obtained from 18 able-bodied subjects, aged between 23 and 26 years old. The performed gestures include: thumb up, extension of index and middle finger, extension of the thumb, index, and middle finger, thumb opposition the base of the little finger, all fingers abduction, fist, index finger pointing, and abduction of extended fingers. Each subject participated in two recording sessions on different days, with an inter-recording interval greater than one week. Each gesture was held for three seconds [159].

### MEC

The MEC dataset [158] was collected through an eight-channel EMG data acquisition system. The electrodes were evenly distributed along the volar and dorsal side of the forearm (Fig. 2.6 (c)). This dataset consists of six forearm movements and one resting phase of EMG data collected from 20 healthy subjects. The six forearm motions include: hand open, hand close, wrist flexion, wrist extension, supination, and pronation. Each subject participated in four sessions and each session consist of six trials. In this study, we investigated both within-session classification results and inter-session classification results. For the within-session classification, the first three trials were used for training, the classification algorithms and the remaining three were test data. For the inter-session classification, the first two sessions were used for training while the rest were used for testing.

A summary of the three datasets is shown in Table 2.1.

### 2.4.2 Classification setup

The algorithms are tested using the aforementioned three datasets. A sliding window scheme with different window sizes and increment sizes is applied. The features considered in this study are time-domain features introduced in Section 2.1. Majority-pooling post-processing techniques are also employed.

All the feature extraction and machine learning algorithms are implemented in MATLAB 2017b.

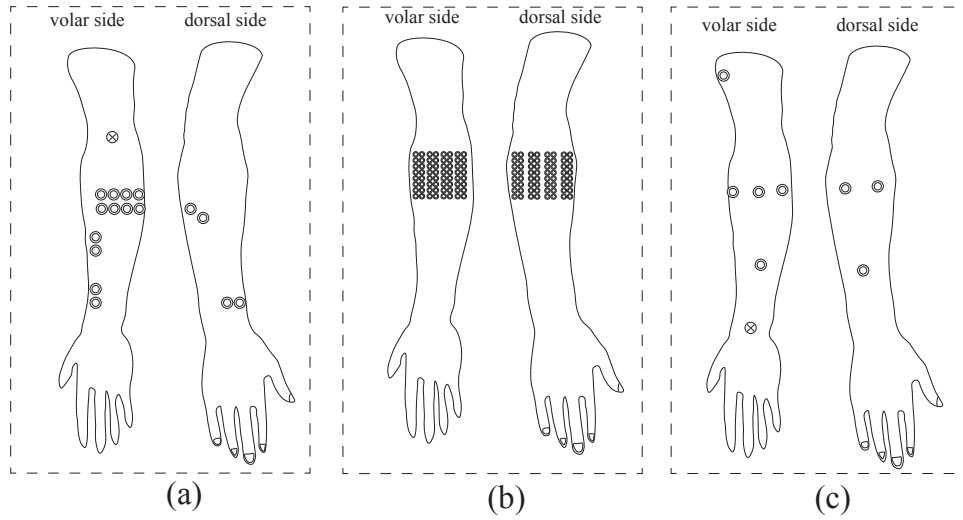


Figure 2.6 – The EMG electrodes placement used in the EMG acquisition for the three datasets used in this study. (a) The individual finger movement dataset [135] was collected through 16 EMG channels. (b) The CapgMyo dataset [157] was collected through an 128 (8 strips of 16 channels) high density EMG channels. (c) The MEC dataset [158] was collected through 8 channels. The stars represent the reference electrodes.

Dataset name	Individual finger movement	CapgMyo	MEC
Subjects	5 able-bodied subjects, 3 transradial amputees	18 able-bodied subjects	20 able-bodied subjects
Sampling frequency	1.6 kHz	3 kHz	1 kHz
No of channels	16 channels	128 channels	8 channels
Performed movements	12 individual finger movement + 1 resting phase	8 hand gestures + 1 resting phase	6 forearm movement + 1 resting phase (The dataset is reorganized)

Table 2.1 – Summary of the three EMG datasets used in this study.

The algorithms are running on a Lenovo T440s laptop, with Intel Core TM i7-3520M (2.9GHz, 4MB L3).

This study consists of the following three experiments.

*Experiment 1: Select feature or feature combinations*

The first experiment is to select suitable time-domain features. During this experiment, the seven aforementioned time-domain features and the all their possible combinations (127 in

## Chapter 2. Myographic Signal Pattern Recognition for Prosthetic Control

---

total) are applied for all three datasets and the classification results using LDAs are presented below in Section 2.5.1.

*Experiment 2: Evaluate the influence of window size and increment size*

After selecting several suitable feature(s) or feature combinations, during experiment 2, different window sizes ranging from 25 ms to 300 ms and corresponding increment sizes are evaluated using LDAs and the results are presented in Section 2.5.2.

*Experiment 3: Test the effectiveness of each classification algorithm*

In this experiment, the aforementioned algorithms (introduced in Section 2.2), together with the decomposition techniques (introduced in Section 2.3), are tested on the datasets. The accuracy and real time performance aspects are compared in Section 2.5.3.

### 2.4.3 Evaluation methods

#### Accuracy definition

Two types of accuracy are defined. The first type (Type I accuracy)  $x_1$  is the grand average accuracy, where the accuracy is calculated considering all the mis-classifications, regardless of the original class:

$$x_1 = \frac{\sum_{i=1}^N N_i}{N}, \quad (2.13)$$

where  $N$  is the total number of test samples and  $N_i = 1$  if, for test sample  $i$ , the predicted result is the same as the correct testing label.

The second type of accuracy (Type II accuracy)  $x_2$  is the accuracy over all classes, in order to minimize the bias of unbalanced data. Type II accuracy  $x_2$  is defined as:

$$x_2 = \left( \frac{\sum N_{i,j}}{N_j} \right), \quad (2.14)$$

where  $N_j$  is the number of test samples belonging to class  $j$  and  $N_{i,j} = 1$  if for test sample  $i$ , the predicted result is the same as the correct testing label and it belongs to class  $j$ .

#### Real time evaluation metrics

The classifiers are also evaluated regarding their real-time performances. Four types of real-time metrics are used to evaluate the classification performance: response time, motion completion time, dynamic efficiency, and motion completion rate. The response time is the delay between the change of movement and the first correct prediction results. The motion completion time is the time between response time and the first correctly identified  $M$  points.

In this study,  $M$  is chosen as 20. If the movement contains at least  $M$  correctly identified points, this movement is regarded as complete. Motion completion rate is the ratio between complete movements and the total performed movements. Dynamic efficiency is total number of correct responses during the motion completion time over the motion completion time.

## **2.5 Classification results**

The EMG classification results are evaluated regarding their classification accuracy and real-time performance, defined in Section 2.4.3.

### **2.5.1 Feature selection**

This study used seven time-domain features. First, each feature and their combinations were tested using the LDA because the LDA is a fast classification algorithm and the classification results would not be biased by parameter tuning.

The results are shown in Fig. 2.7. The dataset presented here is the individual finger movement dataset. The chosen window size is 150 ms with 50 ms increment size. Other datasets and different window and increment sizes are also considered and they showed similar trends like in Fig. 2.7.

From Fig. 2.7, it can be observed that as the number of features grows, both the classification and real time performance improves, at the cost of longer feature extraction time. To further evaluate the effectiveness of feature and feature combinations, some of the best performed and representative features were selected and used in all the algorithms across the three datasets. These features include: MAV for its short calculation time and high classification accuracy, MAV + MAV1 + RMS + WL for its balance between classification accuracy and calculation time, MAV + RMS + ZC + SSC + WL + AR(6) (referred as TDAR(6) [160] for the rest of the chapter) for its high classification accuracy, MAV + MAV1 + RMS + ZC + SSC + WL + AR(6) for its completeness.

### **2.5.2 Influence of window and increment sizes**

There is a trade-off in selecting window sizes: large window sizes can incorporate more information but also more likely to introduce noise, especially at the movement transaction phase, as well as reducing response speed.

The first experiment focuses on evaluating the influence of window sizes. In this experiment, the increment size is fixed at 10 ms and the window size ranges from 10 ms to 300 ms. The classification results are shown in Fig. 2.8.

The classification accuracy is largely degraded when the window size is smaller than 150 ms.

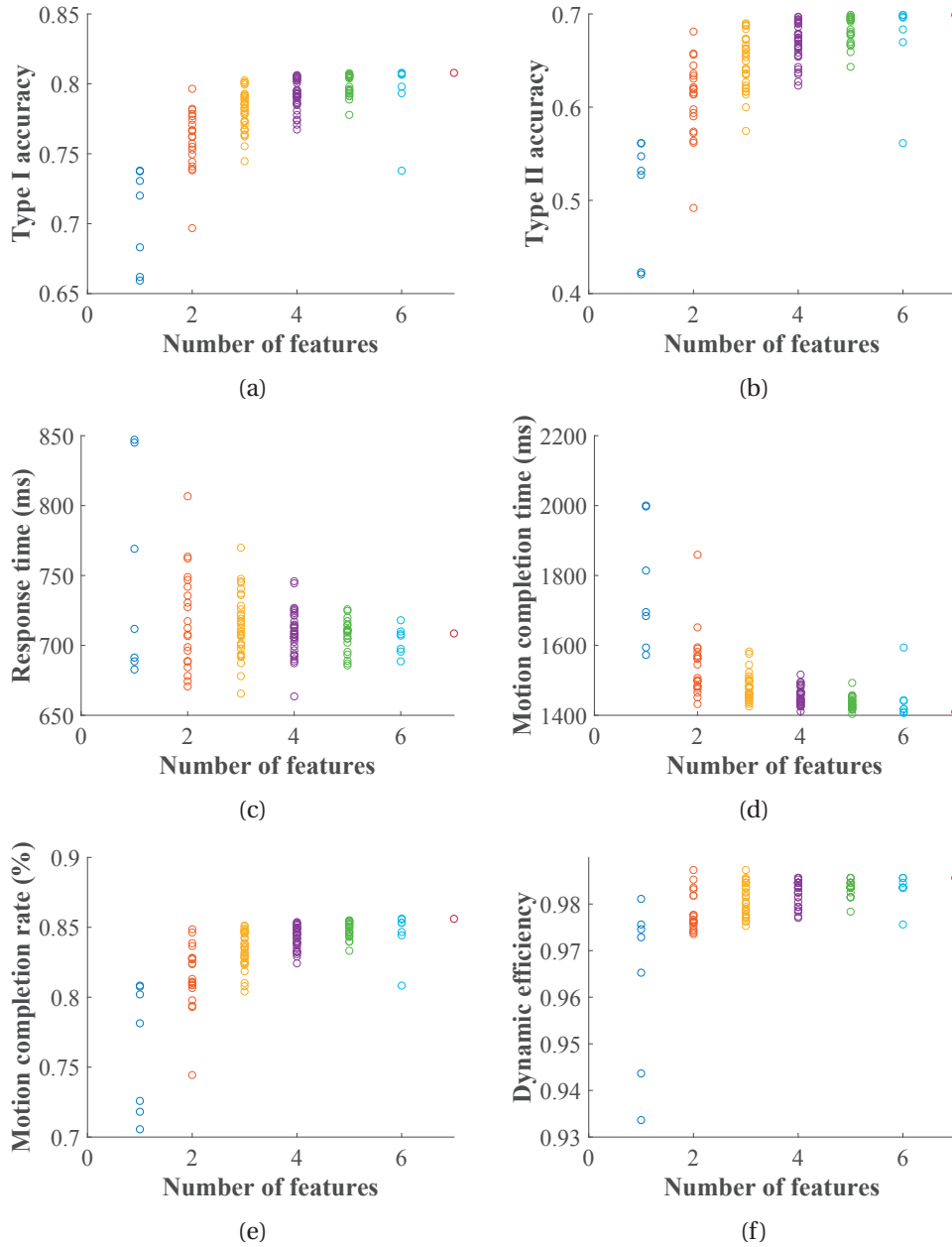


Figure 2.7 – The accuracy and real-time metrics of different features and feature combinations. The x-axis represents the number of features. The chosen window size is 150 ms with 50 ms increment size. The used dataset is the individual finger movement dataset.

When the window size is larger than 150 ms, the accuracy increase slows down (Fig. 2.8 (a) and (b)). The response time increases linearly with the window sizes (Fig. 2.8 (c)), however, the motion completion time (Fig. 2.8 (d)) and motion completion rate (Fig. 2.8 (f)) reaches the saturation when the window size is larger than 150 ms.

The second experiment considered the influence of increment sizes. Fig. 2.9 shows the classi-

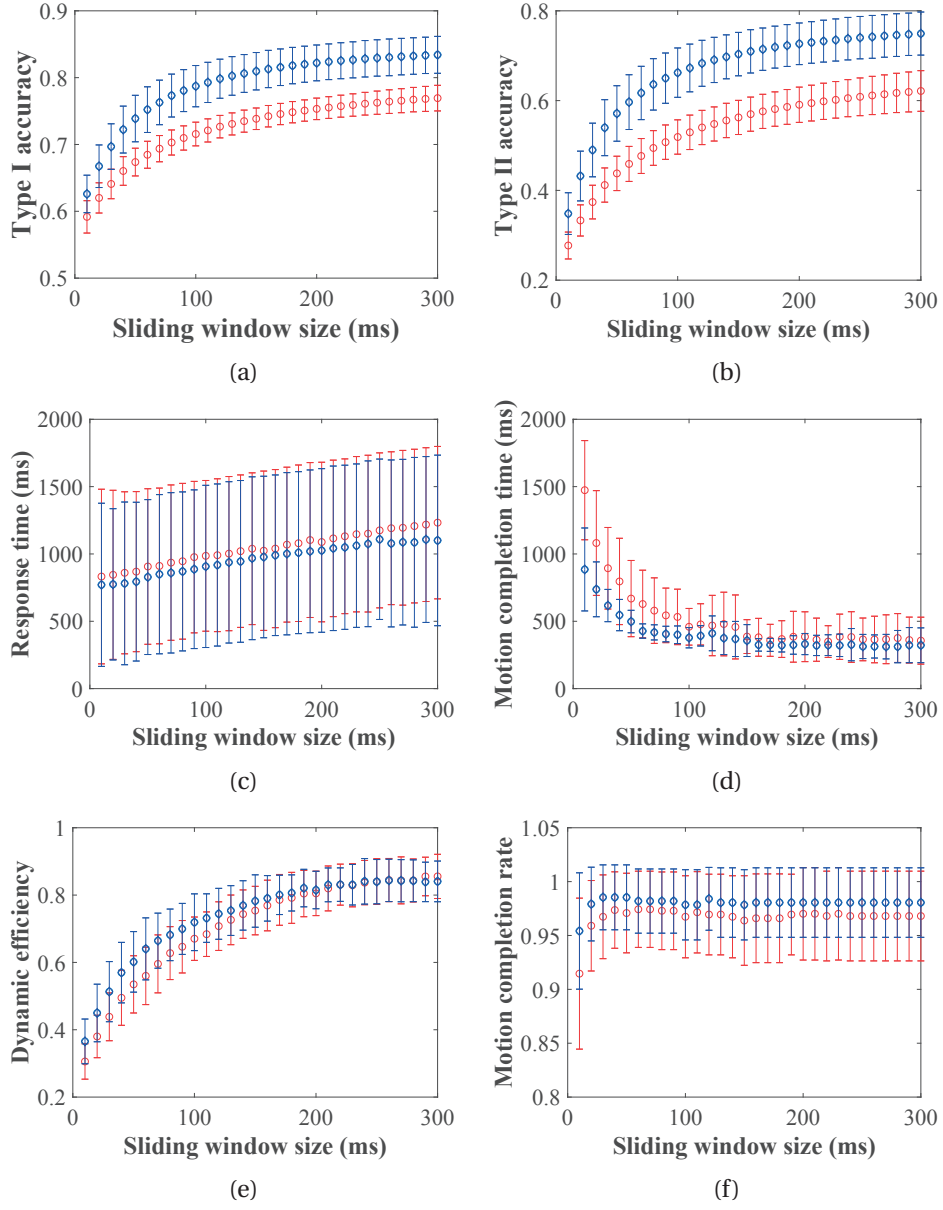


Figure 2.8 – The accuracy and real-time metrics when using different window sizes. The increment size is fixed at 10 ms. The x-axis is the window size. The dataset shown is the individual finger movement. Two types of features were used: MAV (plotted in red) and TDAR(6) (plotted in blue).

fication results using individual finger movement dataset with the increment sizes ranging from 10 ms to 150 ms. The window size is 150 ms.

In Fig. 2.9 (a) and (b), as the window size increases, the accuracy increases slightly, though no significant differences are detected.

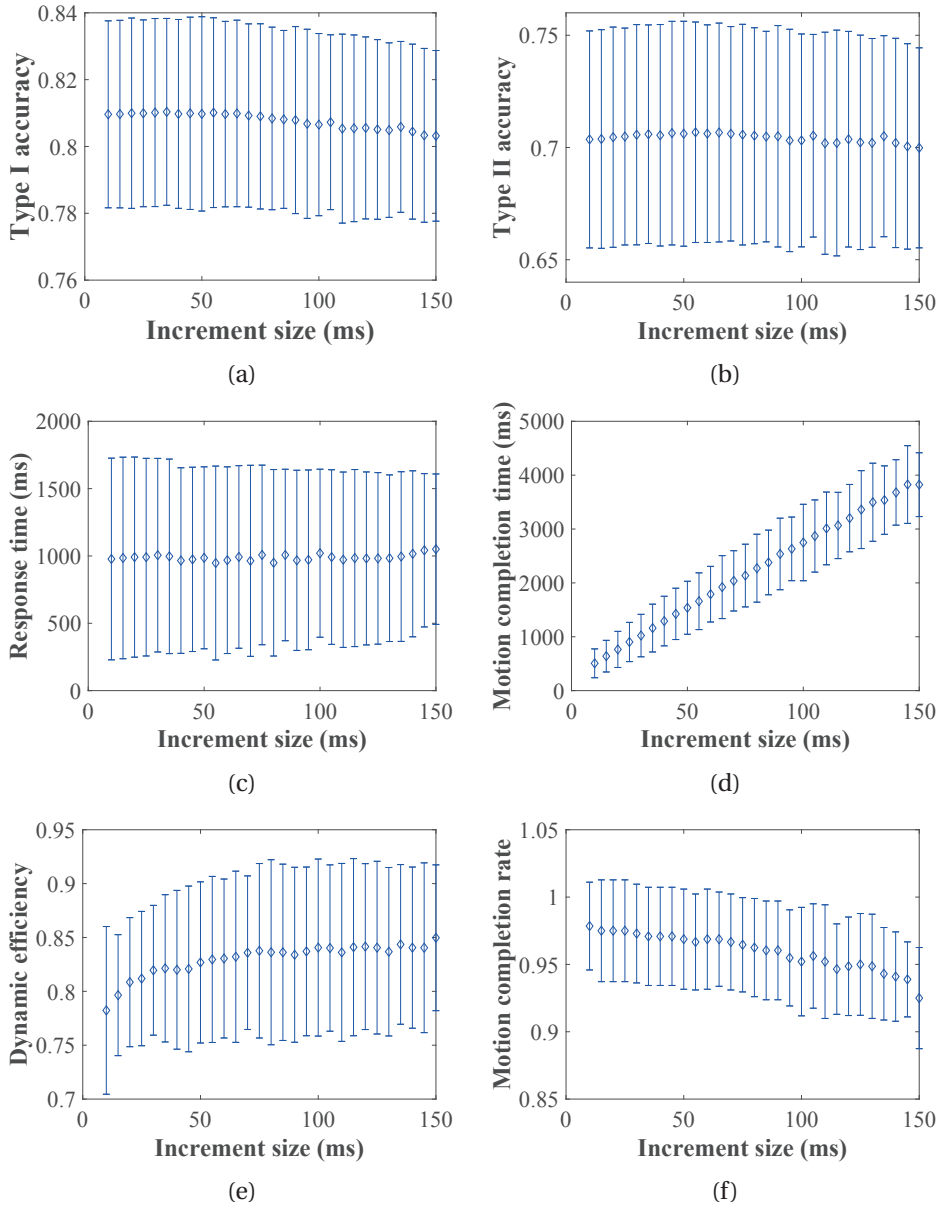


Figure 2.9 – The accuracy and real time performance results of EMG classification. The example dataset is the individual finger movement. The window size is fixed at 150 ms. The feature set is TDAR(6). The other feature sets and different window sizes have shown similar trends. The error bars represent the standard derivatives.

The change in increment sizes have a higher impact on the real time performances. Even though the number of sliding windows are reduced as the increment size increases, the actual needed time is increased (Fig. 2.9 (c) and (d)).

The motion completion rate also decreases as the increment size increases (Fig. 2.9 (f)).

### 2.5.3 Influence of classification algorithms

s In this subsection, the results of the individual finger movement and CapgMyo EMG dataset (introduced in Section 2.4.1) using different algorithms (introduced in Section 2.2) are presented in Fig. 2.10 and Fig. 2.11.

From Fig. 2.10 and Fig. 2.11, it can be observed that there is some performance variation within different datasets. For an individual finger movement dataset, the classification accuracy, both type I and type II, is in general lower than that of the CapgMyo dataset. For CapgMyo dataset, SVM-OVA with the feature combination of 7 features produces the highest type I accuracy (92.2+1.81 %), while for individual finger movement, LDA with the feature combination of 6 features obtains the highest type I accuracy (80.9+2.84 %). This can be explained by the channel numbers. As described in Section 2.4.1, the individual finger movement dataset was collected through 16 channels and the CapgMyo dataset was collected through 128 channels. When using combined features, the feature space increases linearly to the number of channels and the number of features. One of the advantages of SVMs is the ability to effectively classify high-dimensional datasets, thus it out performs LDAs when using a high dimensional EMG collection system.

From the previous feature selection experiment, feature combination TDAR(6) shows similar though slightly lower classification accuracy when using LDA. However, it shows higher classification accuracy when using DBN. In general, the overall seven feature combination shows the best performance for most of the algorithms tested with higher classification accuracy, lower response and motion completion time, and higher or equal motion completion rate.

### 2.5.4 Techniques to improve classification accuracy with unbalanced training data

It has been empirically proven that when the training data become more imbalanced, the support vectors are prone to produce biased classification results by favoring the majority class(es) [161]. The minority classes are normally given less importance and thus the classification accuracy on the minority classes suffers from the global optimization. For two of the datasets used, in the training dataset, the resting classes occurs much more often than the other movement classes (more than 5 times)s.

Resampling methods have been proven to be successful in dealing with imbalanced datasets. In this study, two commonly used resampling schemes are tested: oversampling and downsampling. For the two highly imbalanced datasets, oversampling has shown improved accuracy at the cost of longer training time. Although the discussion above mainly concerns SVMs, the results indicate that LDAs also benefited from oversampling with increased type II accuracy.

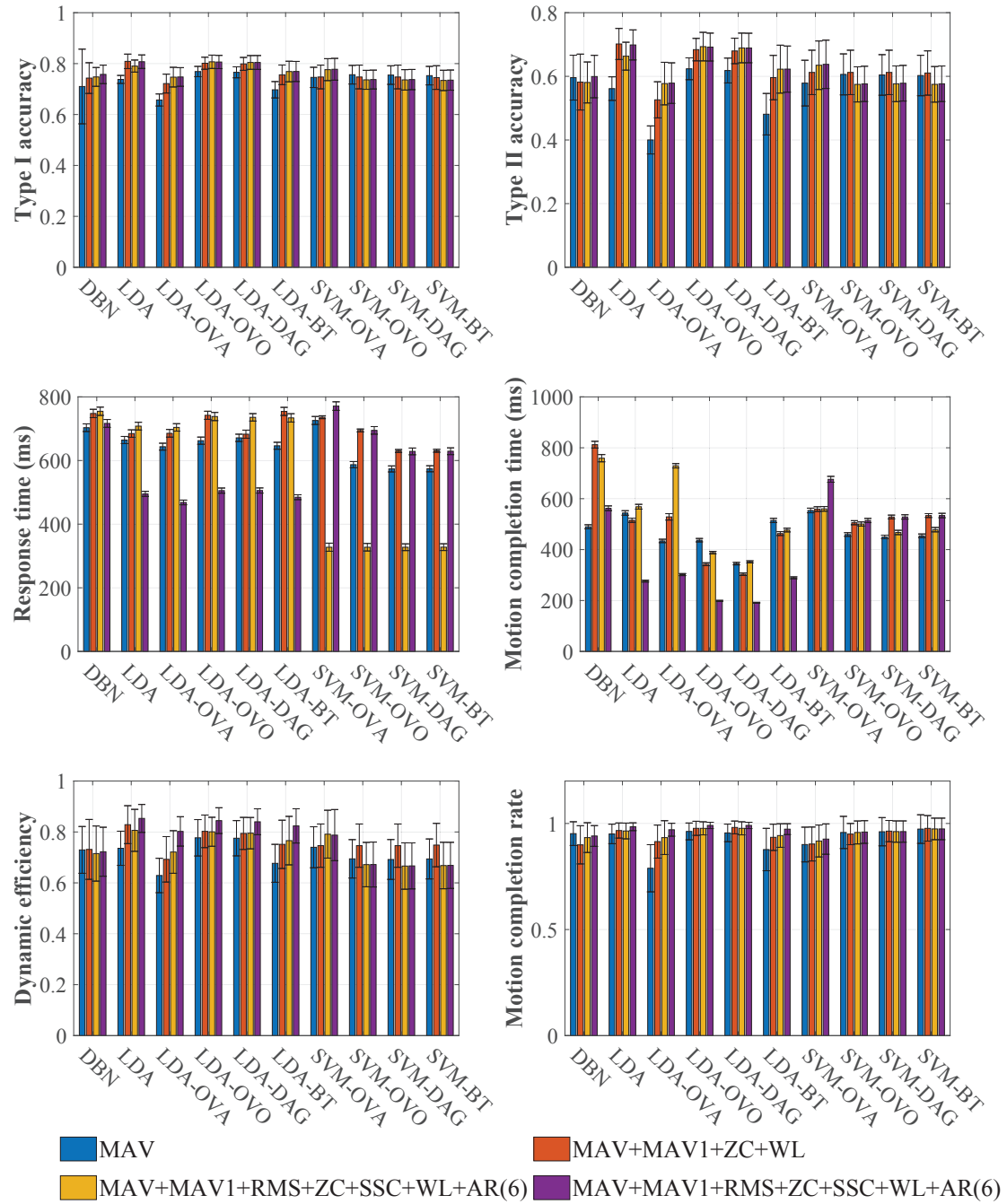


Figure 2.10 – The accuracy and real-time metrics of different algorithms and four feature/feature combinations of individual finger movement dataset. The error bars indicate the standard derivatives. The applied window size is 150 ms with 50 ms increment size.

### 2.5.5 Influence of principle component analysis

Principal component analysis (PCA) is a statistical procedure that uses an orthogonal transformation to convert a set of observations of possibly correlated variables into a set of values

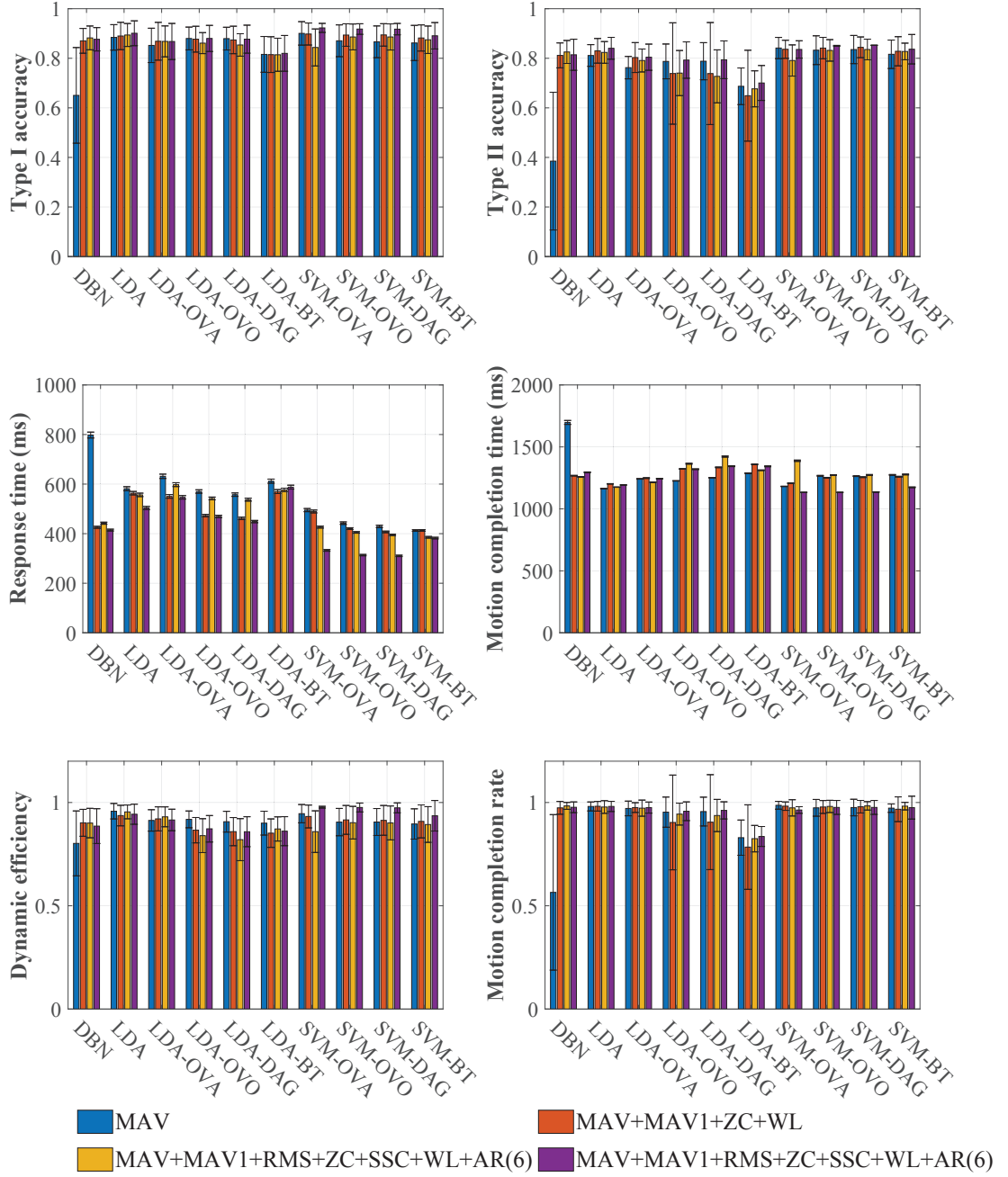


Figure 2.11 – The accuracy and real-time metrics of different algorithms and four feature/feature combinations of CapgMyo (hand gesture) dataset. The error bars indicate the standard derivatives. The applied window size is 150 ms with 50 ms increment size.

of linearly uncorrelated variables called principal components. In this study, the PCA is also applied to each dataset for dimensional reduction and hopefully with improved results. For the three datasets tested, only CapgMyo dataset has improved performance (higher accuracy,

higher dynamic efficiency, and higher motion completion rate) when the dimension reduction is less than 50 %. For the other two datasets, the original dimension is not high, thus, the added PCA does not improve the performance.

### 2.5.6 Post-processing

In this study, majority voting post-processing (introduced in Section 2.1) is applied. The representative results with different voting size is presented in Fig. 2.12. In Fig. 2.12, only the results using OVA-SVM with 150 ms and 25 ms were shown. However, the results from other algorithms and data sets showed similar trends.

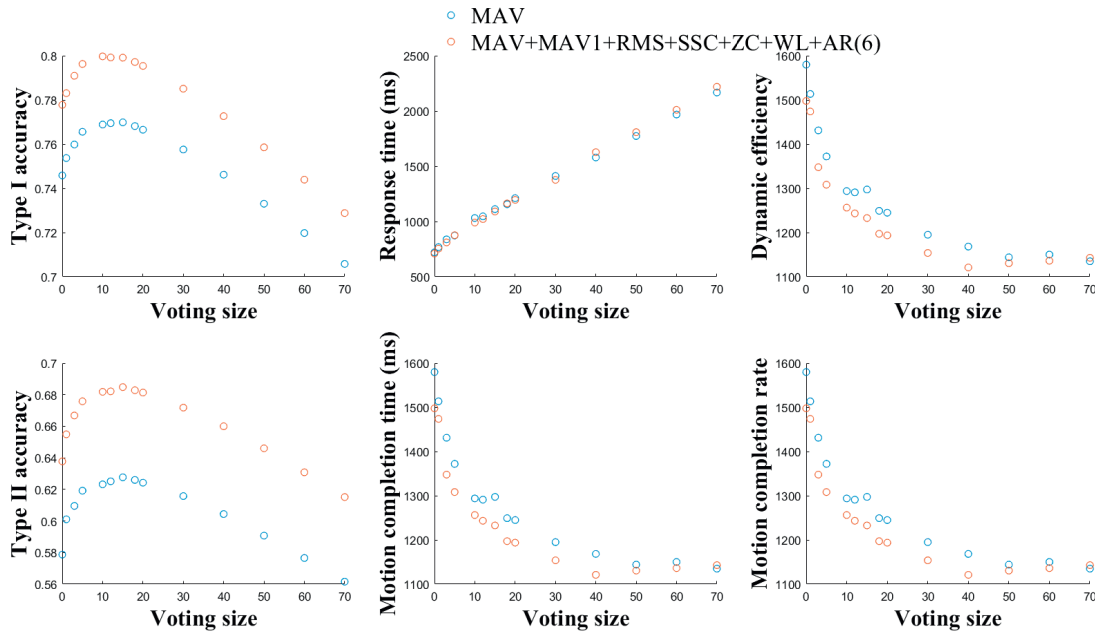


Figure 2.12 – The accuracy and real-time metrics of individual finger movement data set after majority voting.

Comparing the effects of majority voting on the two datasets, the main difference is the change in Type I accuracy. However, because Type II accuracy is a more realistic measure for real life usage, we will mainly focus our discussion on Type II accuracy, which shows the same trend in both datasets. Even though the Type II accuracy increases when the voting size is smaller than 15, the real time performance is compromised: the response time increases linearly with the voting size, the motion completion rate and the dynamic efficiency both decrease dramatically.

In our specific case, the voting size between 10 to 15 is a good trade-off between real-time performance and accuracy.

## 2.6 Summary

The purpose of this study is three-fold: to assess the commonly used time-domain features, to evaluate the influence of sliding window segmentation length and increment length, and to investigate the effectiveness of different algorithms.

Firstly, this study systematically tested seven commonly used time-domain features and their combinations regarding the classification accuracy and real-time performance using different types of algorithms across three EMG datasets. Most of the results were consistent for all algorithms and datasets. In general, feature combinations provide higher classification accuracy (both type I and type II), higher motion completion rate, and higher dynamic efficiency, compared to those of single features. The response time and motion completion time are not necessarily longer when feature combinations are used. However, combined features did require longer feature extraction time, training, and classification time, because of the increased feature dimensions.

The second focus of the study is to examine the influences of sliding window sizes and increment sizes on the classification performance. The results indicate that the window sizes have a high impact on the classification accuracy: smaller window sizes tend to be biased and produce unoptimized classification results. By selecting a larger window size, sometimes even a simple feature can outperform a feature combination which uses a smaller window size. Moreover, the results indicated that increment size has negligible influence on the classification accuracy and plays a more important role in the real-time performance. Larger increment size leads to longer response and motion completion time. If computational power allows it, the increment size chosen should be as small as possible.

We also compared the influence of different algorithms paired with selected feature or feature combinations based on the previous simulation results. Generally speaking, SVMs have higher accuracy, faster response speed, and higher motion completion rate when the feature space is large. In other cases, there is no significant advantages for using SVMs.

Furthermore, majority voting is applied as a post-processing technique to further increase the classification accuracy. It can be observed that there is a trade-off between classification accuracy and real-time performance. When a voting size is chosen properly (in our case, between 1 and 15 window sizes), the classification accuracy increases at the cost of longer response time.

As has been observed in our classification results, the inter-datasets variations are large. The classification results also depend on electrode placement, skin condition, and personal differences. Therefore, there is a difference when attempting to compare our classification results directly to other reported EMG classification results, because of the use of different datasets. However, within the scope of our research, we have proven high classification accuracy within acceptable delay.

## **Chapter 2. Myographic Signal Pattern Recognition for Prosthetic Control**

---

The findings of this study can serve as a reference when choosing the EMG time domain features, selecting window or increment sizes. This study offers some insights for the practical development of dexterous myoelectric prostheses.

## 3 Automatic Hand Phantom Map Generation and Detection

The previous chapter introduced some methods for pattern-recognition-based prosthesis control (the feed-forward path). This chapter will focus on the first step of non-invasive sensory feedback design: defining the phantom map shape distribution. The phantom map phenomenon is a region on the body that can evoke a feeling of the lost hand [162, 163]. We propose to use support vector machines (SVM) for a fine grained phantom map detection. This chapter is organized as follows: Section 3.1 explains the phantom map phenomenon and gives a short introduction on how to use machine learning algorithms for phantom map detection. The phantom map databases are described in Section 3.2. The databases are used to verify the proposed algorithms. The third section presents three sampling methods for SVMs (Section 3.3). The fourth section introduces different decomposed support vector machines applied in automatic phantom map detection (Section 3.4). Their accuracy and timing aspects are presented and compared in Section 3.5. Finally, the results are summarized in Section 3.6.

### 3.1 Hand phantom map introduction

The phantom map phenomenon is also called referred sensation in the literature. For many upper limb amputees, their phantom maps exist on their remaining stumps or their faces. Phantom maps were reported to be developed shortly after amputation [164, 165, 166, 167]. Half of the developed phantom maps will stay stable in the long term [164]. Phantom maps can serve as an area for providing targeted and natural sensory feedback because they are modality-specific, and intrinsically linked to the lost fingers [168, 169, 170]. Providing sensory feedback on the phantom map has also shown to relieve phantom limb pain [70] and reduce the mental workload [168].

The most widely accepted phantom map formation theory is cortical topography reorganization [164]. After amputation, on the Penfield map (Fig. 3.1), the regions representing the arm and face invade the hand area, which is located between the two invading regions [171, 164], thus establishing the phantom map.

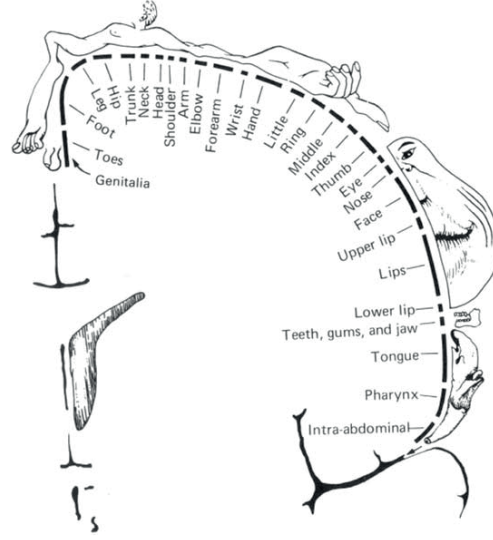


Figure 3.1 – Penfield map i.e. a human body representation in the brain [172]. On the Penfield map, the area representing the hand in the brain is bordered by the face and arm regions.

Due to uncontrollable cortical reorganization after amputation, phantom map shape and sensitivity vary from person to person [173, 168] and can also change over time [164]. The current approach for phantom map detection is based on palpation, after which a rough phantom map is drawn on the remaining stump of the amputee. The defined phantom map is quite rudimentary, inconsistent, and inaccurate. Though this roughly defined phantom map is sufficient for current sensory feedback arrays (one actuator per phantom finger), a more detailed and refined phantom map shape distribution will be needed when a dense stimulation array is applied.

In the current study, we introduce an automatic phantom map detection algorithm. Given a limited number of training data, this algorithm predicts the phantom finger distribution of an unknown phantom map. This algorithm consists of three steps: sampling, training, and classification (Fig. 3.2).

The training data sets and classification feature sets are defined before proceeding to the algorithm descriptions. The training data sets consist of training features and training classes. They are used to train a machine learning algorithm model. The classification feature sets will then be fed into the trained model and each testing feature set will be assigned a class label, during the classification phase.

The training data sets collection  $\mathbf{Tr}$  is defined as

$$\mathbf{Tr} = \{(\mathbf{p}_{tr,1}, c_{tr,1}), \dots, (\mathbf{p}_{tr,M}, c_{tr,M})\}, \quad (3.1)$$

where  $\mathbf{p}_{tr,i}$  is the training feature (the location of the data points within a phantom map), with  $\mathbf{p}_{tr,i} = (x_i, y_i)$ ,  $x_i$  and  $y_i$  being the coordinates of point  $i$  in a phantom map matrix,  $M$  is the

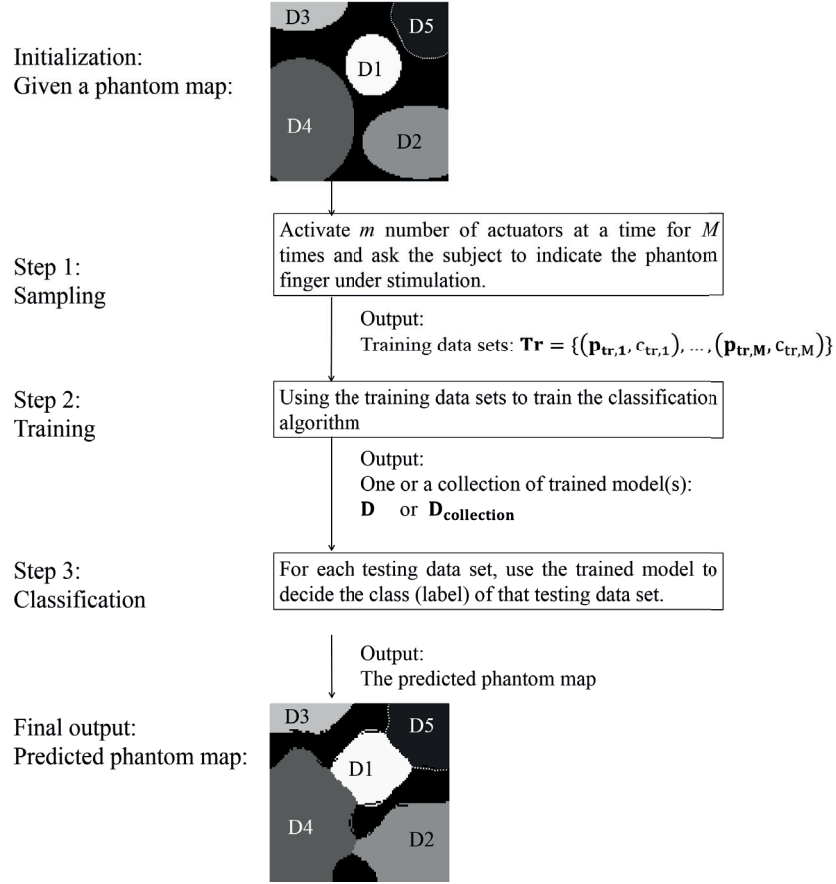


Figure 3.2 – Automatic phantom map detection flow. The detection algorithm includes: sampling, training, and classification. The final output is the predicted phantom map. In this work, the amputees are assumed to always give the right answer.

number of training data sets, and  $c_i$  is the class label ( $c_i \in \{0, 1, 2, 3, 4, 5\}$ , corresponding to no phantom sensation, phantom thumb, index, middle, ring, and little finger,  $i = \{1, 2, \dots, M\}$ ).

The classification feature sets collection is defined as

$$\mathbf{P}_{tst} = \{\mathbf{p}_{tst,1}, \dots, \mathbf{p}_{tst,10000}\}, \quad (3.2)$$

whereas the collection of testing classes is defined as

$$\mathbf{C}_{tst} = \{c_{tst,1}, \dots, c_{tst,10000}\}, \quad (3.3)$$

where  $c_{tst,1} \in [0, 1, 2, 3, 4, 5]$ . For each individual phantom map,  $M$  selected points are sampled and used to train the SVMs. Due to the different outliers of each phantom map, every phantom map needs its individual training and classification.

### 3.2 Hand phantom map databases

Two databases are introduced in this section to test the phantom map detection algorithms: the first database consists of generated phantom maps using a contour model (Section 3.2.1), whereas the second database is based on processed and transformed reported phantom map images (Section 3.2.2).

#### 3.2.1 Hand phantom map model generation

Realistic phantom maps are generated to test the phantom map detection algorithms (Fig. 3.2: Initialization). From the reported phantom maps, and our own observations, it can be concluded that phantom maps have clear and smooth edges [170, 168]. Repeated phantom digits and phantom finger overlaps were also reported [168]. Some amputees have a complete phantom map (all five phantom fingers exist) while other amputees have only partial phantom maps (one or more phantom fingers are missing) (Fig. 3.3). Moreover, it is also observed that when several phantom digits are touched simultaneously, the amputee can distinguish all the digits that are being touched.

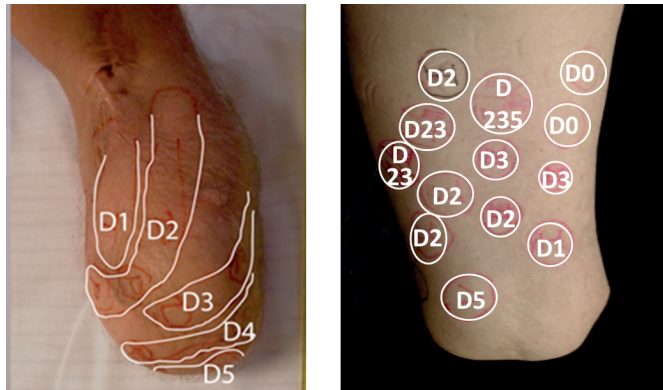
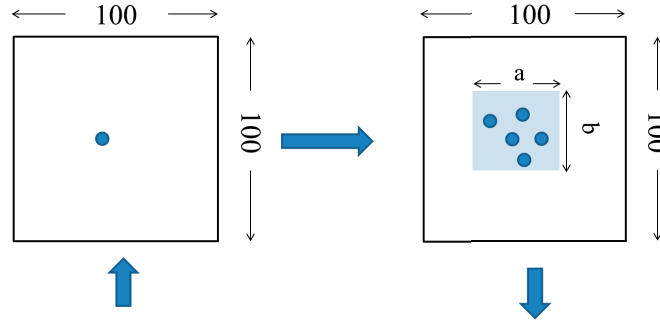


Figure 3.3 – Two real phantom map examples. Left: a complete phantom map with five phantom digits: D1 to D5 represent thumb, index, middle, ring, and little phantom finger, respectively. The phantom map shapes were detected by palpation [170]. Right: a complete phantom map with either shared phantom fingers or indistinguishable phantom fingers under testing conditions (touching with a pen). D0 represents tested areas without phantom sensation. D23 and D235 represent shared phantom sensation areas [168].

For simplification, it is assumed that phantom digits do not overlap. The phantom map model is formulated as a  $100 \times 100$  matrix  $A$ , considering the typical area of the remaining stump and the minimum two-point discrimination distance. Each cell in the matrix is assigned a number from  $[0, 1, 2, 3, 4, 5]$  using a contour model, where zero represents no phantom sensation and the numbers 1 to 5 represent phantom thumb, phantom index, phantom middle, phantom ring, and phantom little finger, respectively (Fig. 3.4). Firstly, the generation algorithm selects 4 to 5 cells randomly within the given  $a \times b$  window (Fig. 3.4: step 1 and 2) (for 5 finger phantom maps,  $0 < a, b \leq 60$  and for 10 finger phantom maps,  $0 < a, b \leq 45$  to accelerate

the convergence speed). The selected cells are then connected by an active snake contour model (Fig. 3.4: step 3) [174]. The contour defines the boundary of a phantom finger by assigning a number to all the cells inside the contour, starting from 1 (Fig. 3.4: step 4). Then the generation algorithms repeat this procedure until the required phantom fingers are assigned (Fig. 3.4).

1. Randomly select an element within the available space ( $100 \times 100$  matrix) representing the stump area.
2. Select 3 or 4 more points within an  $a \times b$  window.



3. Use snake contour model to generate an edge that connects all selected points.
4. Assign a phantom finger number to the area defined by the edge and mark this space as unavailable for the next iteration.

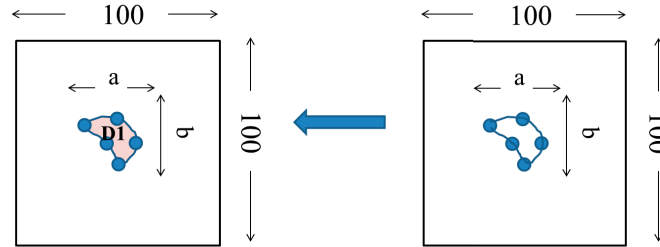


Figure 3.4 – Phantom map generation flow graph. The generation consists of four steps: define a window, select points within the window, connect the points, and assign the phantom finger.

To quantify the size of phantom sensation area (the area on the remaining stump that can elicit the feeling of lost fingers), the ‘phantom sensation coverage ( $C_{PS}$ )’ parameter is defined to describe the percentage of the phantom sensation area over the remaining stump:

$$C_{PS} = \frac{A_{\text{Phantom fingers}}}{A_{\text{Stump area}}}, \quad (3.4)$$

where  $A_{\text{Phantom fingers}}$  is the total phantom finger area, and  $A_{\text{Stump area}}$  is the whole stump area,  $A_{\text{Stump area}} = 100 \times 100$ . In our case, each cell is a sampling point.

The phantom map model generation method provides the possibility to adjust the phantom sensation coverage range (Fig. 3.5), to select between complete and partial phantom maps, and to control the total number of generated phantom digit representations (Fig. 3.6). Examples of generated phantom map models are shown in Fig. 3.7.

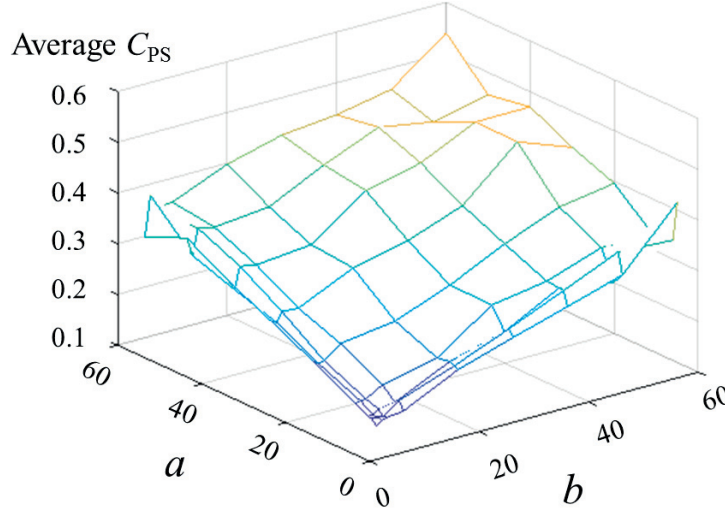


Figure 3.5 – Phantom sensation coverage control: average  $C_{PS}$  of 5 fingered phantom maps generated by varying  $a$  and  $b$  within  $0 < a, b \leq 60$ .

#### 3.2.2 Database from reported phantom map images

To further validate the proposed algorithms, we also used five reported phantom map images from the literature [175, 176, 170, 177] to build a second phantom map database. To digitize the reported phantom map images, the edge of each phantom finger in the reported phantom map images (Fig. 3.17(a)) was outlined in Illustrator (Adobe Illustrator CC, United States) and each phantom finger area is assigned a color. Then each Illustrator processed image is imported into MATLAB 2017b (The MathWorks, Inc., United States) and down-sampled into a  $100 \times 100$  matrix (Fig. 3.17(b)), with each color mapped to its corresponding grey scale value. The compressed matrix (image) is used for classification. The corresponding predicted phantom maps using OVO-SVM and  $2 \times 2$  majority pooling are presented in Fig. 3.17 (c).

The digitized phantom maps are then transformed into a group of images using rotation, scaling, shearing, translation, and barrel or pin cushion transformation. For rotation, each digitized reported phantom map image is rotated between  $0^\circ$  and  $360^\circ$  for every  $5^\circ$ . For scaling, both proportional scaling and one-dimensional scaling are used. The scaling factor ranges from 10 % and 100 %. For the translation, both single direction and bi-directional translation are used. The shear factor ranges from 0 to 1. For barrel or pin cushion transformation, the amplitude of the cubic term varies between -0.01 to 0.01. Examples of the transformed images

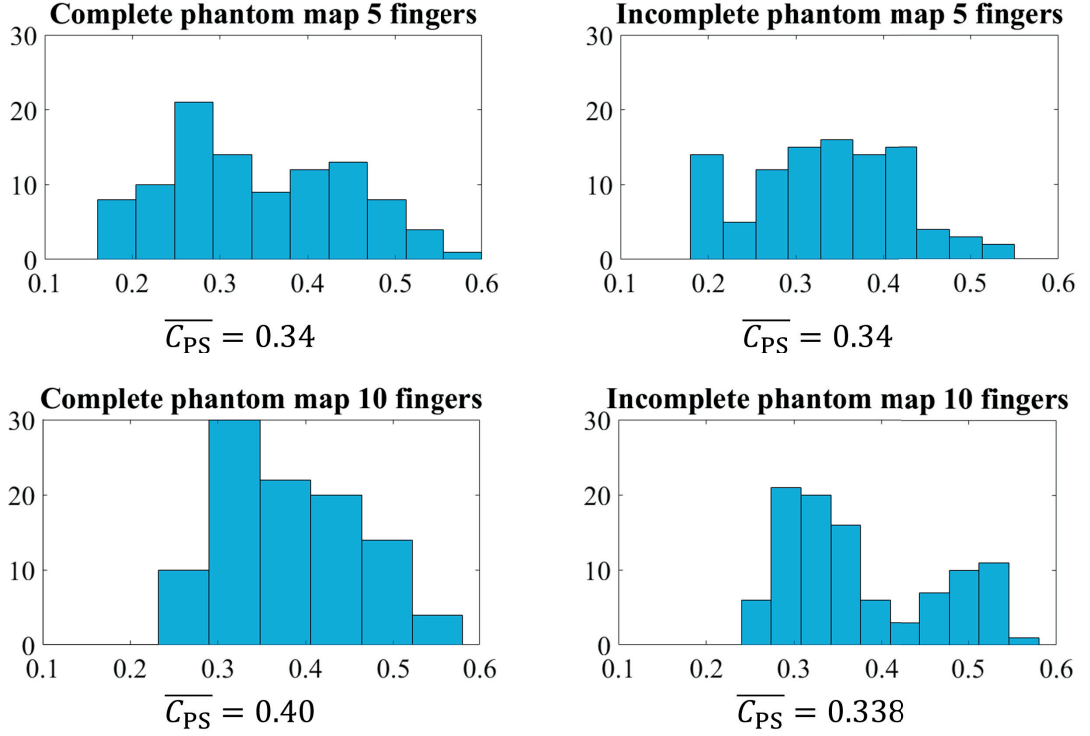


Figure 3.6 –  $C_{PS}$  distribution of 400 generated phantom maps (100 samples of each type). x-axis:  $C_{PS}$ , y-axis: number of phantom maps.

are shown in Fig. 3.8.

### 3.3 Sampling methods

Our work applies machine learning algorithms for accurate phantom map detection. One of the reasons to use machine learning algorithms is to deploy a limited number of sample points (referred to as samples in the rest of the chapter) and thus require limited active time involving an amputee. Selecting representative samples is key for machine learning algorithms. Our experience working with amputees has confirmed that amputees can clearly identify the phantom finger that is being touched and that the amputee can distinguish which finger feels stronger when several phantom fingers were simultaneously touched.

Three different sampling methods to gather training data are proposed and explained in this section (Fig. 3.2: Step 1: Sampling): random sampling, systematic sampling, and majority pooling sampling. Although their effectiveness is tested with simulated data, the sampling protocols are designed in such a way that they are also applicable in future clinical tests.

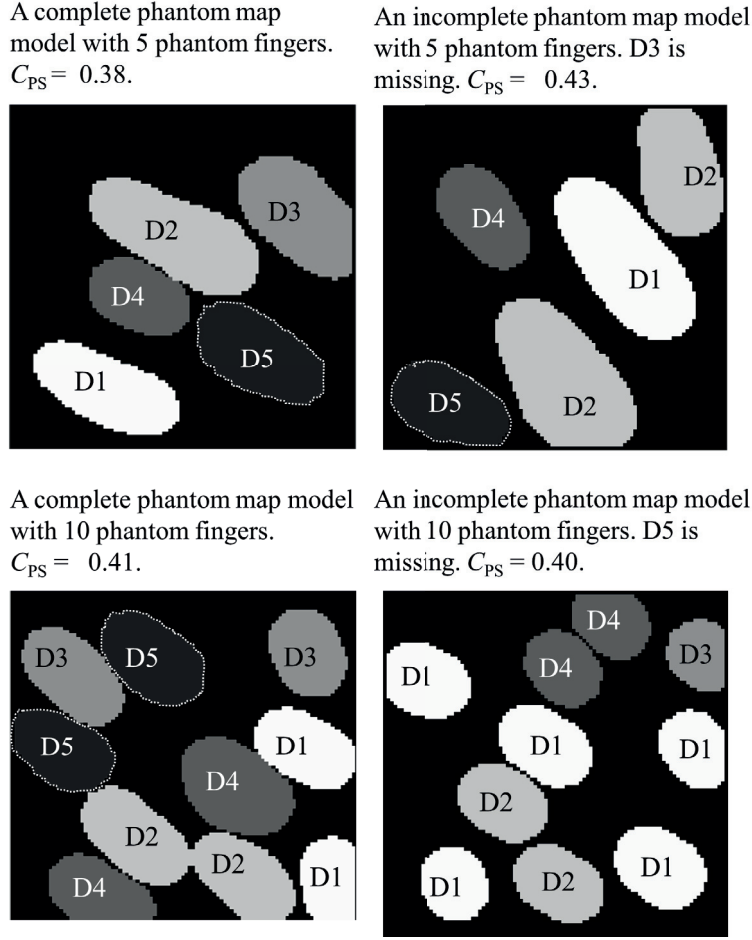


Figure 3.7 – Examples of generated phantom map models.

### 3.3.1 Random sampling (RS)

Random sampling involves randomly picking  $m$  data sets and labeling them individually (Fig. 3.9 (a)). The  $m$  data sets will be used for training the support vector machine algorithms.

### 3.3.2 Systematic sampling (SS)

Instead of randomly choosing the query data point, the whole phantom map region is evenly divided into a regular grid. Each grid point is a sampling point (Fig. 3.9 (b)).

### 3.3.3 Majority pooling sampling (MPS)

Majority-pooling sampling shares the same principle with the max-pooling concept of convolutional neural networks. Applying pooling can provide a more compact representation of the data sets and high resistance to outliers [178]. First, MPS defines a number of non-overlapping

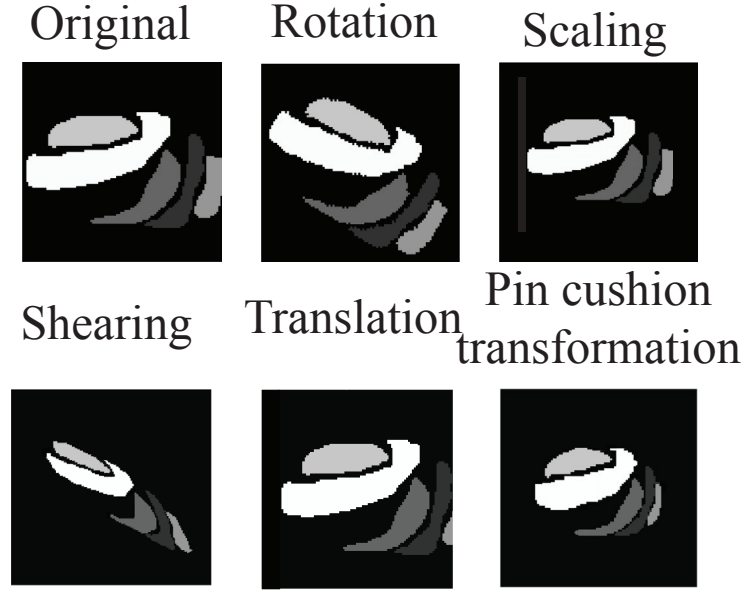


Figure 3.8 – Examples of transformed phantom map images from the reported phantom map images.

rectangular windows  $\mathbf{W}_i$ , with  $\mathbf{W}_i \subset \mathbf{A}_{\text{stump area}}$  and  $i \in [1, 2, \dots, M]$ ,  $M$  being the number of training data sets. Each window covers  $p \times q$  sampling points. The contents (finger number) of all the cells within the window are collected and relabeled as the number that occurs most frequently.

$$\forall i, \mathbf{W}_i = \text{Mo}(\mathbf{W}_i), \quad (3.5)$$

where Mo represents mode operation, which selects the value that occurs most frequently in the window.

Fig. 3.9 (c) and (d) are the graphical representations of two majority pooling sampling examples. Due to the mode operation, errors are introduced in the training data sets. To analyze how these errors influence the classification accuracy, we define a pooling induced error  $E_{\text{MP}}$  as

$$E_{\text{MP}} = \frac{N_E}{N}, \quad (3.6)$$

where  $N_E$  is the number of wrongly labeled training data due to pooling and  $N$  is the total number of training data sets.

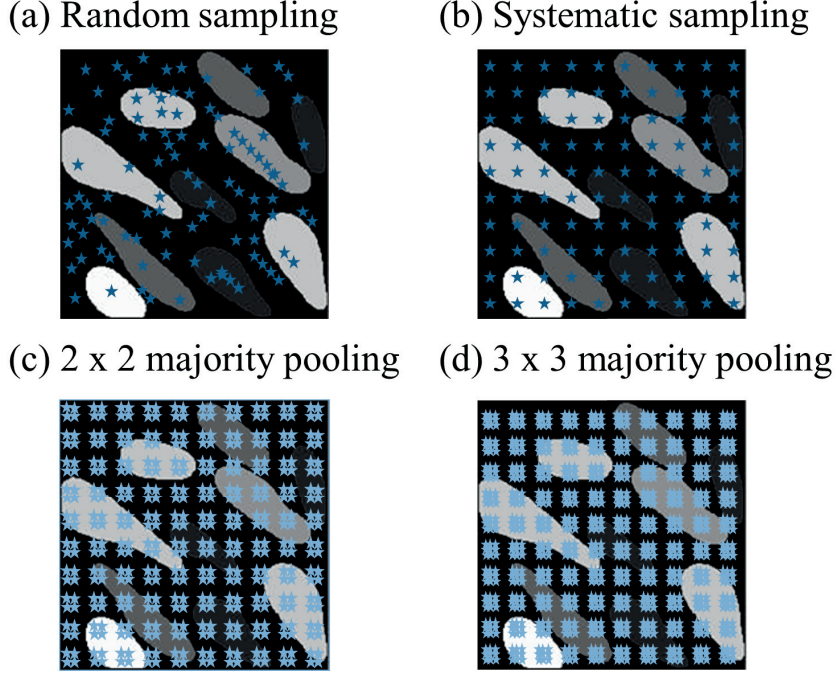


Figure 3.9 – Graphical representations of sampling methods. The number of samples is 100. The stars represent sampled points (enlarged for better visualization).

### 3.4 Support vector machines in phantom map detection

After the training data sets are gathered, the next step is to use the training data sets to train the support vector machines (SVMs) (Fig. 3.2: Step 2: training). After the SVMs are trained, they can be used to detect the phantom map distribution (Fig. 3.2: Step 3: Classification).

The working principles of SVMs have been introduced in Chapter 2 Section 2.2.2 and will not be repeated here.

The four decomposition techniques to extend binary SVMs to multi-class SVMs for phantom map detection is the same as described in Chapter2 Section 2.3. The architectures of the four decomposition techniques: one-vs-all (OVA), one-vs-one (OVO), direct acyclic graph (DAG), and binary tree (BT), are shown in Fig. 3.10 to Fig. 3.13.

Table 3.1 lists the number of binary SVMs needed for a  $k$ -class classification problem.

#### 3.4.1 Fuzzy support vector machine

Even though an SVM has high classification accuracy, it is prone to influences from noise and outliers in the training data [179]. Thus, fuzzy SVMs (FSVM) were proposed to increase the noise resistance of conventional SVMs by applying a fuzzy membership function to the training data sets [180]. The fuzzy membership function is used to reorganize the training

### 3.4. Support vector machines in phantom map detection

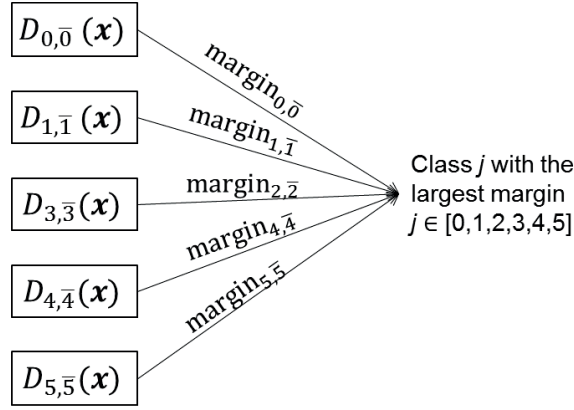


Figure 3.10 – The architecture of an OVA-SVM in classifying a complete phantom map. Zero(0) to five(5) represent no phantom sensation, thumb, index, middle, ring, and little phantom finger, respectively.  $D_{i,\bar{i}}$  represents a binary SVM (a decision function) in classifying class  $i$  and the rest of the classes.

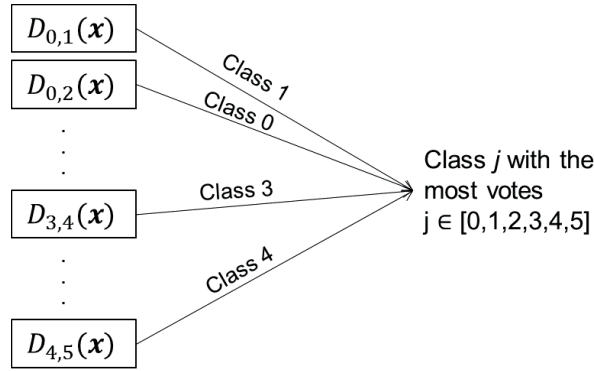


Figure 3.11 – The OVO-SVM architecture in classifying a complete phantom map. Zero to five represent no phantom sensation (0), thumb (1), index (2), middle (3), ring (4), and little phantom finger (5).  $D_{i,j}(\vec{x})$  represents a binary SVM (a decision function) in distinguishing class  $i$  and class  $j$ .

Table 3.1 – Multi-class SVM classifiers: number of binary SVMs required for the four main decomposition methods.

Method	Number of binary SVMs required for a k-class classification problem	Number of SVMs required to classify a complete phantom map
OVA	$k$	6
OVO	$\frac{k(k-1)}{2}$	15
DAG	$\frac{k(k-1)}{2}$	15
BT	$2\log_2 k$	5

data set so that the noisy or false input points contribute less to the boundary formation. In automatic phantom map detection applications, the noise mainly comes from majority

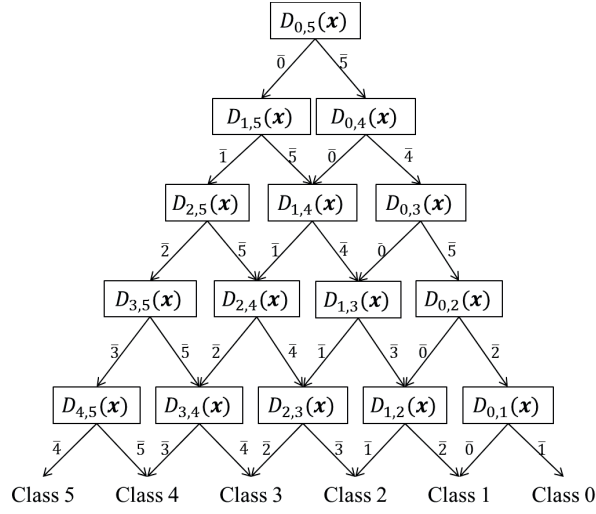


Figure 3.12 – The DAG-SVM architecture in classifying a complete phantom map. Zero to five represent no phantom sensation (0), thumb (1), index (2), middle (3), ring (4), and little phantom finger (5).  $D_{i,j}(\vec{x})$  represents a binary SVM for classifying between class  $i$  and class  $j$ .  $\bar{i}$  on the branch represents the decision function output that the testing point does not belong to any class  $i$ .

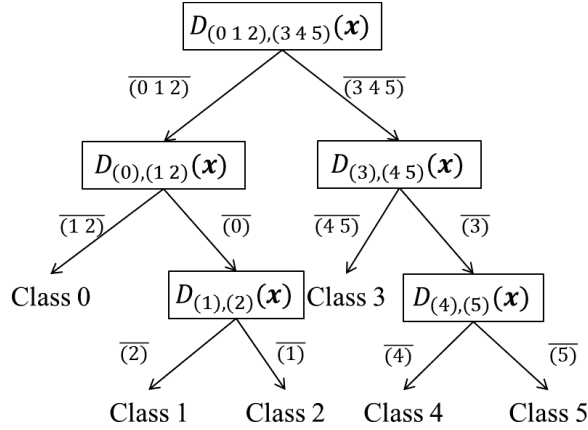


Figure 3.13 – A BT-SVM architecture for classifying a complete phantom map. Zero to five represent no phantom sensation (0), thumb (1), index (2), middle (3), ring (4), and little phantom finger (5).  $D_{(\vec{i}),(\vec{j})}(\vec{x})$  represents a binary SVM in distinguishing between classes included in  $\vec{i}$  and classes included in  $\vec{j}$ .  $\overline{(\vec{i})}$  represents the decision function output that the data does not belong to any of the classes included in  $\vec{i}$ .

pooling sampling (Subsection 3.3.3). In order to reduce the effect of pooling-induced errors, we propose to employ a step fuzzy membership function  $f_c$ :

$$f_c = \begin{cases} 1 & \text{when } \forall i \text{ and } j, i \neq j, S_i = S_j, \\ \alpha & \text{otherwise,} \end{cases} \quad (3.7)$$

### 3.4. Support vector machines in phantom map detection

where  $i$  and  $j$  are the element indices in a pooling window,  $S_i$  and  $S_j$  are the phantom sensation labels of the  $i^{th}$  and  $j^{th}$  element, with  $S_i, S_j \in [0, 1, 2, 3, 4, 5]$ , and  $\alpha$  is a constant.

After applying the fuzzy membership function, the penalty parameter  $C$  in (2.11) depends on the training data sets:

$$\mathbf{C} = C_{\text{const}} \times f_c, \quad (3.8)$$

where  $C_{\text{const}}$  is the constant penalty parameter value defined in the conventional SVM.

#### 3.4.2 Active learning support vector machine

Active learning can be considered as a semi-supervised machine learning technique [181]. It is suitable in situations where data are abundant, but the labeling is ‘expensive’ or time-consuming. In this case, selecting suitable data for each query is important. Active learning is able to query the candidate data interactively, using a specified rule (called query strategy) and sequentially adding new data for labeling and contributing to the model training. Formulating the query strategy is one of the core research topics in active learning. One of the most widely-used query strategies is uncertainty sampling [182]. Among the uncertainty sampling methods, margin sampling (MS) and its variations, especially multi-class level uncertainty (MCLU), have shown good performance when combined with SVM [182].

The MS strategy queries the instances with the least confidence under the current model:

$$x_M^* = \operatorname{argmax}_x (1 - P_D(\hat{y}|x)), \quad (3.9)$$

where  $x_M^*$  is the instance selected for query,  $\hat{y}$  is the class label under the current model  $D$ ,  $P_D$  represents the distance to the decision boundaries, and  $x$  represents the feature of the candidate set.

The MCLU approach selects the samples that feature the smallest difference between the first and the second largest distance values to the decision hyperplanes. In other words, MCLU focuses on the instances that have the most uncertainty between the two most likely classes in the current model:

$$x_M^* = \operatorname{argmin}_x (P_D(\hat{y}_1|x) - P_D(\hat{y}_2|x)), \quad (3.10)$$

where  $x_M^*$  is the instance selected for query,  $\hat{y}_1$  and  $\hat{y}_2$  are the two most likely class labels under the current model  $D$ ,  $P_D$  represents the distance to the decision boundaries,  $x$  represents the feature of the candidate set.

The above mentioned two strategies focuses on adding one instance at a time. In order to achieve faster training, batch-mode active learning is often used, whereby a group of instances

is added at a time. To ensure the representativeness of selected instances, diversity criteria are often used for query data selection. In the current study, we applied angle-based diversity (ABD), as it shows improved classification accuracy when combined with SVM [183, 184]. The diversity is measured by the cosine angle distance between two samples defined in the kernel space:

$$\angle(x_i, x_j) = \cos^{-1}\left(\frac{K(x_i, x_j)}{\sqrt{K(x_i, x_i)K(x_j, x_j)}}\right), \quad (3.11)$$

where  $K(\cdot)$  is the kernel function (the RBF kernel defined in Chapter 2 (2.12) in our case),  $x_i$  and  $x_j$  are the features of two instances of selected for the similarity measurement.

The diversity criteria variable  $g$  can therefore be expressed as:

$$g = \max\left\{\frac{|K(x_{i,l}, x_{i,j})|}{\sqrt{K(x_{i,l}, x_{i,l})K(x_{i,j}, x_{i,j})}}\right\}, \quad (3.12)$$

To combine both batch-mode uncertainty measurement and diversity criteria, the added training batch is constructed incrementally:

$$x_t = \arg \min_{x_i \in I/X} \left( \lambda |f(x_i)| + (1 - \lambda) \left[ \max_{x_j \in X} \frac{K(x_i, x_j)}{\sqrt{K(x_i, x_i)K(x_j, x_j)}} \right] \right), \quad (3.13)$$

where  $I$  contains the unlabeled candidate data in the pool,  $I/X$  represents the candidate data excluding the ones already contained in the current batch,  $f(x_i)$  is the distance to the hyperplane, and  $\lambda$  is the trade-off parameter between uncertainty measurement and diversity criteria.

## 3.5 Results and discussion

Due to the absence of wearable dense stimulation arrays, the automatic phantom map detection algorithms were tested on realistic and flexible generated phantom maps as well as five reported phantom map images and transformations thereof. The phantom map generation algorithm considered different types of phantom maps and introduced parameters to provide a variety of reasonable and representative shapes. The trends of the classification results obtained by the two types of phantom maps are similar. Therefore, the analyses and discussion were applicable for both generated and reported phantom maps.

The phantom map model generation and detection were implemented in MATLAB 2017 (The MathWorks, Inc., United States), running on an HP laptop with an Intel core i5-4300 CPU@1.90 GHz. Six types of metrics are defined below, and used to interpret the classification accuracy (presented in Subsection 3.5.2). The timing of each algorithm is presented and examined in Subsection 3.5.3. The impacts of different algorithms, sampling methods, stimulation array density, and socket shifting on accuracy and timing are discussed, respectively.

### 3.5.1 Simulation setup

Two types of scenarios were simulated: dense array and coarse array.

**Dense array** A total of 100 samples for the sampling phase were selected, which we believe to be realistic for a dense array. From our experience of working with amputees, we have observed that the approximate time needed for one stimulating and collecting response is 15 to 30 seconds. In a clinical set-up, we need 25 to 30 minutes to complete 100 data collections, which is a reasonable time period to actively involve an amputee.

**Coarse array** The potential use of custom-designed coarse stimulation arrays for phantom map detection is also investigated. These stimulation arrays are designed primarily to provide sensory feedback for upper limb amputees (Chapter 3). Two types of stimulation devices are considered: a multi-modal actuator combining a servo motor and an eccentric rotating mass vibrator (Fig. 3.14(a)) and a servo motor-based mechanotactile pusher (Fig. 3.14(b)). For the multi-modal stimulation device, the minimal contact size is fixed by the vibrator ( $153 \text{ mm}^2$ ). For the mechanotactile pusher, the arm and pin are 3D printed and the contact size is controllable. A  $3 \times 5$  multi-modal actuator array (Fig. 3.14(c)) [185] or a  $4 \times 6$  mechanotactile actuator array can fit on the remaining stump of an amputee.

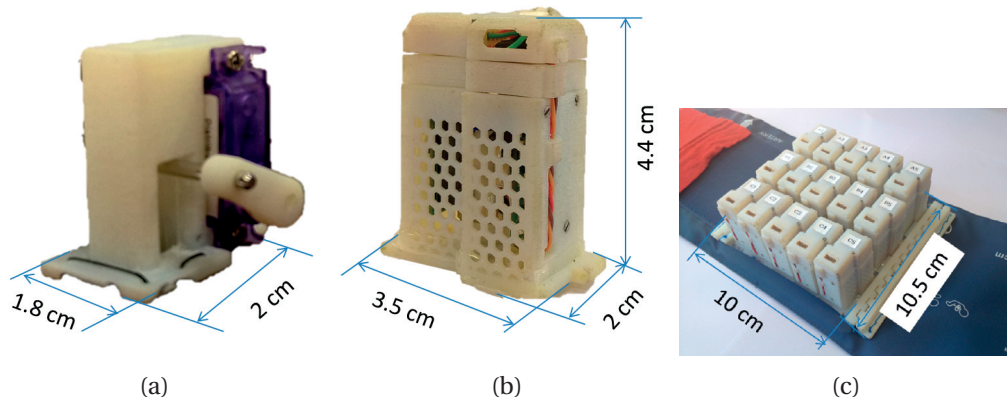


Figure 3.14 – Two types of stimulation devices: (a) mechanotactile stimulation device and (b) multi-modal stimulation device, principally used for providing sensory feedback for upper limb amputees. An array consisting of  $3 \times 5$  multi-modal stimulation devices are also shown (c).

The physical contact sizes of mechanotactile and multi-modal actuators are represented by pooling sizes in the simulation scenario. The average phantom map area is roughly  $100 \text{ cm}^2$ . The minimum contact sizes for mechanotactile and multi-modal actuators are  $100 \text{ mm}^2$  and  $153 \text{ mm}^2$ , respectively. Given that in a simulation scenario the pooling size reflects the physical contact size, the corresponding minimum pooling sizes  $p \times q$  (defined in 3.3.3) are  $15 \times 9$  and  $7 \times 7$  for multi-modal and mechanotactile actuators, respectively (Fig. 3.15).

The overall simulation setup is summarized in Table 3.2

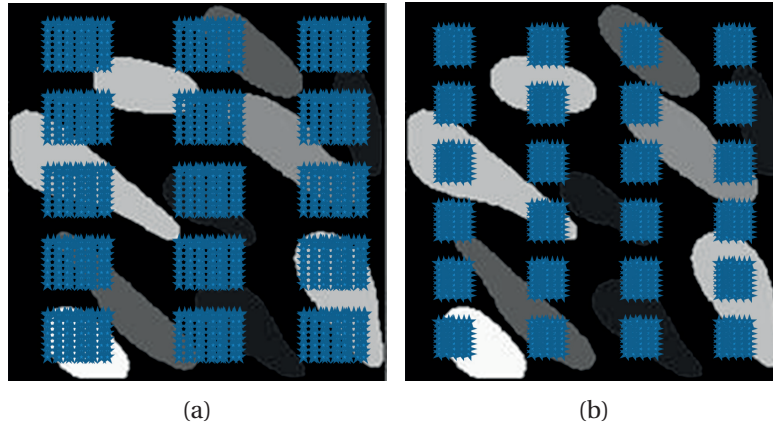


Figure 3.15 – Graphical representations of coarse array sampling. The blue stars represent sampling points, enlarged for better visualization. (a) Multi-modal stimulation array:  $3 \times 5$  sampling size with  $15 \times 9$  pooling size. (b) Mechanotactile stimulation array:  $4 \times 6$  sampling size with  $7 \times 7$  pooling size.

Table 3.2 – Simulation setup using dense ( $100 \times 100$ ) and coarse arrays (multi-modal and mechanotactile) for different sampling methods.

	Sampling methods	
	RS and SS	MPS (pooling size = $p \times q$ )
# Training data sets per phantom map model	100	$100 \times p \times q$
# Testing data sets per phantom map model	10000	
Number of phantom maps in each database		
Phantom map database	Type	Number of phantom map images
# Generated phantom maps	complete 5	100
	complete 10	100
	incomplete 5	100
	incomplete 10	100
# Transformed reported phantom map images	reported (original)	5
	rotation	$72 \times 5$
	scaling	$10 \times 5$
	shearing	$20 \times 5$
	translation	$10 \times 5$
	barrel or pin cushion	$20 \times 5$

### 3.5.2 Accuracy

The detection accuracies of different sampling methods, algorithms, and scenarios are depicted by six metrics defined in the following.

### Accuracy metrics definition

To evaluate the accuracy of the phantom map detection algorithms, six types of metrics are defined: absolute error rate ( $E_A$ ), functional error rate ( $E_F$ ), redundancy error rate ( $E_R$ ), insufficiency error rate ( $E_I$ ), precision error rate ( $E_P$ ), and phantom sensation coverage ratio ( $R_{PSC}$ ) between a generated phantom map and its corresponding predicted phantom map.

The general error rate  $E$  is defined as

$$E = \frac{\sum_{i=1}^N f_i(c_{i,a}, c_{i,p})}{N}, \quad (3.14)$$

$$\text{where } f_i(c_{i,a}, c_{i,p}) = \begin{cases} 1 & \text{when } c_{i,a} \neq c_{i,p} \\ 0 & \text{when } c_{i,a} = c_{i,p} \end{cases}$$

$c_{i,a}$  is the real label of the  $i^{\text{th}}$  testing set,  $c_{i,p}$  is the predicted label of the  $i^{\text{th}}$  testing set, and  $N$  is the number of testing data sets for  $E_A$ ,  $E_F$ ,  $E_R$ , and  $E_I$ , and the number of testing data sets containing phantom sensation for  $E_P$ .

- For  $E_A$ ,  $c_{i,a} \in \{0, 1, 2, 3, 4, 5\}$ ,  $c_{i,p} \in \{0, 1, 2, 3, 4, 5\}$ .  $E_A$  measures the fraction of all misclassified data points of a predicted phantom map.
- For  $E_F$ ,  $c_{i,a} \in \{1, 2, 3, 4, 5\}$ ,  $c_{i,p} \in \{1, 2, 3, 4, 5\}$ .  $E_F$  measures the fraction of points belonging to one phantom finger which are falsely attributed to another finger, leading to a functional error (wrong finger stimulation when providing sensory feedback).
- For  $E_R$ ,  $c_{i,a} = 0$ ,  $c_{i,p} \in \{1, 2, 3, 4, 5\}$ .  $E_R$  measures the fraction of points belonging to class 0 (i.e. no phantom sensation) which are wrongly attributed to other classes. When providing sensory feedback, these points do not cause mistakes between fingers, but their stimulation is redundant and costs energy without providing useful feedback.
- For  $E_I$ ,  $c_{i,a} \in \{1, 2, 3, 4, 5\}$ ,  $c_{i,p} = 0$ .  $E_I$  measures the loss of stimulation points which takes place when data points belonging to class 1 to 5 (phantom thumb to phantom little finger) are wrongly attributed to class 0 (no phantom sensation) and therefore not stimulated.
- For  $E_P$ ,  $c_{i,a} \in \{1, 2, 3, 4, 5\}$ ,  $c_{i,p} \in \{1, 2, 3, 4, 5\}$ .  $E_P$  indicates the fraction of incorrectly classified phantom sensation points with respect to all the phantom sensation points in the generated phantom map.

The absolute error rate is the sum of functional, redundancy, and insufficiency error rates:

$$E_A = E_F + E_R + E_I. \quad (3.15)$$

$E_P$  is a special case of misclassification between fingers. It is defined as :

$$E_P = \frac{E_F}{C_{PS}}. \quad (3.16)$$

The phantom sensation coverage ratio  $R_{PSC}$  is the ratio of predicted phantom sensation area over the original phantom sensation area:

$$R_{PSC} = \frac{C'_{PS}}{C_{PS}}, \quad (3.17)$$

where  $C'_{PS}$  is the phantom sensation coverage of the predicted phantom map and  $C_{PS}$  is the phantom sensation coverage of the original generated phantom map.  $R_{PSC}$  defines the proportion of the predicted phantom map  $C'_{PS}$  over the corresponding generated phantom map model (the original  $C_{PS}$ ) (3.17).

To demonstrate the defined metrics, Fig. 3.16 shows examples of generated phantom maps, predicted phantom maps, their confusion matrices and accuracy metrics.

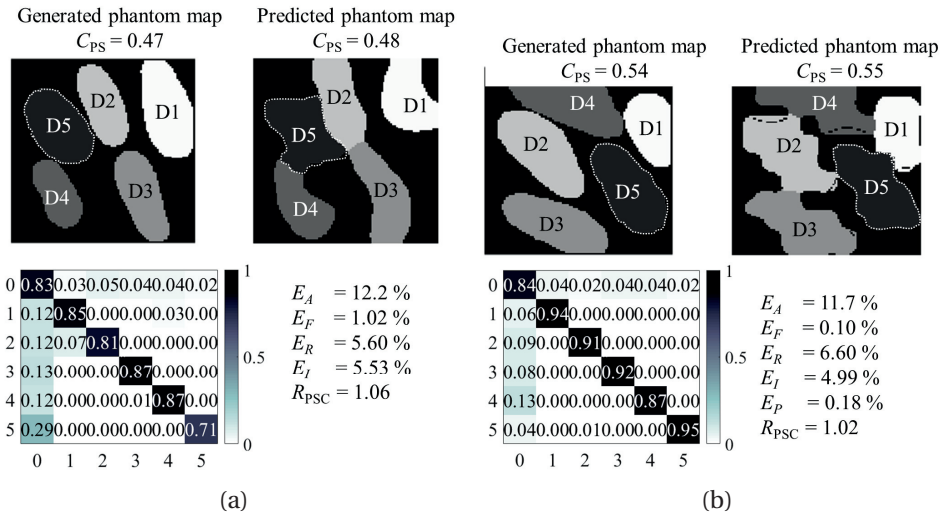


Figure 3.16 – Examples of generated phantom maps, predicted phantom maps, their confusion matrices, absolute error rates ( $E_A$ ), functional error rates ( $E_F$ ), redundancy error rates ( $E_R$ ), insufficiency error rates ( $E_I$ ), and precision error rates ( $E_P$ ) using (a) BT-SVM with 3 × 3 majority pooling and (b) OVA-SVM with 3 × 3 majority pooling.

#### Grand average accuracy

The grand average accuracy is defined as the average error rate over all 400 generated phantom maps (Fig. 3.6) or over the tested phantom map photos. The five types of grand average error rates and phantom sensation coverage ratios of different SVM algorithm and sampling method combinations are presented in Fig. 3.18. The reported error rates for active learning

(AL) is the smallest error rate from different query strategies, diversity criteria, initial size, and incrementing steps.

For the reported phantom map images, the edge of each phantom finger in the phantom map photos presented in the literature (Fig. 3.17(a)) was outlined in Illustrator (Adobe Illustrator CC, United States). Each phantom finger area is assigned a color. Then the outlined image is imported into MATLAB 2017b (The MathWorks, Inc., United States) and down-sampled into a  $100 \times 100$  matrix (Fig. 3.17(b)). Each color is mapped to its corresponding grey scale value. The compressed matrix (image) is used for classification. Selected classification results are presented in Fig. 3.17 (c) and (d).

The detection accuracy results obtained by using the reported phantom map images show similar trends to those observed when using generated phantom maps; the following analysis does therefore apply to both types, although it will be mostly focused on the discussion of the generated data. The error rates of the reported phantom maps are slightly higher than those of the generated ones, which could be caused by the low average phantom sensation coverage of the former. However, it is hard to draw further conclusions because of the limited sample size.

#### The influence of sampling methods

To further discuss the influence of sampling methods, Fig. 3.19 is presented, illustrating the absolute classification error rate as a function of different sampling methods. The algorithm used is OVO-SVM, over 100 complete phantom maps with 5 phantom fingers.

For all four algorithms used, applying majority pooling generally reduces error rates, especially the absolute error rate  $E_A$  and the functional error rate  $E_F$  (Fig. 3.18). Random and systematic sampling produce higher rates because the two sampling methods cannot acquire enough representative data points (as qualitatively illustrated in Fig. 3.9). Only 1 % of the total data points are considered in the training while using random or systematic sampling. By applying majority pooling, a larger range of samples can be acquired, normally  $p \times q$  more data compared to the other two sampling methods, with a sample size of  $p \times q$ .

It was also observed that for the chosen dense array settings (Table 3.2),  $2 \times 2$  majority pooling produces the smallest error rates for all five error rate metrics (see for example Fig. 3.19 for  $E_A$ ). However, when using majority pooling in other settings, there is a trade-off between the pooling-induced error rate and the sampling range. A larger pooling size can produce a larger sampling range coverage, but it introduces more pooling-induced errors or noise. For each particular setting, an optimal pooling size exists.

#### The influence of different SVM decomposition methods

Overall, the OVO architecture produces the lowest  $E_A$  (Fig. 3.18) and we have observed that the predicted phantom map shapes do indeed best represent the original phantom maps (Fig.

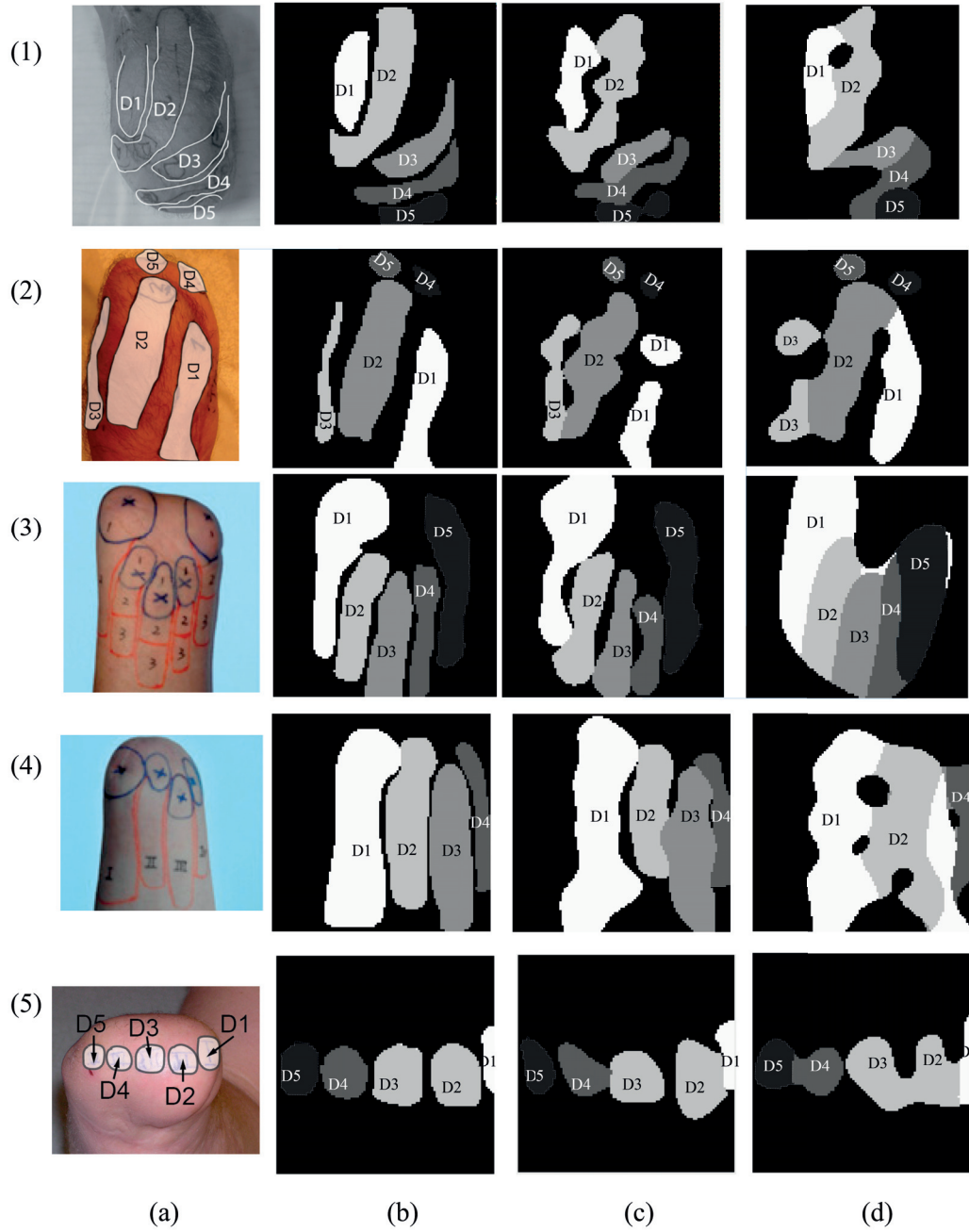


Figure 3.17 – Examples of (a) the photos of phantom maps drawn on the remaining stumps ((1)[170], (2)[177], (3) [176], (4)[176], (5)[177]), (b) the down-sampled phantom map matrices based on the photos, (c) the predicted phantom maps using OVO-SVM with majority pooling (pooling size =  $2 \times 2$ , and (d) the predicted phantom maps using BT-SVM with majority pooling (pooling size =  $2 \times 2$ ). The phantom maps predicted using OVO-SVMs better represent the original shapes of the phantom fingers than the ones using BT-SVMs. Due to the architecture of BT-SVM, the phantom fingers tend to become attached to each other.

3.16). Although OVA has the second best performance. We have observed unclassified regions when using this architecture. Examples of the unclassified region can be seen in the dashed black lines running within a phantom map finger in Fig. 3.16(b).

The architecture of BT-SVM is intrinsically different from the other three multi-class SVMs. All the other three methods classify, to some degree, one class at a time, whereas a BT-SVM tries to separate a group of classes from another group of classes. When classifying a complete phantom map (Fig. 3.13), the BT-SVM first distinguishes between class group (0, 1, 2) and class group (3, 4, 5). When then distinguishing between classes (3, 4, 5), it does not consider the classes (0, 1, 2), but only looks for the largest margin between the classes (3, 4, 5) themselves. This can result in two of the class regions being connected in the predicted phantom map, such as in Fig. 3.16(a).

When using BT-SVM, different tree structures can produce different prediction results, especially when dealing with unbalanced data sets. BT-SVM should theoretically have a faster training and classification speed - however, the fast speed comes with the price of a degraded performance[156].

#### The effect of adding a fuzzy membership function

Fuzzy SVMs are applied to each decomposition SVM algorithm. An FSVM assigns a fuzzy membership function (3.7) to each training data set, so that each training data set makes a different contribution in the training process. An FSVM can reduce the influence of pooling induced errors  $\overline{E_{MP}}$  (3.6). Using FSVMs generally increases the detection accuracy when using the  $100 \times 100$  dense arrays. We have also observed that FSVMs reduce the unclassified region for OVA- and OVO-SVM, in accordance with findings in previous literature [186, 187].

#### The influence of active learning

As mentioned in Subsection 3.4.2, there are different query strategies and diversity criteria for active learnings. Moreover, the initial size and batch size also affect the final accuracy. The error rates using different query strategies, diversity criteria, initial sizes, and batch sizes are listed in Table 3.3 and examples of learning curves when using margin sampling are shown in Fig. 3.20.

For MS query strategies, smaller batch sizes generally produce smaller final error rates (Fig. 3.20). For MCLU query strategies, the influence of batch sizes on final error rate are less dominant. In our specific classification application, adding ABD diverse criteria does not necessarily decrease the error rate (Table 3.3).

### Chapter 3. Automatic Hand Phantom Map Generation and Detection

Table 3.3 – Absolute error rates of active learning SVMs using different query strategies, diversity criteria, initial and batch sizes. The algorithm used is OVA-SVM with  $2 \times 2$  majority-pooling sampling. For ABD, the trade-off parameter  $\lambda = 0.5$ .

Initial size	Batch size	Query strategy and diversity criteria			
		MS	MCLU	MS + ABD	MCLU + ABD
40	2	11.62	16.8	15.5	20.4
	5	18.3	16.0	17.6	19.5
	10	19.7	15.7	20.0	18.7
	20	21.3	15.8	21.1	17.5
50	2	11.6	15.4	11.7	16.4
	5	9.11	15.4	10.5	14.5
	10	15.5	16.1	14.6	13.3
	20	16.0	12.9	15.7	11.5
60	2	12.1	14.7	11.9	13.6
	5	20.6	13.9	19.8	15.1
	10	16.4	13.3	18.4	17.4
	20	17.5	13.9	18.0	16.9
70	2	11.4	11.6	12.5	12.3
	5	14.4	12.8	13.4	10.7
	10	17.6	12.3	16.8	10.4
	20	19.3	11.8	19.4	12.5
80	2	18.8	11.6	17.5	12.0
	5	19.7	9.59	18.7	10.4
	10	19.6	9.46	18.7	11.3
	20	19.3	9.66	20.4	15.4
90	2	15.0	10.4	14.5	20.2
	5	16.4	14.6	15.8	18.4
	10	16.2	15.1	17.4	19.5
	20	18.5	14.43	19.0	17.1

MS stands for margin sampling. MCLU stands for multi-class level uncertainty. ABD stands for angle-based diversity.

#### Coarse array detection accuracy

The grand average error rates and phantom sensation coverage ratios when using coarse arrays for phantom map detection are shown in Table 3.4. Fuzzy SVMs were also evaluated in coarse array detection scenarios. However, the error rates were not significantly decreased when fuzzy membership functions were used, thus the corresponding results are not reported here. Fig. 3.21 shows examples of generated phantom maps, their corresponding predicted phantom maps, the confusion matrices, and six metrics.

The detection accuracy decreases dramatically when coarse stimulation arrays are used (Fig. 3.18 VS. Table 3.4). For coarse arrays, OVO architecture was still shown to produce the smallest error rate. However, applying fuzzy SVM does not decrease the error rates. One possible

Table 3.4 – Grand average accuracy results over all 400 generated phantom maps using coarse stimulation arrays (Fig. 3.14).

Multi-modal stimulation array $3 \times 5$ , pooling size: $15 \times 9$ , $\overline{E_{MP}} = 14.9\%$						
Method	$\overline{E_A}(\%)$	$\overline{E_F}(\%)$	$\overline{E_R}(\%)$	$\overline{E_I}(\%)$	$\overline{E_P}(\%)$	$\overline{R_{PSC}}$
OVA	35.9	7.06	11.6	17.2	22.5	1.08
OVO	32.1	2.20	13.7	16.2	13.6	0.91
DAG	38.5	5.4	15.6	17.5	20.7	0.86
BT	51.8	4.6	23.6	13.6	38.2	1.23
Mechanotactile stimulation array $4 \times 6$ , pooling size: $7 \times 7$ , $\overline{E_{MP}} = 19.4\%$						
OVA	33.5	3.80	25.0	4.77	9.41	1.57
OVO	33.2	2.19	26.9	4.14	5.51	1.66
DAG	37.5	5.95	15.2	16.4	7.83	1.25
BT	40.8	9.48	27.2	4.17	30.2	1.38

explanation is that the pooling size is too big and the sensing density is too small, thus the high pooling induced error is so large that the current fuzzy membership cannot cancel the error rate.

From the simulation results of coarse array detection, we could conclude that a dense array is needed for accurate phantom map detection. However, to the best of our knowledge, no wearable dense array ( $100 \times 100$ ) is readily available. Therefore, we propose a two-step approach for sensory feedback designs: first, a non-wearable dense array is used to detect the accurate phantom map shapes. Then, according to the predicted phantom map distribution, a wearable array consisting of 20 to 30 actuators can be integrated into the socket.

### Socket shifting effects

For the dense array scenario, the stimulation devices are used both for phantom map detection and for providing sensory feedback. The stimulation devices are embedded in the socket. The socket is taken on and off daily, thus resulting in slight shifts of the stimulation device arrangement. One possible shifting scenario could be the lateral shift shown in Fig. 3.22. This scenario has been simulated with different levels of shifting and the error rates are calculated as shown in Fig. 3.23 and Fig. 3.24.

As can be seen from Fig. 3.23, all the error rates increase as the shifting degree increases (Fig. 3.24). Despite the dramatic increase of the absolute error rate  $E_A$ , the functional error rate  $E_F$  does not increase substantially in absolute terms (from 0.12 % to 0.97 %). Indeed, the increased  $E_F$  is still small (less than 1 %), which demonstrates that the function of the stimulation devices, reflected by the  $E_F$  value, will be not largely affected by a slight socket misalignment.

### 3.5.3 Timing

Different sampling and training methods result in different training ( $T_t$ ) and classification times ( $T_c$ ). Table 3.5 shows the grand average training and classification time using different sampling methods, averaged over all 400 generated phantom maps and calculated for the target ideal dense array as well as for the two examples of coarse stimulation arrays currently under investigation to provide sensory feedback.

Table 3.5 – Grand average training time  $\overline{T}_t$  and classification time  $\overline{T}_c$  of all 400 generated phantom maps using a dense array (100 samples) and two coarse (stimulation) arrays ( $3 \times 5$  and  $4 \times 6$  actuators, corresponding to simulation pooling sizes of  $15 \times 9$  and  $7 \times 7$ ).

	$\overline{T}_t$ (ms)	$\overline{T}_c$ (s)	$\overline{T}_t$ (ms)	$\overline{T}_c$ (s)
Dense array				
Method	OVA		OVO	
RS	35.0	15.9	54.9	33.7
SS	28.6	15.3	47.9	32.7
MP ( $2 \times 2$ )	84.2	17.5	79.3	39.6
	DAG		BT	
RS	54.9	15.8	24.8	5.57
SS	47.9	15.5	19.8	5.30
MP ( $2 \times 2$ )	79.3	16.5	48.1	6.05
Multi-modal coarse (stimulation) array, $3 \times 5$ actuators				
	OVA		OVO	
MP $15 \times 9$	952	34.7	356	46.7
	DAG		BT	
MP $15 \times 9$	356	35.8	301.9	9.13
Mechanotactile coarse (stimulation) array, $4 \times 6$ actuators				
	OVA		OVO	
MP $7 \times 7$	348.3	25.2	196	45.0
	DAG		BT	
MP $7 \times 7$	196	43.5	153	9.79

The training and classification time increase substantially with the pooling size, but still stay within an acceptable range. Given the same number of training data sets, the training and classification times were influenced by decomposition architectures (shown in Fig. 3.10 to Fig. 3.13). OVO and DAG share the same training process. Under the same conditions, the training times of OVO and DAG are therefore equal. Given the same number of training data sets, OVO and DAG-SVM do not require significantly more training time than the other two methods when using random and systematic sampling, and sometimes even less training time when using majority pooling sampling. The classification processes of OVO and DAG-SVM are different (Fig. 3.11 and Fig. 3.12). DAG-SVM requires much less classification time than OVO-SVM at the price of a slightly higher absolute error rate ( $E_A$ ).

### 3.6 Conclusion

This chapter proposed automatic phantom map detection algorithms using different decomposition SVMs. Fuzzy SVMs and active learning SVMs are also evaluated. In the absence of wearable dense stimulation arrays, the accuracy and timing aspects were tested on flexible and realistic phantom map models and five reported phantom map images. The results were compared and discussed. Because the classification results of five reported phantom map images are similar to that of generated phantom map models, the discussion incorporated both generated and reported phantom map images.

OVO-SVMs generally feature high classification accuracy (absolute error rate ranging between 8.8 % to 25 %) and near real time training speed (less than 1 s training time). Moreover, fuzzy-SVMs proved effective in decreasing the influence of noisy data and increasing detection accuracy, as well as reducing unclassified regions for OVA-SVMs. Active SVMs interactively select samples, thus increasing the detection accuracy when the initial size and batch size are selected properly.

The three sampling methods: random sampling, systematic sampling, and majority-pooling sampling were designed so as to be also applicable for future clinical tests. Among the three, majority-pooling sampling with a proper pooling size proved to be the most efficient, at the cost of an increase in training time which does, however, stay within an acceptable range.

The potential performance using coarse stimulation arrays, designed primarily to provide sensory feedback, was also evaluated and found to be much lower than that of a dense array. They are thus unsuitable for refined phantom map shape detection. We therefore propose a two-step approach, firstly using a non-wearable dense array to detect an accurate phantom map shape, then applying a wearable coarse stimulation array, customized according to the detection results.

To the best of our knowledge, it is the first attempt at systematic phantom map shape detection. The proposed method can help optimize sensory feedback array arrangements, as well as tracking the changes of the phantom maps.

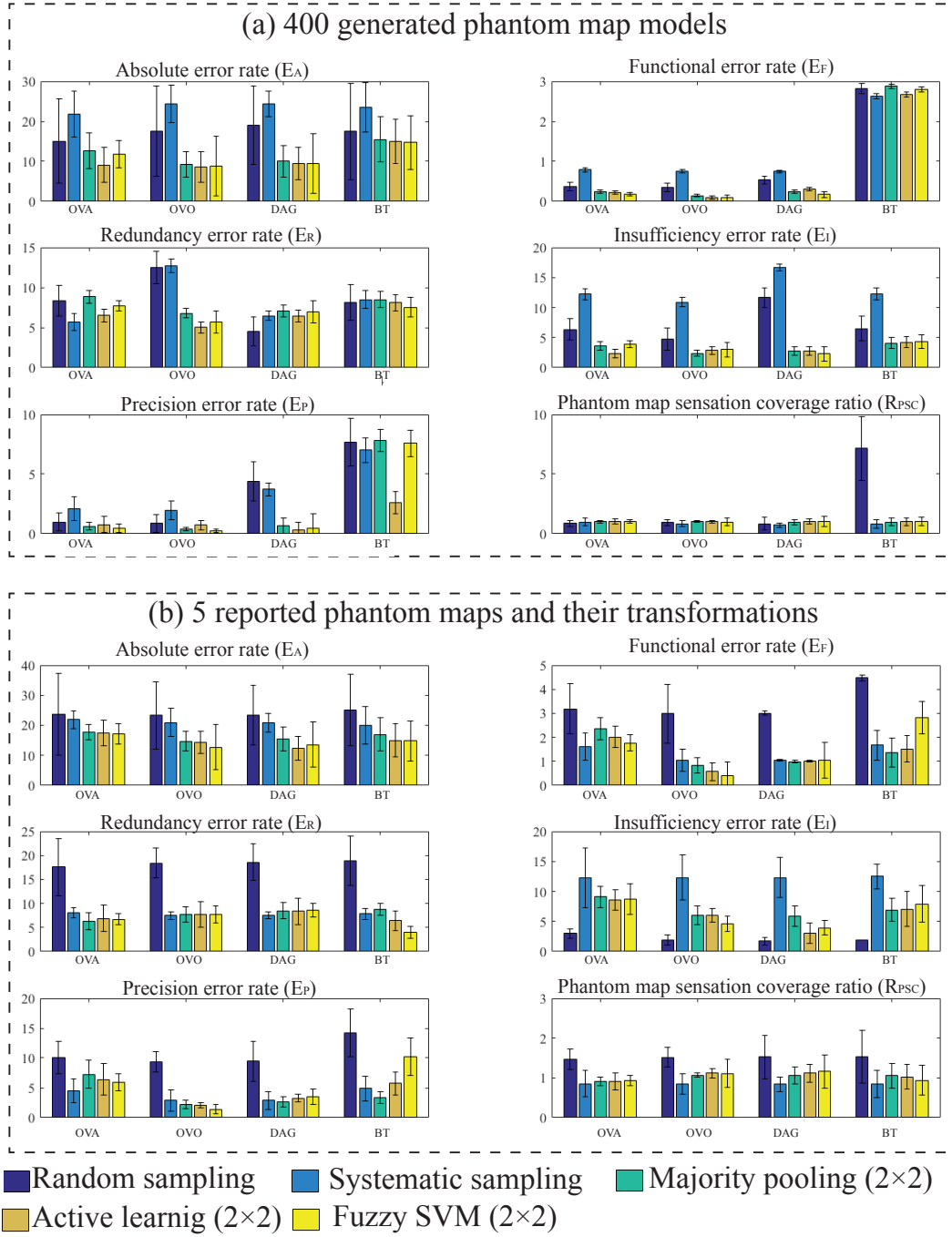


Figure 3.18 – Grand average error rates and phantom sensation coverage ratios over (a) all 400 generated phantom maps and (b) five reported phantom map images and their corresponding transformed images. For  $2 \times 2$  majority pooling,  $\overline{E}_{MP} = 5.35\%$  for generated phantom maps and  $\overline{E}_{MP} = 4.27\%$  for reported phantom map images. The grand average accuracy is influenced both by the sampling methods and SVM algorithms used. For both generated and reported phantom maps, OVO-SVM produces the smallest error rate. Even though the absolute error rate ( $E_A$ ) for reported phantom maps is higher than for the generated ones, the more critical metric (function error rate  $E_F$ ) is still within an acceptable range.

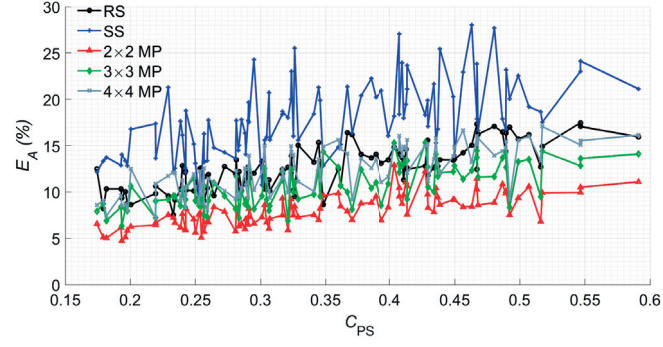


Figure 3.19 – Absolute error rate  $E_A$  vs.  $C_{PS}$  using different sampling methods for OVO-SVM. The phantom map models used are 100 complete phantom maps with 5 fingers.

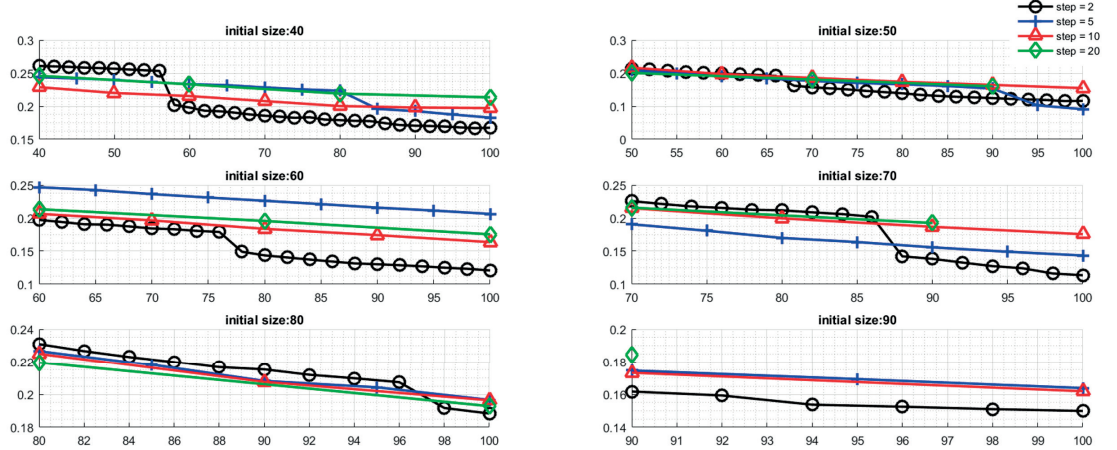


Figure 3.20 – Learning curves for different batch sizes and different initial sizes using MS selection strategies. The x-axis is the size of training data sets. The y-axis is the absolute error rate. The absolute error rate was averaged over 400 phantom maps. The used algorithm is OVA-SVM with random sampling. The stop criterion is when the number of sampling times reaches 100.

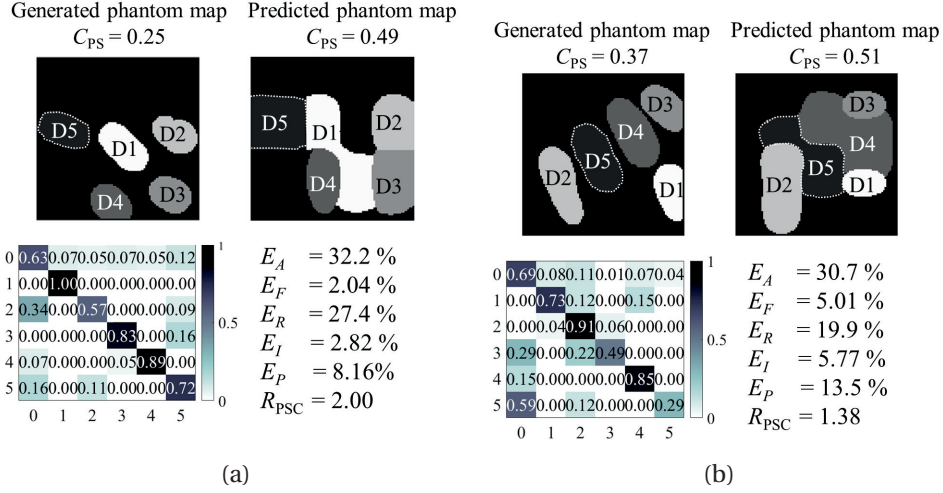


Figure 3.21 – Examples of using coarse stimulation arrays to detect phantom map distributions. The array types used and algorithms are (a) OVO-SVM, 3 × 5 multi-modal coarse array (corresponding to 15 × 9 majority pooling), and (b) BT-SVM, 4 × 6 mechanotactile coarse array (corresponding to 7 × 7 majority pooling).

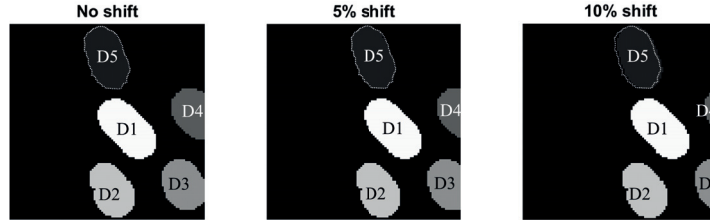


Figure 3.22 – Examples of shifting error caused by a lateral socket shift.

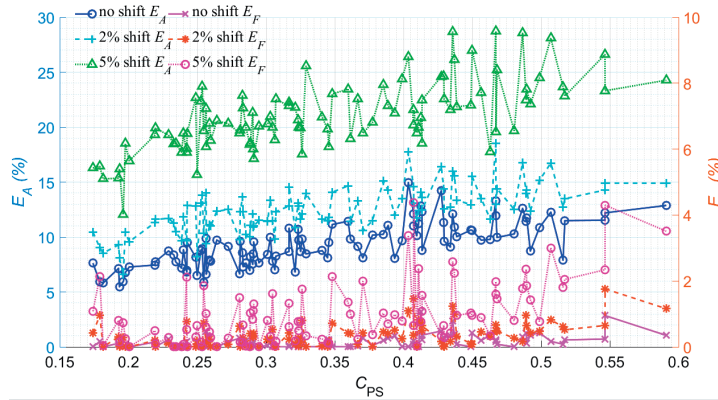


Figure 3.23 – Absolute error rate  $E_A$  and functional error rate  $E_F$  vs. phantom sensation coverage  $C_{PS}$  caused by different degrees of shifting. The phantom map models used are 100 complete phantom maps with five fingers (Fig. 3.6(a)). The algorithm used was OVO-SVM with 2 × 2 majority pooling.

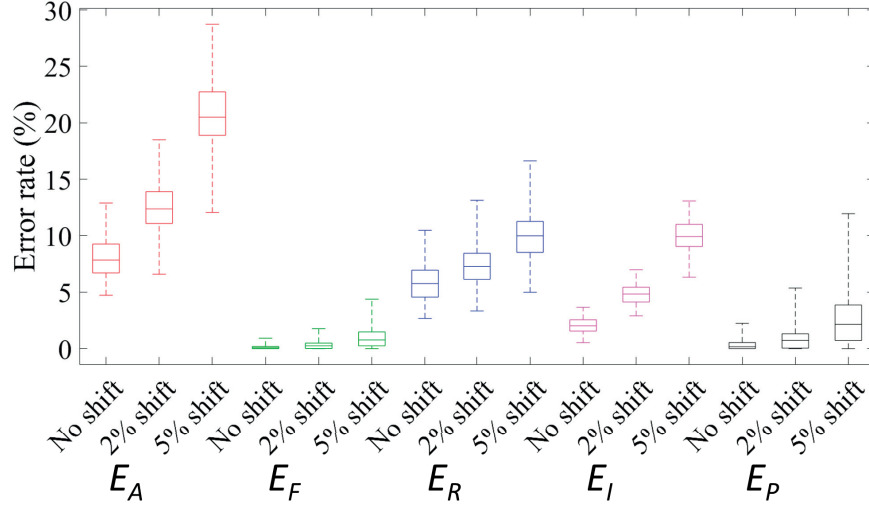


Figure 3.24 – Error rates ( $E_A$ : red,  $E_F$ : green,  $E_R$ : blue, and  $E_I$ : Magenta,  $E_P$ : black) as functions of different degrees of shifting (no shift, 2 % shift, and 5 % shift). The rectangle spans the first and third quartile of the error rate. The line inside each rectangle shows the median value. The two whiskers above and below each rectangle show the minimum and the maximum. The phantom map models used are 100 complete phantom maps with five fingers (Fig. 3.6(a)). The algorithm used was OVO-SVM with  $2 \times 2$  majority pooling.



## 4 Non-invasive Tactile Display: Design and Testing

The previous chapter (Chapter 3) has explored automatic phantom map detection employing support vector machines. After defining the phantom finger shapes and distribution, the next step in designing the sensory feedback system is to develop effective sensory feedback devices and tactile display. The design of tactile displays is an important step in constructing the overall sensory feedback system, which will be explained in the next Chapter (Chapter 5).

This chapter is organized as follows: in the first section, a short introduction of different feedback devices and psychophysical evaluation methods for tactile perception is given. In Section 4.2, the psychophysical evaluations of two types of commonly used vibrotactile devices are introduced. A multimodal tactile display was also build and the experiments and corresponding results are depicted in Section 4.3. At the end of this chapter, the work is summarized and concluded.

### 4.1 Introduction

Providing tactile information could potentially speed up reaction time, enhance the realistic feeling, and introduce more natural interaction with the system [188]. In this section, state-of-the-art non-invasive tactile displays (Section 4.1.1) and psychophysical methods (Section 4.1.2) are introduced.

#### 4.1.1 Non-invasive tactile display: state-of-the-art

A tactile display is an interface using tactation to provide information [189]. During the last decades, several research projects have focused on the design of tactile displays or tactile interfaces from psychophysical, mechanical, electrical, and computer science aspects. Tactile displays offer an independent sensory channel that the brain can process to further enhance a user's experience in a multimodal environment. The sense of touch provides a unique communication channel because it is a proximal sense and it is bi-directional [190]. Tactile displays are very suitable for communicating non-visual information [191] and they have

## Chapter 4. Non-invasive Tactile Display: Design and Testing

been used in many fields including: teleoperation or telemanipulation [192], navigation [193], gaming [194], virtual reality [195, 196], mobile devices [197], and so on.

Non-invasive tactile display devices can be categorized into four main modalities: mechanotactile devices, vibrotactile devices, electrotactile devices, and thermal devices [198].

One of the successful applications of mechanotactile devices in the market is the piezoelectric Braille readers [199, 200]. This kind of device is based on pin display driven by piezoelectricity.

Vibration based devices have been tested on navigation assistance system for car drivers [201, 202] and pilots [203]. For vibration stimulation, the variable dimensions for conveying information include: frequency, amplitude, waveform, duration, frequency and interval, beat, and location. Among the dimensions, waveform detection was reported as relatively insensitive and hard to distinguish [204]. Duration and location are mainly used to compose patterns. Variations of amplitude and frequency of a certain stimulation device are most commonly used and widely investigated [205, 206, 207, 208].

Electrotactile displays can be made thin, light, flexible and they have been used in sensory substitution [201], gaming [209], and virtual reality [210].

Thermal feedback has begun to be incorporated into tactile displays to convey thermal property of objects [211, 212, 213]. It is useful for object identification, material discrimination [214], and for creating a richer feedback about the virtual world [215]. It can also replace vibrotactile feedback in bumpy environment due to its robustness against body movement.

The comparison of the four types of non-invasive tactile displays is shown in Table 4.1.

Table 4.1 – Comparison of four non-invasive tactile modalities.

Modality	Speed	Power	Size	User acceptance	Coding parameters
Electrical	Fast	Small	Paper thin, diameter ranges from 5 to 10 mm	Can potentially invoke painful sensation	Voltage, current, frequency
Mechanical	Slow	High	Bulky	High	Force, frequency
Vibrational	Medium	Small	Small coin size	High	Amplitude, frequency
Thermal	Slow	High (1 to 100 W)	Thin (3 to 4 mm) but big (10 mm <sup>2</sup> )	High	Temperature

### 4.1.2 Psychophysical measurement methods

The study of psychophysics concerns the relationship on the applied stimuli and the human perception of those stimuli [216]. Psychophysical techniques allow quantitative measurement of the effects from different sensory modalities [217]. This introduction will mainly focus on outer psychophysics, which is the research area relating the physical inputs to the peripheral senses (the inner psychophysics focuses on the to relation between the brain and the perception).

#### Areas of psychophysical measurements

Most of the psychophysical measurements concern two areas: the *threshold measurements* (e.g. minimal detectable signal) and the *sensory attribute measurements* (e.g. perceived loudness, warm/coldness, stimulation pressure). The combination of the two areas provides a complete picture of a tactile display. However, the two areas focus on different aspects of psychophysical research: the threshold measurements describes the minimal energy needed from the physical stimuli, while the attribute measurements focus on the perceived effects on the human side.

##### *Threshold measurements*

The threshold measurements are useful for quantifying the sensitivity of a sensory system. The commonly used threshold parameters include: the minimal detectable signal or the absolute thresholds, the just noticeable differences, and the two-point discrimination distance.

The absolute threshold (RL as in *Reiz Limen*), or minimal detectable signal, is defined as the minimal needed energy of a stimulus to be detectable by humans [218].

The just-noticeable differences (JND) describes the minimal amount of changes that is necessary to evoke a sensation of change. It is often described by the Weber-Fechner equation in the form of

$$w = \frac{\Delta I}{I}, \quad (4.1)$$

where  $\Delta I$  represents the difference between just noticeable intensity change,  $I$  represents the initial intensity, and constant  $w$  is called Weber's ratio.

The *two-point discrimination distance* describes the smallest distance needed for a person to distinguish two simultaneously activated stimuli [219]. The commonly used testing methods include grating orientation task, raised letter recognition task, and two-point orientation discrimination task [220]. It is the lower boundary of the distance needed between two factors.

##### *Attributes measurements*

For the attribute measurement, the focus is on the humans' ability to identify or categorize stimuli. One of the commonly used test is localization, during which the testing subjects need to recognize the location of a certain stimuli. More details of sensory attribute measurements

are given below when describing scaling techniques.

### Psychophysical methods

Commonly used psychophysical methods can be categorized into classical psychophysical methods, methods based on signal detection theory, and scaling methods. Among these methods, classical and signal detection theory are used for threshold measurements while scaling techniques are used for attribute measurements.

#### *Classical psychophysical methods*

Classical psychophysical methods were proposed to detect both absolute and difference thresholds. Three commonly used classical methods are the constant stimuli method (Fig. 4.1(a)), the method of limits (Fig. 4.1(b)), and the method of adjustment.

The method of constant stimuli is the procedure of repeatedly using the same set of stimuli throughout the experiment and calculating the proportion of correct responses. The percentage values of correct responses are fitted with an ogive curve, called psychometric curve. The threshold is normally the value where the correct response is 50 %, although sometimes, the 25 % and 75 % thresholds are also used (Fig. 4.1(a)).

The method of limits is more time-efficient than the method of constant stimuli, albeit less precise. For absolute threshold measurement, the experimenter starts by presenting a stimulus well above or well below threshold; on each successive presentation, the threshold is approached by changing the stimulus intensity by a small amount until the boundary of sensation is reached. For difference threshold measurements, standard and comparison stimuli are presented in pairs, and on successive presentations the comparison stimulus is changed by a small amount in the direction of the standard stimulus. One variation of method of limit is the staircase method, shown in Fig. 4.1(b)

The method of adjustment is primarily used for the just-noticeable difference measurement, but occasionally can be also applied for measuring the absolute thresholds. For absolute threshold measurement, the experimenter first sets the stimulus intensity level either far below or far above the threshold and the testing subject directly adapts the intensity level until it is just perceivable for him or herself. For difference threshold measurement, the testing subject adjusts a comparison stimulus until it feels equal to the standard stimulus.

#### *Signal detection theory*

Signal detection theory is a probabilistic approach to model the human decision making process in the presence of noise. This method takes into account that the same stimulus may not always be perceived in the same way, due to, for example, environmental noise, artifacts, or human errors (Fig. 4.1(c)). The most commonly used paradigm is the one-interval, two alternative, forced choice experiment, often shortened as 1I-2AFC, where one stimulus is presented at each trial with two alternatives to choose from, and the participant has to indicate which of the two alternatives was present without a 'I don't know' choice. The response is

## 4.2. Psychophysical investigation of two types of vibrotactile devices

gathered and presented in a stimulus-response matrix, which was used to calculate the false alarm and hit rate. The advantage of the signal detection theory based method is its ability to estimate detection or discrimination performance independent of the response bias [221].

### Scaling methods

The scaling methods bridge the physical stimuli with the humans' perception by quantifying sensory attributes. The basic idea of scaling methods is to assign numbers to the physical stimuli property. There are some variations in experimental paradigms. The most direct method is to ask testing subjects to make quantitative judgments of perceived stimuli according to the number assigned by the experimenter. The other method requires the testing subjects to compare or match intensity, magnitude, or frequency of the perceived stimulus to that of a reference stimulus [216].

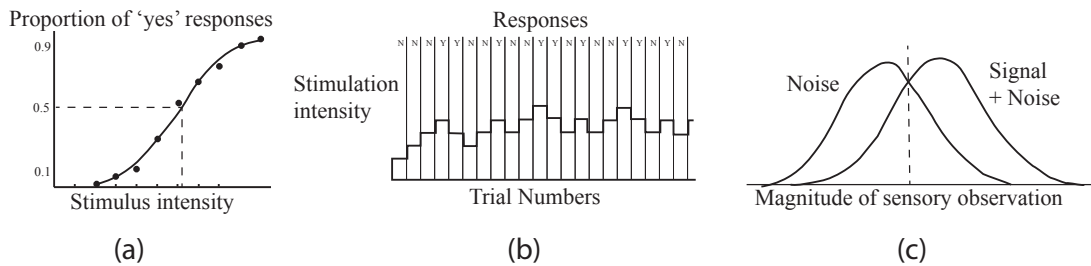


Figure 4.1 – Selected illustrations of some psychophysical methods: (a) the constant stimuli method, (b) the staircase method, and (c) signal detection theory.

## 4.2 Psychophysical investigation of two types of vibrotactile devices

In this section, a study to compare two types of commonly used miniature vibrotactile devices is explained. The purpose of this study is first quantify the perception thresholds of vibrotactile stimulation and then compare the effectiveness of the two forms of vibrational devices.

Due to their compact sizes, relative fast speed, and low power consumption, vibrotactile devices are often chosen to be integrated into wearable tactile displays. However, the human perceptions of vibrational signal is still not clear. Many of the previous works mainly focused on static tactile perception. For example, the classic work from Weber [222] discussed in details the static pressure thresholds. But static stimuli are essentially different from vibratory stimuli. When a vibrotactile stimulation is applied on the skin, instead of just a pressure, a mechanical wave will propagate on the skin as well as in the tissue under the skin [223]. So it is inappropriate to generalize the experimental results from static stimuli to vibratory stimuli. Some papers have discussed the skin perception when certain vibrotactile stimulation devices were mounted on different body locations. Cholewiak *et al.* investigated the vibrotactile localization performance on the forearm [223] and abdomen [224]. Jones *et al.* investigated vibrotactile pattern perception on the arm and back [225]. Biggs *et al.* reported the relative effectiveness of tangential and normal displacement of skin on forearm and fingerpad using a probe glued to the skin [226]. But no comparison has been made between different types of

vibrotactile devices.

The most common types of vibrotactile actuators are linear resonance actuators (LRAs) and eccentric rotating mass motors (ERMs). LRAs operate by oscillating a magnetic field to vibrate a magnet connected to the case by a spring and require an AC input. They typically have one resonant frequency at which they operate. A complex driving circuitry is needed for an LRA to track its their resonance frequency due to enviromental influence and manufacturing variations. ERMs are DC motors that have an offset mass rotating about the center axis. The non-symmetric rotating mass causes a displacement of the motor body to produce vibration. Frequency and amplitude of ERMs are coupled, which means that an increase in frequency (directly proportional to voltage) usually causes a linear increase in amplitude of vibration.

This work focuses on investigating the minimal detectable signals, just-noticeable differences, and minimum two-point discrimination distances of vibrotactile perception on the dorsal side of upper arm of healthy subjects using ERMs and LRAs. The mounting site was selected due to practical considerations: the upper arm provides more space than the forearm and the dorsal side is easier to mount the device without interrupting normal daily activities.

### 4.2.1 Experimental materials

The vibration devices used in the experiments are pancake-type linear resonant actuators (LRAs) and eccentric rotating masses (ERMs) from Precision Microdrives Ltd. LRAs provide a vertical vibration at resonant frequency; while ERMs provide a rotational vibration (Fig. 4.2). When the supply voltage changes, both the frequency and amplitude of the ERM change linearly with the supply voltage within normal operating region. The characteristics of the two devices are shown in Table 4.2. Two thin silicone (Hobby time) plates were designed and fabricated, embedded with 9 LRAs and 9 ERMs, respectively (Fig. 4.2). The control module consists of a microcontroller and custom-designed PCB boards with DRV2604 drivers (Texas Instruments Inc.). A LabView-based testing interface was used to guide participants through the experiments and to record data.

Table 4.2 – The characteristics of the LRAs [97] and the ERMs [227] used in this study.

Parameters	LRA	ERM
Diameter (mm)	10	12
Height (mm)	3.6	3.4
Frequency $f$ (Hz)	175	$f = 56.1V + 16.71$
Amplitude $A$ (g)	$A = 0.83V - 0.04$	$A = 0.6341V + 0.10$

V represents the driving voltage in volt

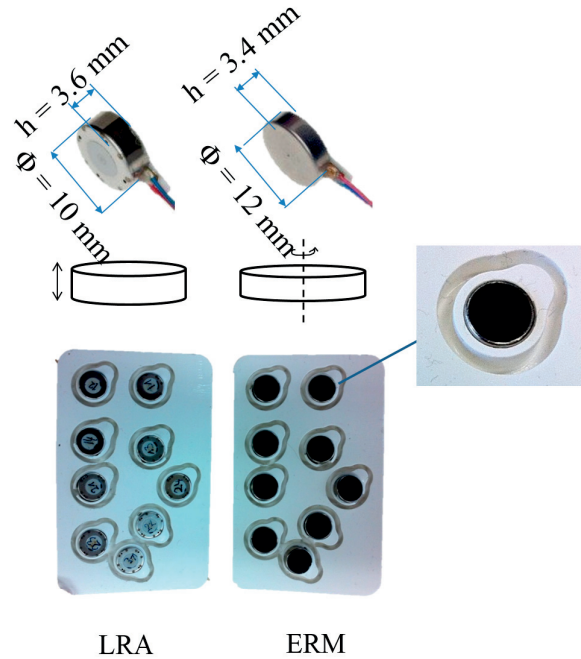


Figure 4.2 – The custom-designed stimulation array consisting of 9 ERMs or 9 LRAs embedded in the thin silicone plates. The LRA vibrates vertically. The ERM rotates around its axis. In order to avoid the cross-talks between each actuator, there is a ditch surrounding each actuator (shown in the zoom in). The vibrators are arranged to provide different distances.

### 4.2.2 Subjects

Fifteen subjects (14 males and 1 female, average age = 24.9, ranging from 22 to 31) participated in the experiments. All the participants had no previous experience with vibrotactile stimulation and had no known neurological deficit. Before the study, each participant provided an informed consent.

### 4.2.3 Experimental procedure

During the experiments, participants sat comfortably and rested the forearm on a small cushion placed on the table. They were wearing headphones with white noise to eliminate any audio cues coming from the motors. The custom designed stimulation array (Fig. 4.2) was fixed on the dorsal side of the subject's upper arm using a blood pressure cuff. The center of the stimulation array was placed in the middle line of the arm and in the middle between the shoulder and the elbow (Fig. 4.3).

All the participants engaged in the experimental session twice-weekly for two weeks. During each experimental session, the display was placed on the same area of the subject's upper arm.

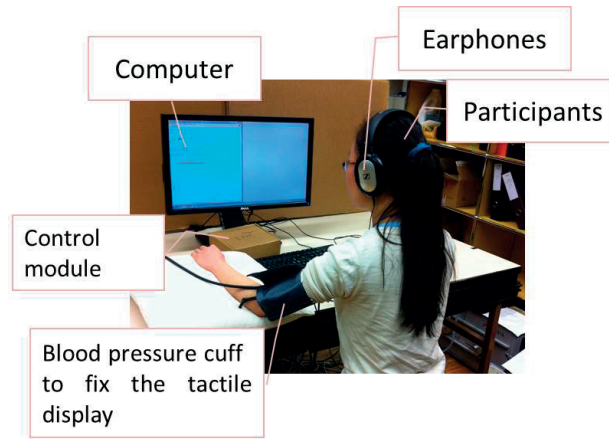


Figure 4.3 – The experimental setup: The participant rested the arm on a cushion placed on the table and followed the instruction shown in the computer screen. During all the experiments, the participant wore a headphone with white noise. The tactile display was fixed by a blood pressure cuff.

There was no training before each experiment. One experimental session consists of the three experiments explained below. All the experiments were designed using the constant stimuli methods (Section 4.1.2).

### Experiment 1: Minimum detectable signal using LRAs and ERMs

During this experiment, only a specific actuator in the middle of the array was activated. Participants were provided with 50 stimulations of different intensities. For LRA, the vibrating frequency was fixed at resonant frequency: 175 Hz, and the amplitude ranged from 0 g to 1.2 g. For ERM, the vibrating amplitude and frequency ranged from 0 g to 2.0 g and from 70 Hz to 185 Hz, respectively. Each stimulation lasted for 1 s. The order of stimulation was randomized. After each stimulation, the participants were asked to answer whether they could feel the stimulation or not.

### Experiment 2: Just-noticeable difference using LRAs and ERMs

During this experiment, only a certain actuator in the middle of the array was activated. The whole range of amplitude (or amplitude and frequency for ERMs) was linearly divided into 4 standard stimuli (shown in Table 4.3). At each stimulation, participants were first given a signal from one of the 4 standard stimuli for 1 s, and then another vibration signal (the comparison stimulus) within  $\pm 0.2$  g (for LRAs) or within  $\pm 0.31$  g and  $\pm 30$  Hz (for ERMs) of the standard stimuli for another 1 s. After each two vibrations, the participant was asked to answer whether he or she felt the differences in intensities. There were in total 40 vibration sets of each type of device and the order was randomized.

## 4.2. Psychophysical investigation of two types of vibrotactile devices

Table 4.3 – The standard stimuli for LRAs and ERMs

Number	LRAs			ERMs			
	Voltage (V)	Current (mA)	Amplitude (g)	Voltage (V)	Current (mA)	Amplitude (g)	Frequency (Hz)
1	0.63	26.0	0.48	0.95	16.9	0.70	69.7
2	0.79	30.9	0.61	1.18	21.0	0.85	83.0
3	0.94	36.2	0.74	1.42	25.0	1.00	96.2
4	1.10	41.6	0.87	1.65	29.0	1.15	109

### Experiment 3: Two-point discrimination using LRAs and ERMs

Thirteen different distances were tested on each participant: 0.0 mm, 20.0 mm, 22.0 mm, 24.4 mm, 28.0 mm, 29.7 mm, 31.9 mm, 34.0 mm, 36.0 mm, 37.4 mm, 39.5 mm, 41.6 mm, and 44.9 mm. One or two actuators were vibrating at the same time for 1 s and the participants were required to answer whether he or she felt two spatially separated vibrations. The participants were aware that there could be one or two active actuators for one test. The order of vibration is randomized. For LRAs, The vibration frequency was fixed at resonant frequency: 175 Hz and the vibration amplitude was 0.78 g. For ERM, the vibration frequency was at 100 Hz and the vibration amplitude was 1.04 g.

### 4.2.4 Results

The collected results of all the participants during 4 sessions are presented below.

#### Minimal detectable activation level results

In this study, each individual's answer was plotted and fitted with an ogive curve, resulting in the psychometric curve. The 50 % correct rate was chosen to determine the minimal detectable level. The overall average minimal detectable activation levels and the corresponding standard deviations of ERMs and LRAs are shown in Table 4.4. The average minimal detectable activation levels of ERM and LRA during each session are shown in Table 4.5. The overall distributions of minimal detectable levels are shown in Fig. 4.4. Because the results cannot be assumed to be normally distributed after the Lilliefors test, Wilcoxon test was used to compare the results between LRAs and ERMs. The comparison is shown in the boxplot in Fig. 4.4. The Wilcoxon test has shown that the minimal detectable levels of LRA and ERM belong to different distribution ( $p = 1.8139 \times 10^{-7}$ , indicating the statistical difference).

## Chapter 4. Non-invasive Tactile Display: Design and Testing

Table 4.4 – The average minimal detectable activation levels of ERM and LRA of all participants over the 4 sessions.

Parameters	LRA	ERM
Average $\pm$ standard deviation		
Frequency (Hz)	175	$69 \pm 5.8$
Amplitude (g)	$0.28 \pm 0.10$	$0.68 \pm 0.07$
Voltage (V)	0.39	0.92
Current (mA)	17.5	16.5
Power (mW)	6.88	15.2

Table 4.5 – The average minimal detectable activation levels of ERM and LRA during each session

Session	LRA	ERM	
	Amplitude (g)	Amplitude (g)	Frequency (Hz)
1st	0.22	0.69	67.0
2nd	0.26	0.67	67.0
3rd	0.29	0.69	67.0
4th	0.29	0.67	67.4

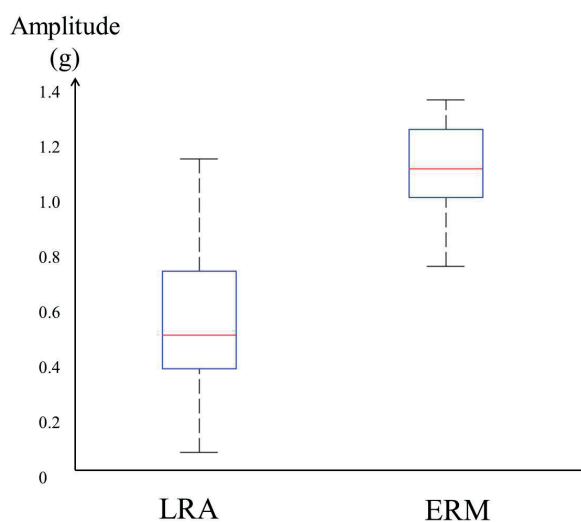


Figure 4.4 – The boxplot of minimal detectable level of LRAs and ERMs.

### Just noticeable difference results

During the just noticeable difference experiments, the participants could choose the answer between 1) *yes, I feel the difference*, 2) *no, I did not feel the difference*, or 3) *I am not sure*. In order

## 4.2. Psychophysical investigation of two types of vibrotactile devices

to evaluate the results qualitatively, an index JNDCI (just noticeable difference confidence index) is proposed:

$$\text{JNDCI} = \frac{m_{\text{diff}} + w \cdot m_{\text{ns}}}{N}, \quad (4.2)$$

where  $m_{\text{diff}}$  represents the occurrences when the participants felt the difference,  $w$  is the assigned weight, and  $m_{\text{ns}}$  is the occurrences when the participants were not sure.

When JNDCI = 0, it means that the participants cannot distinguish the two level of stimulation at all. When JNDCI = 1 and weight < 1, it indicates that the participants can distinguish the two levels easily without misclassifying.

The JNDCI plots of LRA and ERM at four standard stimuli are shown in Fig. 4.5.

By adding the ‘not sure’ answer, subjective influences was introduced. In order to observe how the ‘not sure’ answer affects the JNDCI, the JNDCI was plotted with different weights. By changing the weights, the plots of JNDCI simply shifted vertically without changing too much of the trends. This shows that the ‘not sure’ answer does not affect the total performance too much.

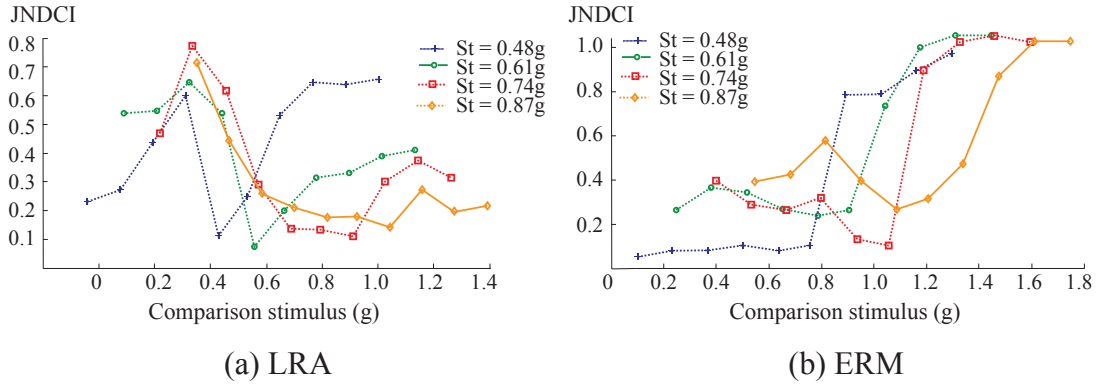


Figure 4.5 – The JNDCI plot of (a) LRA and (b) ERM at different starting levels when  $w = 0.3$ . St stands for standard stimulus. JNDCI stands for just noticeable difference confidence index, defined in (4.2).

### Two point discrimination results

The correct answer percentages in the two point discrimination tests using LRAs and ERMs are shown in Table 4.6. After conducting Wilcoxon rank sum test, there is no significant difference between LRAs and ERMs ( $p = 0.7950$ ) in the two point discrimination performance.

Table 4.6 – The average correct answer percentage of LRAs and ERMs during the two point discrimination experiments.

Distance (mm)	LRA			ERM		
	Single	Double	Not sure	Single	Double	Not sure
0	0.64±	0.19±	0.16±	0.64±	0.22±	0.14±
20 -30	0.23	0.58	0.20	0.36	0.48	0.16
30 - 40	0.24	0.6	0.16	0.32	0.56	0.12
40 - 45	0.39	0.47	0.14	0.34	0.52	0.15

#### 4.2.5 Discussion

The experiment results are compared between LRAs and ERMs in all three experiments. The factors that have potential influence on the results are also discussed.

##### Minimal detectable level discussion

The average minimal detectable level of LRA is lower than that of ERM. But the standard deviation of ERM minimal detectable level is smaller. One possible reason could be that ERM needs at least 0.8 V to enter the normal operating region (the linear region) while LRA needs only 0.15 V to enter the linear region. When the voltage is below the thresholds (0.8 V for ERM or 0.15 V for LRA), the vibration intensity is very small and hard to detect. The results that LRAs have a lower average minimal detectable level may be caused by the limitation of the devices, not by the nature of human perception.

To compare current devices, LRAs appear to be good candidates for an ON/OFF application because its relatively smaller power consumption and lower detectable level. It is possible to further reduce the detection thresholds by increasing the stimulation duration time and by increasing the area of stimulation [228].

##### Just noticeable difference discussion

From the results shown above, the stimulation changes provided by LRAs are harder to detect. Participants also reported the difficulty of detecting the intensity changes from LRAs. One possible explanation could be the different vibration nature of the LRA and the ERM. When the supply voltage is changed, the LRA vibrates at a fixed resonant frequency (in this case, at 175 Hz); while the ERM changes both the vibration frequency and amplitude. According to Stevens' power law [229], the perceived stimulation intensity  $\Psi(I)$  is given as:

$$\Psi(I) = K_f(A^2 f^2)^{b_f} \quad (4.3)$$

## 4.2. Psychophysical investigation of two types of vibrotactile devices

In which,  $K_f$  and  $b_f$  are frequency dependent parameters;  $A$  is the stimulation amplitude;  $f$  is the stimulation frequency.

In order to examine how the change of amplitude and frequency affect the perceived intensity, the derivatives of stimulation amplitude  $A$  and stimulation frequency  $f$  of equation 4.3 are calculated (shown in 4.4 and 4.5, respectively).

$$\frac{\partial \Psi(I)}{\partial A} = \frac{2b_f K_f}{A} (A^2 f^2)^{b_f} \quad (4.4)$$

$$\frac{\partial \Psi(I)}{\partial f} = \frac{\partial K_f}{\partial f} (A^2 f^2)^{b_f} + 2b_f K_f (A^2 f^2)^{b_f} \left( \frac{1}{A} + \frac{1}{f} \right) \quad (4.5)$$

Because LRAs vibrate at resonant frequency,  $\frac{\partial \Psi(I)}{\partial f}_{LRA} = 0$ . Assuming that frequency and amplitude are independent parameters contributing to the perceived vibration intensity, ERMs introduce a stronger change of feeling than LRAs.

Moreover, in ERM just noticeable difference tests, participants have a higher recognition rate when the second stimulation level is higher than the first one. On the contrary, for LRA, the recognition rate is higher when the first stimulation level is higher than the second stimulation level.

In summary, the vibrational JND could be influenced by the cross-influence of amplitude and frequency [230]. Some experimental results shows that vibrational JND are mediated by two types of mechanoreceptors: the Meissner's corpuscle and the Pacinian corpuscles [230, 231]. The two mechanoreceptors have different JNDs: the JNDs in the higher frequencies (mediated by Pacinian corpuscles) are more sensitive to relative amplitude changes.

### Two point discrimination distance discussion

For our study, when only one vibrator is vibrating, there is slightly higher than 50% of correct rate for both ERMs and LRAs (64%). As the distance increases, the size with the highest correct answer percentage is between 30 mm to 40 mm for both LRA (60% correct answers) and ERM (58% correct answers).

Compared to mechanotactile stimulation, the two-point discrimination distances of vibrotactile is much larger. One of the possible explanation is that the receptive field of Pacinian corpuscle is larger than the other mechanoreceptors. Another possible reason is the vibrational wave propagation [232, 233, 234]. Jones *et al.* have investigated the vibrational wave propagation using 3-axis accelerometers. It has shown that the vibrational amplitude gradually decreases as the measured points from the vibration center, following an exponential function.

During the post-experiment interview, 12 out of 15 participants (86 %) reported a ‘traveling signal’ feeling. Most of the time, participants could not feel two distinct vibrations. They distinguished the two actuator scenario from the one actuator scenario by the stronger vibration intensities and larger vibration areas induced by the former. The two actuator scenario introduces a more ‘blurry’ vibration sensation. This could be explained by funneling illusion or cutaneous rabbit effect [235]. This is a type of sensory illusion causing mislocalization on the skin. Two simultaneous vibratory stimuli at a certain distance can cause only one pulse. If the intensities of the two stimuli are the same, the felt stimulation locates in the middle of the two stimuli. Otherwise, the location of the felt stimulation is shifted to the actuator with a higher vibration intensity [235].

Some argue that the two point discrimination distance does not show the true spatial resolution of human perception because the summed intensity of two points stimulation and one point is different. The subjects could also use the intensity clue to distinguish the two points from one points [236].

One possible way to increase the recognition rate is to enhance the training. Because of the funneling illusion or cutaneous rabbit effect, the distinguishing between one and multiple vibration becomes rather unclear. Enhanced training might help participants to distinguish better between single-site vibrations and multi-site vibrations.

### Parameters affecting the performance

There are several factors that could affect the vibrotactile sensitivity: age, sex, individual difference, fatigue, mood, etc [228].

#### *Age*

During this experiment, no significant age induced differences in any of the experiment is observed using Wilcoxon tests. The reason could be that all the participants are young adults and the individual age gap is too small. However, some research has revealed age-related decrease in tactile sensitivity for both glabrous skin and hairy skin [237, 238, 239]. This decrease is not uniform across all the stimulation frequencies [240]. The reported data have shown that the vibrotactile sensitivity loss is greater at higher frequencies (mediated by PC channel) than in lower frequencies [240]. This could be explained by the loss of receptor due to aging.

#### *Gender*

Because there was only one female subject in our study, it is hard to analyze the sensitivity difference between two genders. However, several of previous research has indicated that there is no gender difference in vibrotactile perception. Verrillo *et al.* reported that there is no significant difference of the vibrotactile thresholds measured on the thenar eminence using different sinusoidal frequencies between the two gender groups [241]. This result is in accordance with a relatively recent experiment conducted by Bikah *et al*, which showed that

## 4.2. Psychophysical investigation of two types of vibrotactile devices

---

there was no significant correlation between gender and vibrotactile perception threshold at various hairy body locations [242]. Wiles *et al.* reported that gender did not affect the vibrotactile perception thresholds at toes or thumbs, but it affect the thresholds on the ankles [243].

### *Contact sizes*

This study only investigated devices with a fixed size. However, previous research has also shown that vibrational contact sizes have an influence on the absolute thresholds. Verrillo *et al.* have tested the relationship between absolute amplitude threshold and frequency on the thenar eminence. They observed that the relationship of absolute amplitude threshold of a vibrator with a large contact area ( $>0.32 \text{ cm}^2$ ) can be represented by a bi-limbed curve, changing with the frequency, but the absolute amplitude of a vibrator with a small contact area is not affected by the frequency changes [244]. The widely accepted theory to explain the differences caused by different contact sizes is the spatial summation ability of PCs. Gescheider *et al.* proposed a model of the correlation between contact size and minimal detectable level: the PC channel integrates vibrational energy (the square of amplitude  $A$ ) over the area of applied stimuli  $S$  [245]:

$$A^2 \times S = \text{Constant}, \quad (4.6)$$

where  $A$  is the amplitude,  $A^2$  represents the energy level, and  $S$  is the stimuli size [246].

It was also observed that at lower stimulation frequencies (below 40 Hz), the absolute thresholds for large contactors are the same as that of small contactors. In other word, there is no PC induced spatial summation at lower frequency because the other three channels do not have spatial summation ability [247]. One of the possible explanation is that PCs exist in the deep layers of Dermis, thus lower frequency stimulation cannot reach and active PCs.

### *Temperature*

The absolute thresholds are also influenced by temperature [248]. As the temperature shifted away from our normal body temperature (around  $34^\circ\text{C}$ ), but within non-painful sensation temperture (between  $15^\circ\text{C}$  and  $40^\circ\text{C}$ ), the absolute threshold becomes smaller, i.e. the skin becomes more sensitive. At the same time, the optimal frequency shifted from around 200 Hz to higher frequencies [249].

### *Learning effects*

During this two weeks, four sessions of experiments, no obvious performance improvement was observed. But participants reported that they were more comfortable with the tactile array after the first one or two sessions and it takes less time for participants to finish the same experiments.

### 4.2.6 Summary

In this study, experiments investigating the minimal detectable activation level, the just noticeable difference, and two point discrimination distance using coin type LRAs and ERMs were explained. The results collected from 15 participants, each has participated 4 times in 2 weeks, were shown and analyzed. For the minimal detectable activation level, LRAs have shown potential application to transfer binary information due to its lower detectable level and smaller power consumption. For the just noticeable difference, ERMs provide higher detection rate. For the two point discrimination experiment, funneling illusion and cutaneous rabbits illusion were reported. This could enrich the possible signals provided by the stimulation array.

## 4.3 Multimodal tactile display

Applying simultaneous multimodal stimulation can be advantageous. Firstly, from a neurological point of view, mechanotactile and vibrotactile elicit different mechanoreceptor channels (mechanoreceptors are introduced in Chapter 1 Section 1.2.1). Secondly, from a psychophysical point of view, the sensations introduced by the two types of stimulation is different: mechanotactile stimulation produces a focused point sensation, while vibrotactile stimulation produces a smooth vibration feeling. Moreover, the multimodal stimulation devices can potentially provide multi-dimensional and multimodal information in a compact configuration.

Previous researchers have considered and designed different types of multimodal systems. Caldwell *et al.* designed a cutaneous tactile feedback glove incorporating pressure feedback exerted from piezoelectric and thermal display [250]. Jimenz *et al.* has constructed a multimodal system [114]. But the system consists of three discrete systems, each providing a single modality. D'Alonzo *et al.* has integrated electrotactile and vibrotactile together [112]. The testing results on healthy subjects have shown that combined modality has better or similar performance than single modality. Considering that electrotactile can evoke painful feelings, in this work, incorporating mechanotactile and vibrotactile into a single device is proposed.

The aim of this study is to test the hypothesis that a multimodal tactile device, incorporating mechanotactile and vibrotactile feedback, can increase the subjects' performance in localization and intensity discrimination. The information transfer rate is also analysed in this study.

### 4.3.1 Multimodal stimulation device

The multimodal actuator was designed for providing richer information either for upper-limb amputees or as an wearable perceptual enhancement device, it should be light-weighted, small-sized, and low-power. The designed multimodal stimulation device consists of a micro

servo motor (Blue Bird BMS 303 ultra micro servo [251]) and a ERM vibrating element. The coin-type ERM was integrated into the arm of the servo motor (Fig. 4.6).

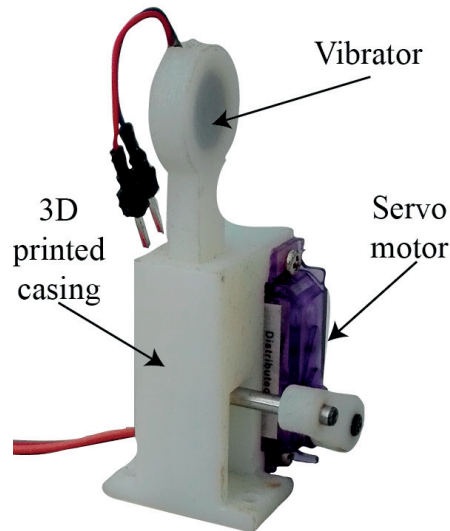


Figure 4.6 – The designed multimodal tactile display device. This multimodal tactile stimulation device consists of a servo motor, an ERM vibrator, and a custom-made, 3D printed casing.

#### 4.3.2 Experimental procedure

Twelve subjects participated the experiments. Five multimodal stimulation devices were arranged on the upper arm of each participants. The placement of the multimodal device guaranteed good contact between the skin and the stimulation device. All the subjects were first given 5 minutes to learn the stimulation patterns. After the learning phase, six sets of experiments were conducted:

- Finger localization using mechanotactile stimulation,
- Force level identification using mechanotactile stimulation,
- Finger localization and intensity identification using mechanotactile stimulation,
- Finger localization using multimodal stimulation,
- Intensity identification using multimodal stimulation,
- Finger localization and intensity identification using multimodal stimulation.

All the experiments applied scaling techniques (introduced in Section 4.1.2).

For the single modality experiments (experiment 1 to 3), only the servo motors were activated. For the multimodal modality experiment (experiments 4 to 6), the subjects received the vibrational signal together with a static force. The two modalities were applied by the same device at the same location. After each stimulation, the subject was required to answer as fast as possible which finger and which intensity (when applicable) was applied. For localization test (experiments 1 and 4), 25 stimulation were given. Each finger repeated 3 to 8 times. For intensity test (experiments 2 and 5), three levels of intensities were given. When using multimodal stimulation, the intensities of vibrotactile and mechanotactile are coherent. In total, 15 stimulation signals of different intensities were given. Each intensity level was repeated 5 times. The stimulation order was randomized. For localization and intensity identification test (experiments 3 and 6), in total, 75 stimulation signals were given. There are in total 15 possible location and intensity combinations. Each combination was repeated 5 times.

### 4.3.3 Experimental results and discussion

The detection accuracy is presented and the information transfer are calculated.

#### Identification accuracy

The averaged correct answer rates of all subjects are shown in Fig. 4.7. From Fig. 4.7, it can be observed that multimodal stimulation has only slightly higher accuracy than mechanotactile. Statistical tests have shown no significant difference between the two.

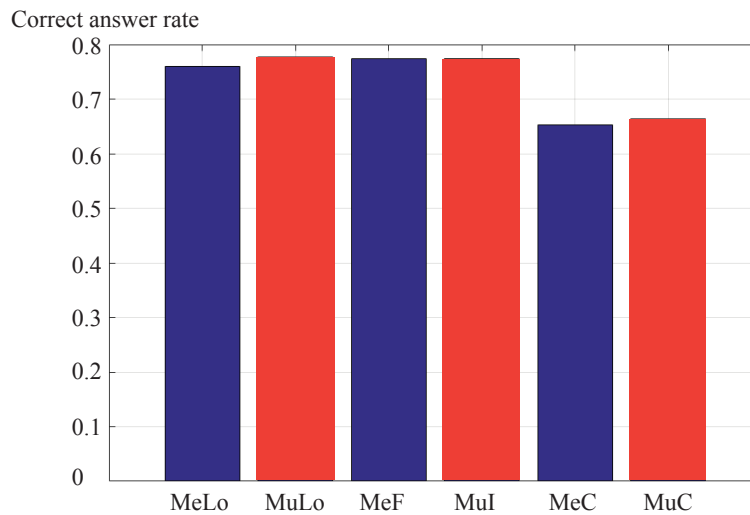


Figure 4.7 – The average detection accuracy of mechanotactile (Me) and multimodal (Mu) stimulation devices in localization (Lo), force level detection (F), intensity level detection (I), and combined (C) tests.

#### Information transfer

As a communication tool, the central limitation of a tactile display is its information transfer ability. The previous results mainly focus on the skin sensing ability (i.e., the resolution), the

information transfer property of a tactile display looks into how much information and/or how fast this information can be conveyed.

In this study, the information transfer (IT) is defined as:

$$IT = \sum_{j=1}^K \sum_{i=1}^K P(S_i, R_j) \log_2 \left( \frac{P(S_i / R_j)}{P(S_i)} \right), \quad (4.7)$$

where  $P(S_i, R_j)$  is the joint probability of stimulus  $S_i$  and response  $R_j$ , and  $P(R_j)$  is the probability of  $R_j$  [252].

The tactile information transfer rate for each experiment are calculated and shown in Table 4.7. From this table, we could observe that despite the reduced detection accuracy (Fig. 4.7), the combined test contains more information than the other methods. Multimodal stimulation has higher information rate than that of mechanotactile modality.

Table 4.7 – The tactile information transfer of mechanotactile and multimodal in localization, intensity identification, and combined tests.

Modality	Tests		
	Localization	Intensity	Combined
Mechanotactile	2.19 bit	1.09 bit	3.45 bit
Multimodal	2.24 bit	1.37 bit	3.75 bit

#### 4.3.4 Summary

In this work, a multimodal stimulation device incorporating two modalities: mechanotactile and vibrotactile was designed. A stimulation array consisting of 5 stimulation devices were tested on healthy subjects. The detection accuracy results showed that multimodal stimulation has comparable performance to that of mechanotactile stimulation (Fig. 4.7), but in this study the vibration provides an extra dimension, and thus resulting in higher information rate (Table 4.7). The subjects spontaneously reported that the extra feature relieved the mental load, since the vibration made them alert to the upcoming mechanotactile stimulation. To the best of my knowledge, this is the first attempt combining mechanotactile and vibrotactile into a single stimulation device.

In this study, only localization and intensity experiments were conducted. Other possible ways to use the hybrid stimulation device include incorporating different types of tactile information, such as vibrotactile stimulation as slip detection feedback and mechanotactile stimulation as pressure feedback.

### 4.4 Summary

In this chapter, three experiments and the corresponding results engaging vibrotactile and multimodal tactile displays were described.

For the vibrotactile modality, first, two types of commonly used vibrators were compared regarding their psychophysics properties using classical psychophysics methods. As far as I know, this is the first attempt to compare similar sized LRA and ERM type of vibrators. The results have shown the LRAs are suitable for conveying binary information (on and off) while ERMs are more effective in conveying multi-level information. Our goal is to provide sensory feedback to upper limb amputees. Because providing the applied force is essential for prosthetic control and a key parameter in sensory feedback, ERMs are chosen for further integration (Chapter 5 Section 5.2 and Section 5.3)

The second experiment focuses on the testing of multimodal tactile displays. The display consists of five multimodal stimulation devices providing vibrotactile and mechanotactile stimulation modalities. The scaling testing results of localization and intensity level identification did not show significant advantage of using multimodal devices, however, the multimodal devices provided higher information capacity, compared to that of the single modality. Moreover, testing subjects reported lower mental load when adding an extra modality. This study was conducted using limited number of testing subjects. The results can also be biased by the limited number of testing subjects.

The knowledge gained by testing the tactile displays were used to develop sensory feedback systems (e.g. the choice of vibrotactile devices) and the development will be described in the next chapter. Both modalities (vibrotactile and multimodal) were integrated into sensory feedback systems and testing with amputee subjects.

## 5 Sensory feedback system: design and testing

Typical sensory feedback systems for upper limb amputees consist of artificial sensors, communication and processing units, and tactile displays. The different tactile displays used for sensory feedback were introduced in Chapter 1 and Chapter 4. In the following introduction, only the artificial sensing for prosthesis and the measurement outcomes used for a fully-integrated sensory feedback system are presented. In the next three sections, three sensory feedback systems are introduced in each section. The first system is the WiseSkin system: a vibrotactile sensory feedback system with a wireless sensor network. This system aims at demonstrating the wireless technology used for body sensor network to improve flexibility and scalability. The second system is a multi-site, multi-modal sensory feedback system incorporating multi-modality stimulation devices to increase haptic vocabulary and psychophysical performance. This system also has applied wireless communication between the sensing part and the actuator part, so as to explore the potential application for tele-operation or tele-manipulation. The third system is a ‘bare-minimal’ system designed to fit the current commercial prostheses, many of which are 1-DoF grippers. The experiments designed to test the third system aim to test whether and to what degree this feedback system can assist the user in simulated activities of daily living. The three systems were designed for different purposes, and an overview of them is shown in Table 5.1.

### 5.1 Introduction

#### 5.1.1 Proprioceptive and exteroceptive sensing for prostheses

One of the challenges for providing natural sensory feedback is the limitation of the available artificial sensors. The sensory system is fundamental, the foremost part in providing sensory feedback. Sensing ability is crucial for the automatic control of prosthetic hands, without requiring visual attention. On the surface of the human body it is the hand that has the highest innervation density (more than 17,000 sensors on the glabrous skin of the hand) and tactile sensitivity. The currently available artificial sensors are a pale imitation of the mechanoreceptors on the hand.

Table 5.1 – Summary of reported sensors used in prosthetic hands

System	Sensors	Communication	Feedback devices
WiseSkin (Section 5.2)	Five barometric sensors, one on each finger	Wireless sensor	Five vibrotactile devices
Multi-site, multi-modality sensory feedback system (Section 5.3)	Five barometric sensors, one on each finger	Wireless communication between sensor block and actuator block	Integrated multi-modality feedback device (vibrotactile and mechanotactile)
Single-site, vibrotactile sensory feedback system (Section 5.4)	Two force sensing resistors on the thumb and index finger, respectively	Wired communication	Single vibrotactile device

The last decade has seen the development of many smart sensing systems based on different sensing techniques, to answer high demands in robotics [253, 254], medical research, minimal invasive surgery and keyhole surgery [255, 256, 257], automation [258], agricultural and food industry [259, 260, 261], the aerospace and automobile industries[262, 263, 264], and consumer electronics [265, 266]. However, not all of the technologies are suitable for prosthetic applications. Because of the nature of prosthetic devices, the sensors should be flexible, have low hysteresis and fast response speed, with low power consumption and low computational load. Both proprioceptive and exteroceptive sensing for prosthetic hands were reported in the literature (Table 5.2).

### **Proprioceptive sensing**

The most commonly measured proprioceptive parameters include finger or elbow joint position and hand shape. One approach for gathering proprioceptive information is through direct measurement. For example, in the RTR II hand [267] the Hall effect-based sensors were glued to the linear slides of the prosthetic hand actuation system. It is used to measure the displacement in the magnetic field created by the small magnet attached to the palm. Another example is the Cyberhand [268], where the Hall effect-based sensors were embedded in all joints of each phalange to measure the relative positions of each finger to the palm. The other proprioceptive measurement approach uses an indirect method by observing the electrical properties of the driving motors.

The commonly used proprioceptive sensors reported for prosthetic use include Hall effect-based sensors (e.g. magnetic encoder), cable tension meters, motor encoder (rotary encoder), and in rare cases, optical sensors and encoders.

**Exteroceptive sensing**

The exteroceptive sensing for prostheses is essentially tactile sensing. A tactile sensor is a device that gathers tactile information regarding the shape, texture, deformability, and temperature of contacting objects, as well as vibration, shear and normal force [269]. Similar to the proprioceptive sensing, tactile sensing methods can also be categorized into direct methods (measuring the physical stimuli property in contact with the hand) and indirect methods (measuring the actuator motor electrical properties). Due to the computational constraint and the limited space in prosthetics, tactile sensing mainly focuses on contact or force sensing, slip detection and temperature; while in humanoid robotics, the sensing modalities also include texture, softness, and so on. Many prosthetic hands [270, 271] use piezoresistance based sensors, either force sensing resistors or strain gauges on the hand surface, for the detection or measurement of contact forces. For some prostheses, for example the ACT hand [272], force is proportional to torque.

Some of the reported tactile sensors for prostheses include force sensing resistors (FSRs), capacitive touch sensors, strain gauges, thermistors (for temperature detection), acoustic sensors (for slip detection), and current sensors for the motor (Table 5.2). Very few of the prosthetic hands are equipped with optical sensors.

**Sensor description**

The working principles, advantages and disadvantages of some selected sensors are described in the rest of this section.

**Hall effect based-sensor** The working principle of a Hall effect sensor is that its output voltage changes according to the magnetic field. Hall effect sensors are commonly used for proximity switching, positioning, speed detection, and current sensing [280]. They are reported to be used for both proprioceptive and exteroceptive sensing. Hall effect sensors have high sensitivity, wide dynamic range, linear response, and mechanical robustness. The main drawbacks include its high sensitivity to the environmental magnetic field and the high computational load.

**Strain gauge based-sensor** A strain gauge based sensor is used for strain, torque, bending, deflection, and tension measurement. It is normally attached to the surface of the object under measurement. When the object deforms, the metallic foil inside the strain gauge is also deformed, causing the resistance to change. The resistance change can be measured through a Wheatstone bridge. Its thinness makes a strain gauge sensor suitable for wearable devices.

**Force sensing resistor** Force sensing resistors (FSRs) are also resistive sensors. They are made of conductive polymer. Though FSRs are not suitable for precision measurement, their

Table 5.2 – Summary of reported sensors used in prosthetic hands

Prosthetic hand	Sensing parameters	Sensors used
RTR II [267]	Slippage detection	Strain gauge based force sensors Hall effect based position sensors
	Force sensing	Strain gauges
CyberHand [268]	Joint position (hand position, object shape)	Eight Hall effect based sensor Three tensiometer Motor encoder Accelerometer
	tactile	On-off touch sensor Three-component force sensors
Southampton Remedi-Hand [34]	Position	Magnetic encoder
	Force	Current sensor on each motor
	Slip detection	Acousticc slip sensor
MARCUS hand [273]	Digit flexion	potentiometer
	Force and contact	FSR <sup>(1)</sup> (Interlink electronics)
	Slip	Miniature microphones
Ultralight anthropomorphic robot hand* [274]	Force and position	Four touch sensors Three flex sensors
MANUS hand [35]	Force and position	Hall effect based sensor
Hand with soft rubber skin [275]	position, velocity, force	A distributed touch sensor with more than 500 points
Five finger underactuated hand* [276]	Force	FSR <sup>(1)</sup> (FlexiForce sensors, Nitta Corp)
	Position measurement	Potentiometer
ACT hand [272]	Position sensing	Photo-sensors and encoders
	Force measurement	Motor current processing
FRH-4 hand [270]	Position	12-bit magnetic rotary encoders (AS5046 by AMS)
	Force	FSR <sup>(1)</sup> (Interlink Electronics)
SmartHand [277]	Finger joint position	15 Hall effect-based sensor
	Grasping force	5 tendon tension sensor based on strain gauge
	Position	Resistive potentiometer and digital encoder
	Contact	4 current sensors and four optical analog tactile sensors
SMA <sup>(2)</sup> -actuated hand 1 [271]	Force	FSR <sup>(1)</sup>
	Temperature	Thermistor (NTC, Panosonic)
SMA <sup>(2)</sup> -actuated hand 2 [278]	Joint deflection measurement	Strain-gauge based joint angle sensor
3D printed low-cost prosthesis [279]	Force	Force sensing resistor (FlexiForce sensors)
	Temperature	Thermistor

thinness, compatible sizes, robustness, readiness, and suitable sensing area makes them the best candidate for integration on the robotic hand. Their non-linearity normally needs extra processing and calibration.

**Optical sensor** An optical sensor commonly consists of a light source facing a compliant membrane. When the membrane deforms, the light distribution changes. The contact force and/or force distribution can thus be calculated. Optical based tactile sensors are immune to electromagnetic interference, flexible, sensitive and fast, but they are generally bulky. One of the other problems associated with optical sensors is the loss of light by micro bending and chirping, which causes distortion in the signal.

**Capacitive sensor** Capacitive sensors are often used in portable devices. They show high sensitivity and spatial resolution, wide dynamic range, linear responses [281]. However, the complex manufacturing process and readout / processing circuitry are a concern.

**Sound sensor** Both ultrasonic sensors and miniature microphones were have been tested for slip and texture detection [282, 283]. The ultrasonic sensors detect the slip and texture of an object in contact. They have a fast dynamic response and high resolution. But miniaturization is a major challenge when using ultrasonic sensors for prosthetic sensing.

**Piezoelectric sensor** Piezoelectric sensors detect the mechanical deformation and change the electrical polarization of the device [284]. They have a high frequency response, and are therefore suitable for vibration detection. Their other advantages include flexibility, lightness, and wide dynamic range. Their drawbacks include their sensitivity to temperature changes and a low sensitivity to static force.

### 5.1.2 Non-invasive sensory feedback outcome measures

The sensory feedback outcome measurements highly depend on the inputs (sensors), the feedback modalities, the functionality of the robotic hand which the system is attached to, and the testing subjects. Many sensory feedback systems consider only the feedback parts without any inputs. These types of system have been introduced in Chapter 4 and will not be repeated here. For a complete system, with a functional robotic hand or a virtual hand, inputs (sensors) and outputs (feedback devices), the reported outcome measures can be divided into a) psychophysical measures, b) kinematic measures, c) functional measures, d) embodiment measures, and e) cognitive load. However, there is still no clinical assessment of the sensory feedback system.

**Psychophysical measure** For psychophysical measures, the main interest is the capacity of the testing subject in perceiving the stimuli. Typically used outcome parameters include minimal detectable levels, just noticeable differences, two point discrimination and haptic information transfer (rate). Psychophysical measurements are the most basic measures and they are often applied for tactile display access (without a fully-integrated feedback system). This type of measure does not necessarily indicate the usefulness of the sensory feedback system, it is rather an indication of human sensitivity to certain modalities and stimulation patterns. Details on different psychophysical methods were described in Chapter 4.

**Kinematic measure** The kinematic measures are often associated with proprioceptive feedback. Commonly used methods include matching elbow angle with and without feedback, and matching hand aperture with and without sensory feedback [285, 286, 287].

**Functional measure** Functional measurement for sensory feedback is still at an early stage of development. Some tests create scenarios to mimic certain activities of daily living, for example: (virtual) grasping tasks, (virtual) egg manipulation tasks, and object lifting and identification. To the best of our knowledge, there is only one long-term experiment attempting to assess the clinical usability of the sensory feedback system [288]. During the test, commonly-used hand rehabilitation tests such as box and block test, block turn test, the cup test, and one test from the SHAP (clothpin relocation) were applied to evaluate the effectiveness of the sensory feedback system on three transhumeral upper limb amputees. So far, however, no test has reached the complexity and thoroughness of upper limb prosthetic clinical evaluation procedures such as SHAP [289].

**Embodiment test** Embodiment tests focus mainly on evaluating whether and to what degree a sensory feedback system helps the amputee to incorporate the prosthesis into his or her body image. Different types of modified rubber hand illusion tests were adopted. Subjective (skin conductance [105], proprioceptive drift [104], psychophysical temporal order judgement [67], physiological temperature measurement[67]) and objective(questionnaires) outcomes [67, 105] were applied.

**Cognitive load** Comparing the cognitive load with and without sensory feedback can also be considered as a type of functional measurement because the decreased cognitive or mental load while using the prosthesis can increase the usability and acceptance of the prosthesis. Some researchers applied questionnaires (e.g. NASA-TLX [290]) and interviews to compare the cognitive load subjectively, while others use standard tests, such as auditory 2-back tests [291] and measurement of the task completion time, to assess the mental load.

## **5.2 WiseSkin: a vibrotactile sensory feedback system with a wireless sensor network**

The WiseSkin system has been described briefly in Chapter 1. In this section detailed information about the system design, an evaluation and a pilot study are given. First, each element of the close-loop sensory feedback system is examined (Subsection 5.2.1). Then the experimental procedure and experimental results with a unilateral transradial amputee are described (Subsection 5.2.2). Finally, the study is summarized and its implications are examined.

### **5.2.1 System description**

This tactile feedback system consists of five wireless sensory nodes, stretchable artificial skin, a data processing unit, and a vibrotactile stimulation array (Fig. 5.1).

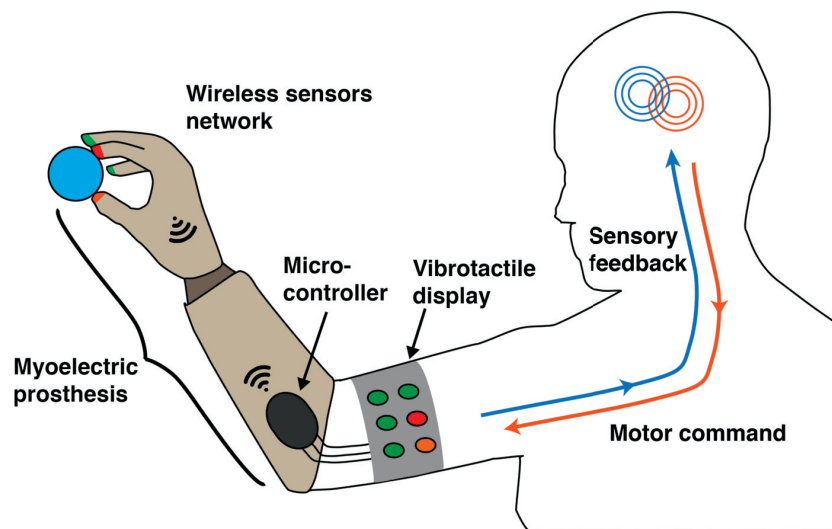


Figure 5.1 – The system illustration of the WiseSkin sensory feedback.

#### **Wireless sensory node**

One of the challenges for providing natural sensory feedback is the limitation of the available artificial sensors. The sensory system is the foremost part of the fundamental principle for providing sensory feedback. As the density of the tactile sensors grows, the wiring connection becomes cumbersome and the implementation and maintaining become costly. The use of wireless connections provides a cost-effective solution to the high density sensor network. In the past decades, wireless body sensor networks (WBSN) have been explored for use in implanted medical devices [292], ubiquitous health care [293], and patient monitoring [294]. WBSN offers mobility, scalability, and unobtrusive information transmission. In the

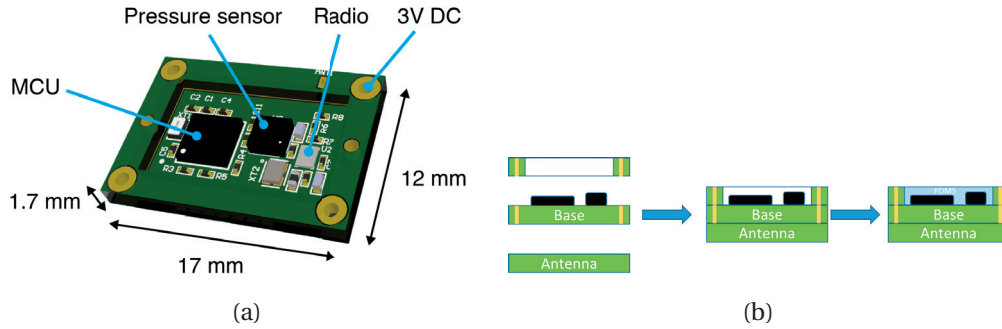


Figure 5.2 – Wireless sensor node (courtesy of CSEM). (a) wireless sensor node PCB, containing a barometric sensor, a micro-controller, and a wireless transmitter. (b) Schematic view of the process of manufacturing the wireless sensor node.

current study, a Bluetooth Low Energy (BLE) based wireless communication protocol is used to transmit tactile sensor data.

In the current system, a barometric sensor (LPS25H, ST Microelectronics [295]) was integrated with a micro-controller and a wireless transmitter (IcyTrx, CSEM, Switzerland [296]) on a PCB board (Fig. 5.2 (a)).

Barometric sensors have recently been used as tactile sensors [297, 298, 299]. They measure the absolute air pressure. For a barometric sensor chip, an inner chamber is communicating with the external environment through a ventilation hole, located on the top sensor surface. The chamber hosts a piezo-resistive transducer, whose physical deflection depends on the external air pressure. The chosen sensor has an operating range of 260 to 1260 hPa [295]. The whole device contains integrated circuits for signal filtering, amplification, temperature compensation, a digitization core and is endowed with an I<sup>2</sup>C or SPI communication protocol.

When carefully processed, they can be used as pressure sensors with good linearity, fast response speed, negligible hysteresis, and high sensitivity [269].

The sensory node PCB board applied a '3D PCB' concept. The module is composed of the base plate on which the pressure sensor and the radio module are integrated, the protection/-connection frame and an antenna mounted on the back. The on-chip antenna was a type of planar inverted-F antenna (PIFA) matched at 2.45 GHz.

In order to enable contact force transduction, the sensory nodes are hermetically sealed in the stretchable skin. The process was completed in a vacuum chamber to degasify the air trapped inside the ventilation hole (Fig. 5.2 (b)). The vacuum degasification process increases the sensitivity of the barometric sensors [300].

### Stretchable skin

The skin is not only a scaffold that holds sensory nodes and maintains electro-mechanical integrity, it is also a power supply for the sensory nodes and the wave-guide for wireless communication.

The design and principle of the power distribution system is presented in Figure 5.3. The scaffold is 3D printed using TangoBlack (Stratasys Ltd, USA [301]) and its shape is designed to fit the fingers and the palm of the hand prosthesis. On the tip of the scaffold and the end of the palm, holes were cut out for inserting the sensory nodes and the relay antenna. After inserting the nodes and antenna, the scaffold was encapsulated by two metallized planes. Conductive adhesive was used to connect the sensory nodes and the metallized planes electrically and mechanically. The whole stretchable skin system is connected to a 3 V power supply.

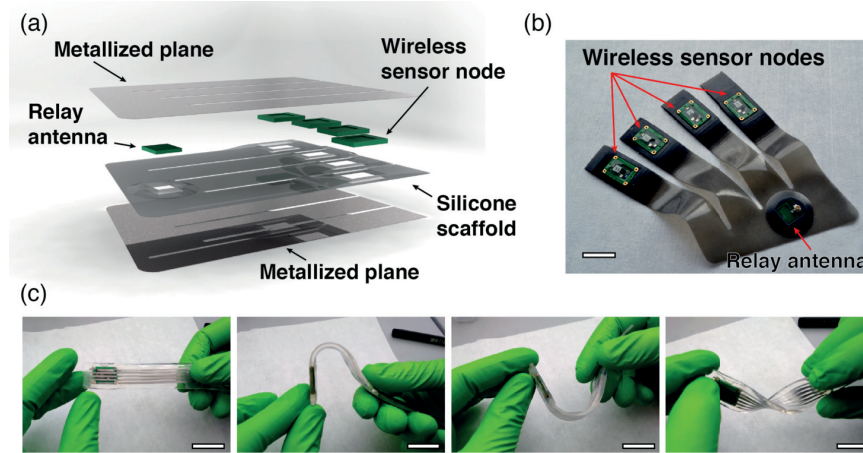


Figure 5.3 – Power distribution system. a) General view of the power distribution system. Wireless sensor nodes are embedded in a silicone scaffold and sandwiched between to metallized planes that power the sensor nodes and form a wave-guide for wireless communication. b) Wireless sensor nodes and relay antenna inserted into a 3D printed silicone scaffold. (c) Skin flexibility demonstration. Scale bar is 20 mm.

### Characterizing wireless sensory node embedded in the skin

The skin system was attached to the Ottobock hand prosthesis (Sensor Hand Speed). We applied a controlled force on the sensors embedded in the skin system using a load frame (Criterion C42, MTS [302]) equipped with a 100 N load cell. The hand was tied to a stand and positioned with its palm facing the load frame indenter. Pressure data from the sensor nodes was streamed to an iPad via Bluetooth Low Energy (BLE) protocol. A custom-designed LabView interface to visualize and save data from the iPad on a PC was developed. Acquisition rates were 10 Hz for load cell (force) data and 16.6 Hz for the sensor nodes (pressure) data. The indentation speed was kept constant at 0.2 mm/s while the maximum applied force was varied between 0.5 N and 25 N. The sensors displayed low hysteresis and large signal to noise

ratio (RMS noise of the barometric sensor is 1 Pa [295]) in the 0 N to 25 N force range (Fig. 5.4). Over the five sensor nodes characterized, two displayed a larger sensitivity and lower linearity. However, with the exception of sensor S2, all sensors had a repeatable response in the 0 to 25 N force range.

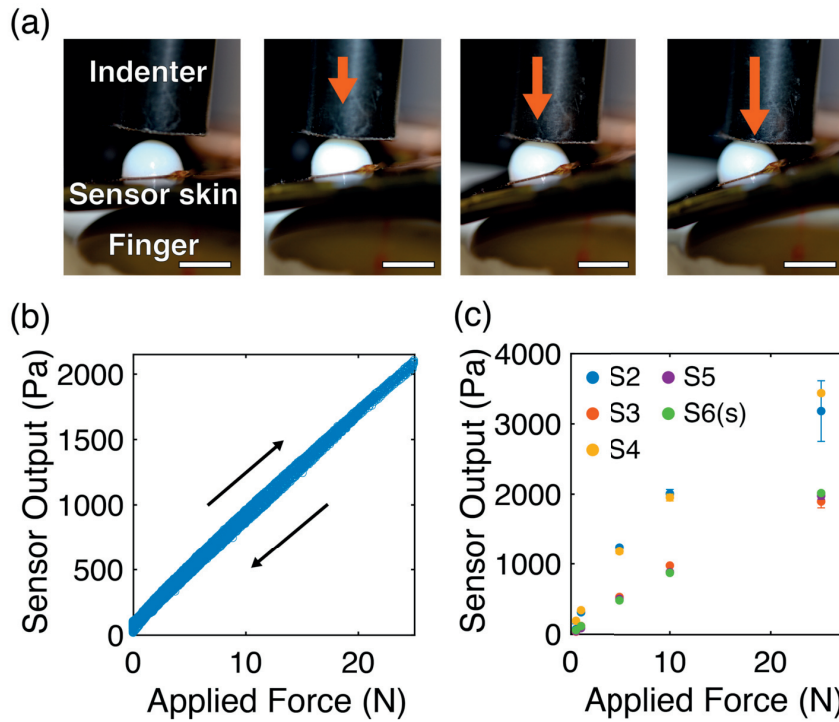


Figure 5.4 – a) Output of a sensor as a function of applied force. 10 loading and unloading cycles are represented. b) Output of five sensors as a function of applied force. Error bars represent standard deviation ( $n=10$ ).

### Communication protocol

The sensor data propagate through the metallization layers to the relay antenna and, subsequently, through the external antenna to an iPad. The iPad functions as the master node to which the sensor-communication modules are connected using BLE and a star topology (Fig. 5.5). With a dedicated application, the iPad receives and sends the sensor data through WiFi to a PC. A developed Labview software running on the PC processes the data and drives the tactile feedback display attached on the patient's residual arm.

### Vibrotactile display

There are two aspects to consider when providing sensory feedback: localization (the ability to locate where the stimulation is) and intensity identification (how many stimulation levels a person can distinguish). To achieve intuitive vibrotactile stimulation, the desirable vibration

## 5.2. WiseSkin: a vibrotactile sensory feedback system with a wireless sensor network

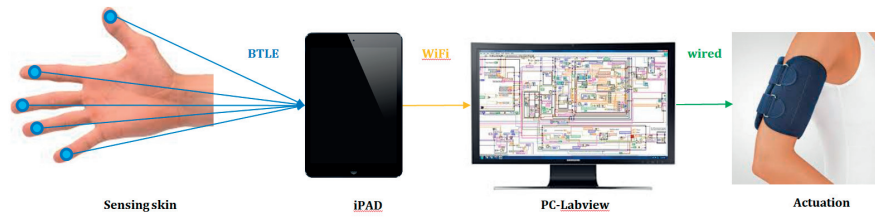


Figure 5.5 – Communication flow chart of the sensory feedback system.

frequency is about 250 Hz to stimulate the Pacinian corpuscles. The device should also be compact enough to be integrated with a hand prosthesis. Two types of pancake vibrators are appropriate: linear resonant actuator (LRA) and eccentric rotating mass (ERM). Previous experimental results suggest that ERM provides better intensity identification performance [303] and is therefore used in this study. The device is commonly used in electric toothbrushes and vibrating touch interfaces. Their robustness and safety have been proven in these applications. Five 10 mm ERM vibrators (Precision Microdrive, UK [227]) are inserted in the socket. To reduce the vibrational wave propagation, the vibrators are embedded through a damping-reduction silicone bed (similar to the one shown in Chapter 4). The processing units and the driver board were embedded inside the socket. ERM provides three distinct force levels. The sensed force is mapped to the vibration frequency through a look-up table.

### Power consumption estimation

For wearable devices, power is one of the major concerns. The total power consumption of five sensors, micro-controllers, and drivers are estimated from the data sheets and it is in the order of magnitude of 10 mW. For the actuators, the vibrator average power consumption with respect to the stimulation intensity is shown in Table 5.5.

Table 5.3 – Average power consumption of a single ERM vibrator used in the current system

Stimulation intensity	Frequency (Hz)	Average power consumption (mW)
Weak	60	67.5
Medium	150	105
Weak	200	126

To estimate the daily power consumption, the typical scenario described before in 5.2.1 was considered. The amputee will use the prosthesis for 16 hours and perform 3800 grasps daily [304]. The 3800 grasps consist of 20 % lateral grasps, 30 % precision grasps, and 50 % power grasps [305]. For lateral grasps, one actuator will be activated; for precision grasps, 3 actuators will be activated; for power grasps, 5 actuators will be activated [306]. Each grasping results in 1 s of activation time. So the estimated average power consumption for the sensory feedback system ranges from 16.3 mW for the best case to 90 mW for the worst case. The best case is

when all the grasps are light grasps (only weak intensities are needed) and the worst case is that all the feedback patterns are in high intensities. The capacities of commonly used built-in prosthetic batteries range from 700 mAH to 2000 mAH, and the typical nominal voltage can be 7.2 V and up to 11 V [307, 308]. So the available power provided by the integrated prosthetic batteries range from 315 mW to 1375 mW. So if we choose the large capacitance batteries, the multi-modal sensory feedback power consumption is around 6.5 % of the total capacity in the worst case. This will not increase the power consumption dramatically.

### 5.2.2 Experiments

The system was attached to an Ottobock VariPlus Speed hand [309]. A unilateral transradial amputee with referred phantom hand sensation was recruited and participated in this pilot study. The subject is a 40 years old male and lost his hand 20 years ago during a traumatic event. The amputee is a regular user of the same hand prosthesis without integrated tactile feedback. The sensory feedback system is adapted to the phantom map of the amputee subject. In this pilot study, we mainly focus on the localization performance using the vibrotactile stimulation because the effectiveness of vibrotactile stimulation intensity perception has been proven (Chapter 4), but the vibration wave propagation when embedded in the hard plastic socket is still not clear.

#### Hand phantom map shape and distribution detection

To measure and record the distribution of the hand phantom sensation of this amputee subject, we used a two-step procedure: first the amputee drew the shape of distribution on related body areas subjectively, and then the investigator verified and recorded the result.

The amputee drew the phantom map distribution on a piece of thin plastic foil, so that the result can be easily documented without any direct ink contamination on the skin. The hand phantom map drawn by an amputee is shown in Fig. 5.6. Then an investigator verified the result when the amputee was blindfolded. The investigator touched each area marked by the amputee, especially along the edges of each phantom digit, 5 times in a random order and asked the amputee to report his sensation. If there was any mismatch, the procedure of drawing and verifying was repeated for each phantom finger, to improve precision.



Figure 5.6 – The phantom map drawn by the amputee.

## 5.2. WiseSkin: a vibrotactile sensory feedback system with a wireless sensor network

Once the phantom map region was verified, the hand phantom map distribution was documented with two methods: 2D on the plastic foil and 3D by a 3D reconstruction software (Autodesk R 123D Catch R). The dimension and distribution could be precisely recorded by the two methods.

### Localization test

To test the effectiveness of the system, localization tests were conducted. This test assesses the subject's ability to localize tactile stimuli. During the experiment, the amputee subject sat beside a table with their arm resting on it. The subject had five minutes' training time prior to the test. During the training, the subject could get familiar with the stimulation patterns. During the test, the subject was blindfolded and given headphones to eliminate any visual or audio cues (Fig. 5.7). The experimenter randomly pressed a digit of the robotic hand and activated a vibrator. The stimulation lasted for 1 s. After each stimulation, the subject was required to answer as fast as possible which finger he felt. The experimenter then recorded the response. Each finger was pressed 10 times.

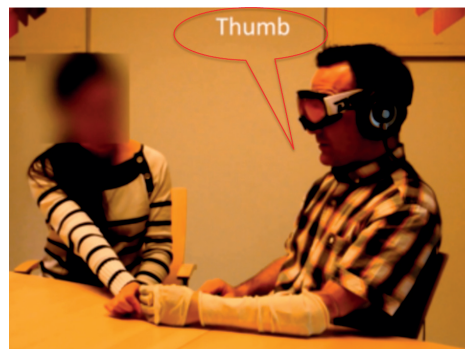


Figure 5.7 – During the localization test, the subject was blindfolded, wearing a noise isolating headset, and fitted with the sensory feedback system. The experimenter pressed the robotic finger and the subject answered which finger he felt being touched.

The testing subject could easily distinguish which finger was being touched. Although he did report a slight vibration of the socket, for him, the stimulation location was distinct enough to make the identification.

### 5.2.3 Summary

This section described the design and testing of a wireless sensory feedback system incorporating miniaturized wireless tactile sensory nodes, flexible, stretchable skin, and a vibrotactile tactile display. The typical power consumption and system delay were estimated. The system was tested on one transradial upper arm amputee subjects. This system provides scalability potentially to incorporate many sensors, in a high density sensor network, and the ability to cover large areas. Even though the system was designed and fitted for upper limb prostheses,

the system could also be adapted for teleoperation, remote control, and surgical robots.

### 5.3 Multi-modal, multi-site sensory feedback system for upper limb amputees

The goal of developing this system is to investigate the effectiveness of multi-modal stimulation in psychophysical evaluation.

#### 5.3.1 System integration

The multi-modal, multi-site sensory feedback system consists of five sensor modules integrated on a robotic hand, Bluetooth low energy (BLE) communication modules, and a multi-modal haptic display (Fig. 5.8). A graphic user interface implemented in LabView was designed for monitoring and interfacing with the testing subjects. The communication between the laptop, sensors, and actuator driving boards is through BLE.

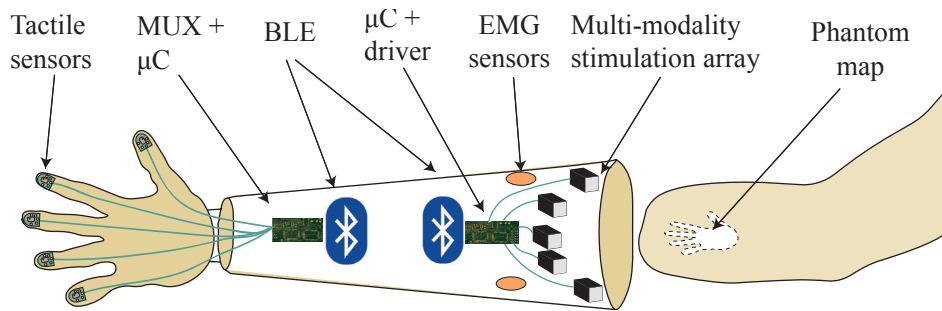


Figure 5.8 – Block diagram of the sensory feedback system integrated on a myoelectric prosthesis, consisting of five tactile sensors on the tip of the phalanges, processing and communication modules,

#### Tactile sensors

Commercial piezoelectric barometric sensors (MPL115A2 from NXP / Freescale [310]) are used as tactile sensors due to their high spatial resolution and their ease of integration with other electronic systems [269]. Each PCB, containing a barometric sensor and peripheral passive devices, was covered with a layer of silicone for protection and measurement. Each sensor module (the PCB covered a silicone layer) was attached to one robotic fingertip using a custom-designed, 3D printed cap (Fig. 5.9(a)).

After testing different types of silicone and coating thicknesses, Hobby-Time silicone (Glorex Hobby-Time 6.2407.405 Silicone Rubber, hardness shore = 35 A) with 5 mm coating was selected because it provides the smallest hysteresis and a good trade-off between sensitivity and measurement range. To improve the repeatability and reduce hysteresis still further, the silicone coating process was carried out in a vacuum system to reduce potential pinpoints

### 5.3. Multi-modal, multi-site sensory feedback system for upper limb amputees

---

caused by trapped air, which could cause measurement distortion.

The sensors were tested on an electromechanical universal test system (MTS Criterion C42.503, MTS [302]). Each sensor was mounted in a macroscopic cylindrical indenter. Controlled normal forces with different load values were applied to the skin sensor module. The calibration curve of each sensor is shown in Fig. 5.9 (b), which represents the averaged results over 10 repeated measurements.

Due to production variation and manual silicone coating, the calibration curve of each sensor was different. To compensate for the variations as well as the non-linearity, the sensor data was processed accordingly in the microcontroller so that the sensory data being sent had a uniform response to the applied force. From the testing results, we could observe a certain amount of hysteresis in the testing results, these could be caused by the silicone covering the barometric surface. This has been taken into consideration in providing the sensory feedback.

#### Communication protocol

To provide more flexibility to the whole system, the sensor array and the actuator array were connected through Bluetooth low energy (BLE) communication modules (CC2640R2F, Texas Instrument [311]). The sensory data from each sensor was combined through a multiplexer into a packet. The packet contains each sensor's ID (2 bits), pressure data (12 bits) and a time stamp (5 bits). The wireless communication protocol implemented in the system is a strict synchronous duty cycling protocol [312]. The communication module is scheduled to wake-up every 100 ms, *i.e.*, 10 pkts/s. During one communication cycle, the modules were active during 20 % of the time.

#### Multi-modal tactile display and driver

For sensory feedback, a multi-modal stimulation device was designed incorporating vibrotactile and mechanotactile modalities (Fig. 5.10a and Fig. 5.10b).

The mechanotactile stimulation was delivered by two DC servo motors (SPEKTRUM [313]) and the vibrotactile stimulation was delivered by a cylindrical eccentric rotating mass (ERM) vibrator (INEED Technology [314]). For the choice of vibrators, there are two available types: linear resonant actuators (LRAs) and eccentric rotating masses (ERMs). Previous research done in our lab has compared the two types of vibrators. The results have shown that ERMs are more effective in delivering different intensity levels [303]. Therefore, in the current hybrid stimulation device design, ERM was chosen. The stimulation array consists of five stimulation devices, corresponding to the five fingers. The design specifications of the multi-modal stimulation device are shown in Table 5.4.

Both the vibrators and DC servo motors were driven by pulse width modulation (PWM) signals generated through a microcontroller. The stimulation intensity is in direct proportion to the

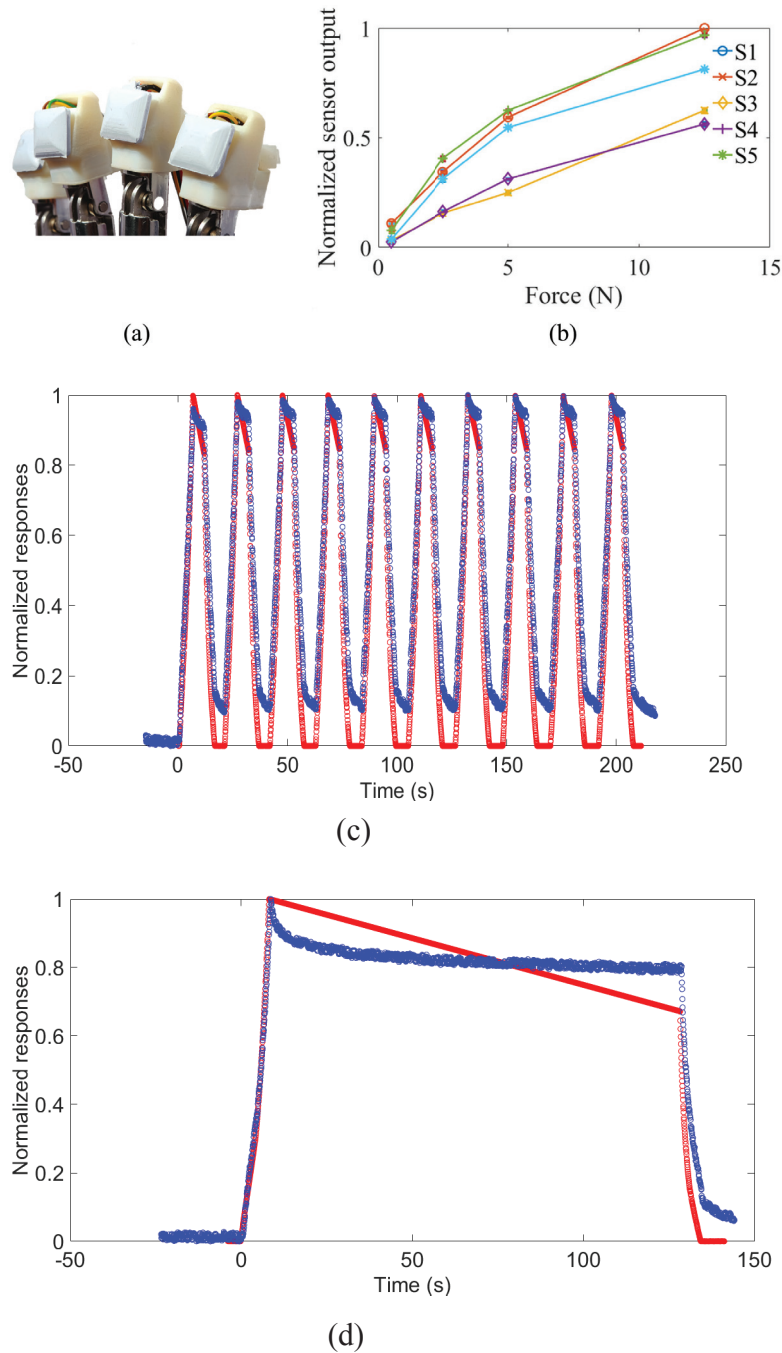


Figure 5.9 – (a) Each tactile sensor PCB, covered with a silicone layer, was attached to a 3D printed cap and mounted on the robotic hand fingertip. (b) Normalized sensor output *vs.* applied vertical force. S1 to S5 represent the sensors mounted on the robotic hand from thumb to little finger, respectively. (c) The sensor response (empty blue dots) and the applied force (empty red dots) plotted against time. (d) The sensor response (empty blue dots) and the applied force (empty red dots) in one testing circle.

### 5.3. Multi-modal, multi-site sensory feedback system for upper limb amputees

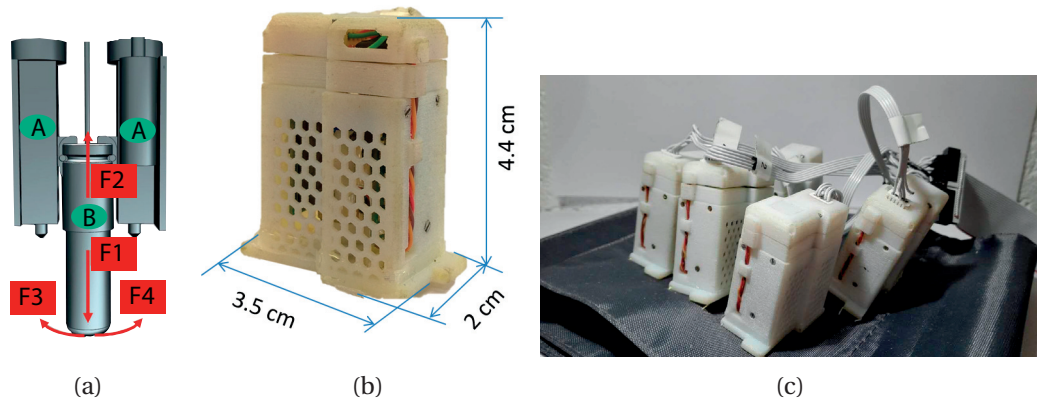


Figure 5.10 – (a) The design concept of the multi-modal sensory feedback device: two servo motors (A) push one cylindrical vibrator (B). (b) The multi-modal device integrated in a 3D printed casing. (c) The multi-modal sensor feedback array arranged to match the phantom map distribution of one test-case amputee.

Table 5.4 – Specifications of the multi-modal actuator

Parameter	Values
Size	35 × 20 × 44 mm
Weight	30 g
Input voltage	3.2 to 4.2 V
Vibration frequency range	100 to 240 Hz
Max pressure	4.4 N
Max stroke	6.5 mm

duty cycles of PWM signals. The duty cycles were proportional to the sensory value.

### Power consumption estimation

The total power consumption of five sensors, MUX, microcontrollers, and drivers is estimated from the datasheets and it is in the order of 10 mW. For the actuators, the average power consumption measurements are shown in Table 5.5.

Table 5.5 – Average power consumption of the actuators under three stimulation intensities

Modality	Stimulation intensity		
	Weak (mW)	Medium (mW)	High (mW)
Vibrotactile	67.5	105	126
Mechanotactile	820	1136	1400
Multi-modal	887.5	1241	1526

To estimate the daily power consumption, a typical scenario was considered. The amputee will use the prosthesis for 16 hours and perform 3800 grasp daily [304]. The 3800 grasps consist of 20 % lateral grasps, 30 % of precision grasps, and 50 % power grasps [305]. For lateral grasps, one actuator will be activated; for precision grasps, 3 actuators will be activated; for power grasps, 5 actuators will be activated [306]. Each grasping results in 1 s of activation time. So the estimated average power consumption in mW for the sensory feedback system with different modalities is:

- Vibrotactile: 16.3 mW for best case, 90 for worst case,
- Mechanotactile: 195 for best case, 333.75 for worst case,
- Multi-modal: 210.6 for best case, 295 for worst case.

The best case is when all the grasps are light grasps (only weak intensities are needed) and the worst case is that all the feedback patterns are in high intensities. The capacities of commonly used built-in prosthetic batteries range from 700 mAH to 2000 mAH, and the typical nominal voltage can be 7.2 V and up to 11 V [307, 308]. So the available power provided by the integrated prosthetic batteries ranges from 315 mW to 1375 mW. So if we choose the large capacitance batteries, the multi-modal sensory feedback power consumption is around 20 % of the total capacity, in the worst case. But in real-life, the percentage will be much lower. The capacities of commonly used built-in prosthetic batteries range from 700 mAH to 2000 mAH, and the typical nominal voltage can be 7.2 V and up to 11 V [307, 308]. So the available power provided by the integrated prosthetic batteries ranges from 315 mW to 1375 mW. So if we choose the large capacitance batteries, the multi-modal sensory feedback power consumption is around 20 % of the total capacity, in the worst case. But in real-life, the percentage will be much lower.

#### End-to-end message delay estimation

The total delay from the applied environmental pressure to the phantom map is the summation of the delays from the sensor, the communication, the processing unit, and the rise time of the actuators. From the data sheets, we could estimate that the delay of sensor reading, wireless transmission, and data processing is below 10 ms. The main delay was caused by the actuators. From the data sheets, the rise time of ERM is between 50 ms to 75 ms. The response time of the servo motor is around 50 ms. So the total delay is around 60 ms to 85 ms. This delay is within the range of 100 ms.

#### 5.3.2 Experiments

To test the effectiveness of the system, localization and intensity identification tests were conducted. Localization tests the subjects' ability to localize tactile stimuli. Intensity identification tests subjects' ability to distinguish stimulation intensity. During the testing, the subjects were blindfolded and wearing headphones to eliminate any visual or audio cues. The audio cues are not too strong and no testing subjects have complained about it.

#### Experimental setup and procedure

In the current study, three amputees (all male and left hand amputated): A1, A2, and A3 participated in the experiments. The testing subject sat beside a table with the arm rested on the table. For the amputee subjects with phantom maps (A1 and A2), the stimulation array arrangement was adapted to his phantom map shape and put on the phantom map. For A3, who does not have a phantom map, the stimulation array was evenly distributed with approximately 4 cm inter-distance between neighboring stimulation devices. A phantom map is a region on the body, normally appearing on the remaining stump, that could evoke sensation of the lost hand [164].

Each subject had five minutes' training time before the experiment started. During the training, the subject could get familiar with the stimulation patterns and remember the pattern. After training, the amputee subject participated in three sub-experiments using two different modalities. The three sub-experiments are localization tests, intensity identification tests and combined tests. The stimulation intensity was divided into three levels (Table 5.6). For multi-modal stimulation, the level of force and vibration are consistent. For localization tests, all five locations were stimulated and the stimulation intensity was fixed at medium level. For intensity identification tests, only middle finger position was stimulated. For combined tests, all combinations of five locations and three intensity levels were used. In each sub-experiment, every stimulation was repeated 10 times and the subject received 450 randomized stimulations in total. Each stimulation lasted for 1 s. After each stimulation, the subject was required to answer as fast as possible which finger they felt or/and the intensity felt. The researcher recorded the response.

Table 5.6 – Stimulation intensity overview. The current was measured and the amplitude and frequency were calculated from the datasheet.

	Mechanotactile (N)	Vibrotactile amplitude (g)	Vibrotactile frequency (Hz)
Level 1	1.5	0.7	90
Level 2	2.3	1.0	140
Level 3	4.4	1.8	175

### Experimental results and discussion

The experimental results for all three subjects and the overall average results using the two modalities, mechanotactile and multi-modal, are shown in Fig. 5.11. Overall, the average performance when using multi-modal has been slightly improved. It can be observed from Fig. 5.11 that A1 (amputee with a phantom map) gave an improved performance after adding the vibration cues in all the tests. However, for A2 and A3, the performance was degraded for certain tasks. The reasons could be (a) A2 has no previous experience with haptic feedback and (b) A3 has no phantom map, thus no intuitive mapping. All three subjects reported that the added vibrotactile cue served as a ‘warning’ signal, which helped them to focus on the coming signal. Therefore, less mental load was needed when using multi-modal stimulation.

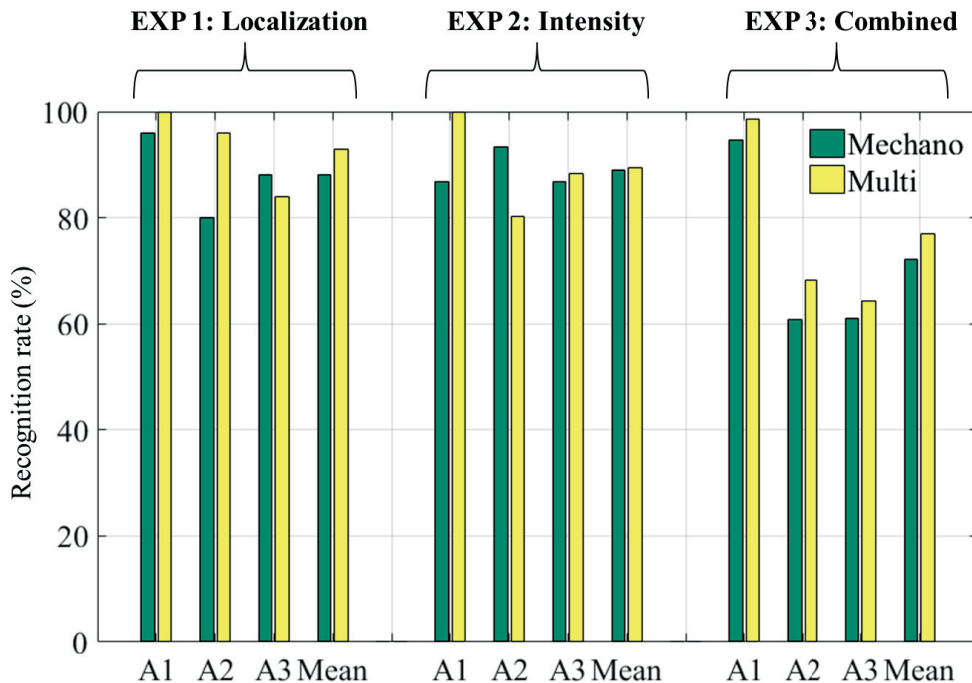


Figure 5.11 – The recognition rate of three amputees (A1, A2, and A3) and the averaged recognition rate during three sub-experiments.

### 5.3.3 Summary

This section describes a multi-modal sensory feedback system incorporating tactile sensors, wireless communication modules, and a haptic display with vibrotactile and mechanotactile stimulation capabilities. The estimated power consumption and delay are reported. The system was tested on three transradial upper arm amputee subjects using psychophysical evaluations: localization and intensity recognition accuracy. Compared to single mechanotactile modality feedback, multi-modal stimulation showed an improvement in the recognition rate. Additionally, multi-modal stimulation also reduces mental load. The results of this study are important for sensory feedback designs. They have shown the effectiveness of combining different modalities for sensory discrimination tasks. To the best of our knowledge, this is the first complete non-invasive sensory feedback system combining mechanotactile and vibrotactile stimulation, tested on amputee subjects. Despite the effectiveness of multi-modal stimulation, in the post-experiment trials, we have applied stimulation patterns by activating several stimulation devices simultaneously. The testing subjects reported being confused by the multi-stimulation patterns, as well as finding it hard to distinguish the patterns.

## 5.4 Single-site vibrotactile sensory feedback system

Our preliminary experimental results have indicated that multi-site stimulation can be disturbing. Multi-site stimulation can often be redundant because most of current prostheses have only one degree-of-freedom (DoF). In this section, a vibrotactile sensory feedback system equipped with one vibration element is presented. The system was integrated into a 1-DoF myoelectric prosthesis (OttoBock VariPlus Speed [309]) and one left-hand unilateral upper limb amputee tested the system in deformability detection tests and fragile object manipulation tasks. Experimental results and post-experiment interviews with the amputee demonstrated that the tactile sensory feedback system is intuitive to use and has positive impacts on the functionality of the prosthetic hand.

### 5.4.1 System description

The single-site vibrotactile sensory feedback system includes two force sensing resistors, signal processing units, actuator driver board, a solenoid actuator, and external power supply (Fig. 5.12).

#### Sensing

Two force sensing resistors (FSRs) (Interlink Electronics, Inc [315]) were chosen to measure the contact force because they are cost-effective and easy to integrate. Each FSR is encapsulated in a custom designed fingertip compartment and attached to the two active fingers. The chosen FSRs have 14 mm diameter circular active area.

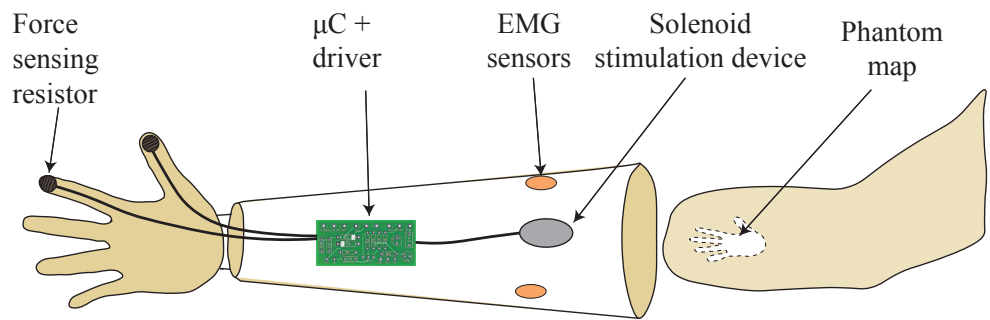


Figure 5.12 – Schematic of the single-site vibrotactile sensory feedback system

**Actuator control**

To increase the reliability, two, instead of one, FSR were integrated into the fingertip. The sensory data is used for generating pulse width modulation (PWM) signals for the actuators. The stimulation intensity is directly proportional to the duty cycle of the PWM signal, which is proportional to the sensed data.

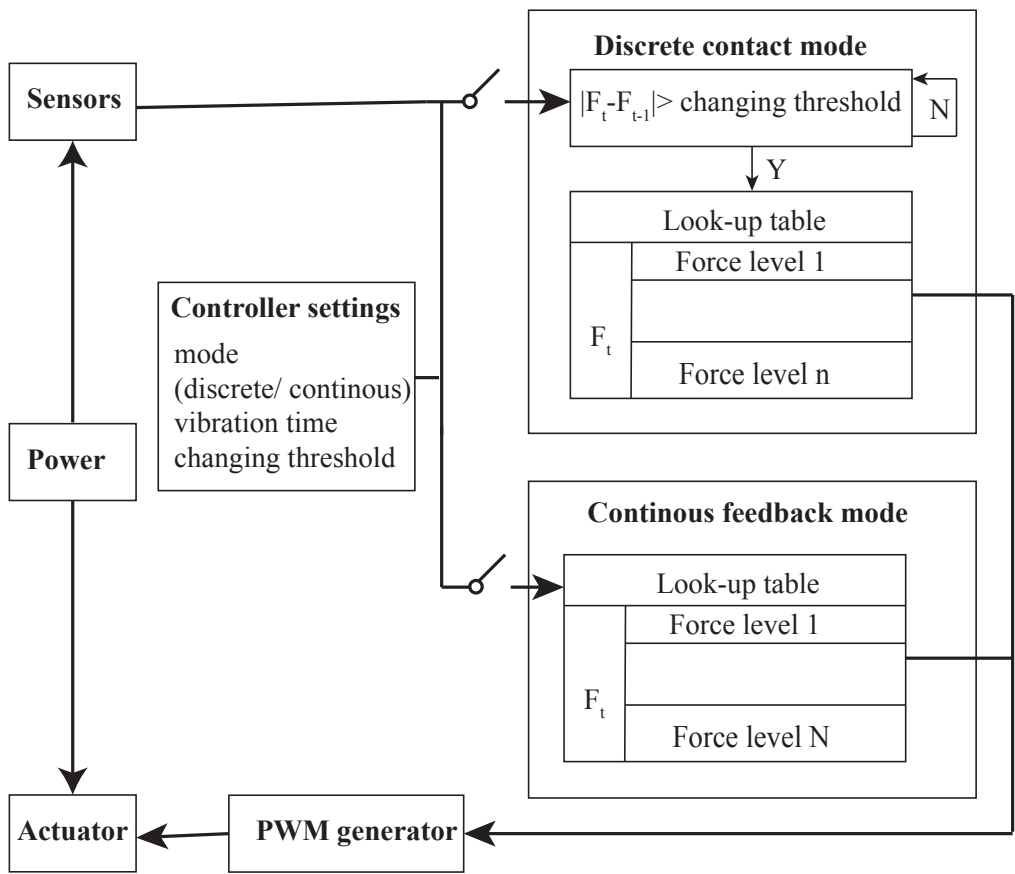


Figure 5.13 – The diagram of the sensory feedback system control.

### 5.4.2 Solenoid actuator

The designed and fabricated solenoids were characterized regarding the size, frequency range, force, and stroke. The characteristics of the solenoid are listed in Table 5.7.

Table 5.7 – Characteristics of the manufactured solenoid actuator

Parameter	Value
Size	Radius = 12.6 mm, Height = 13.6 mm
Weight	20 g
Frequency range	1 to 300 Hz
Max stroke	1 mm
Max force	306 mN

### 5.4.3 Experiments

One amputee participated in a set of experiments, including minimal detectable level and just-noticeable difference tests, as well as two active tests.

#### Subjects

The testing subject was a unilateral transradial amputee, who has been using different types of prostheses for more than 30 years. He has more than 10 years' experience using a myoelectric prosthesis. The testing subject lost his left (non-dominant) arm due to a traumatic event.

#### Experimental procedure

The test subjects underwent two types of active experiments and it is summarized in Table 5.8. The testing protocol consisted of two active experiments: the object deformability identification test and functional fragile object manipulation test. The experiments were conducted with both sensory-feedback-absent scenario and sensory-feedback-presence scenario on two separate days to eliminate any learning effect.

Table 5.8 – Experiment summary of single-site vibrotactile sensory feedback

Deformability test	Absolute deformability ranking	without FB with FB
	Comparative deformability identification	with FB without FB
Handling heavy and fragile objects	with FB without FB with FB without FB	

### Deformability test

The softness property of an object shows its ability to resist pressure. Unlike temperature, softness cannot be directly measured through a single touch or at one point in time. Softness detection normally involves exploration. Numerous sources of sensory information contributed to determine the object deformability properties. This test was designed to determine whether this single-modal, single-site feedback system, combined with amputee's knowledge of the EMG control (reflection of the hand position and hand open/close speed) are sufficient to recognize softness. Five equisized cubes (four sponges with different softness and one wooden cube) were used (Fig. 5.14). The deformability of the cubes is similar to that of many every day objects. The amputee determined the deformability degree by pressing the cubes.

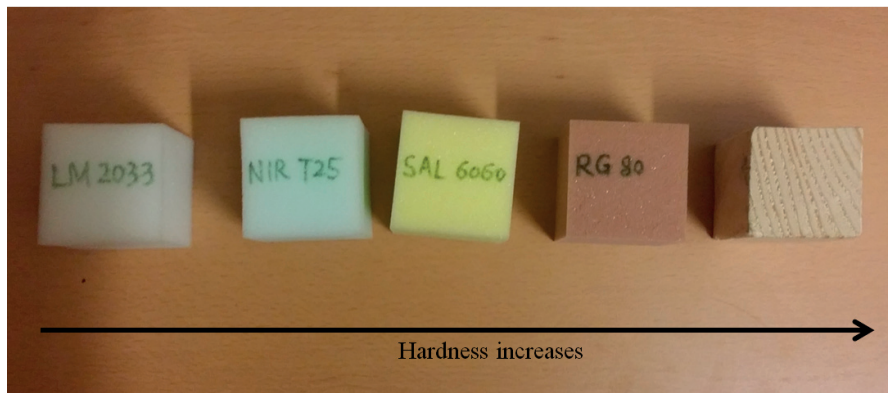


Figure 5.14 – Five equisized cubes: four sponges with different deformability and a wooden block.

The deformability test consists of two experiments: the first one is the absolute deformability identification and the second one is comparative deformability identification. During both experiments, the subject was blind-folded. The subject was given five minutes to get familiar with and remember the feedback patterns from pressing the sponges.

During the first set of experiments, the subject was presented one cube (from the four sponge cubes and the wooden cube) at a time (Fig. 5.14) and were required to rank them from the softest to the hardest as soon as possible (5 is the wooden cube and 1 is the softest white sponge in Fig. 5.14). In each trial, each cube was presented twice and in a random order. In total, six trials were conducted. On day one, the amputee was deprived of sensory feedback. And on day two, the amputee was presented with the sensory feedback. The performance was evaluated using an error score, defined as:

$$\text{error score} = \sum_{n=1}^{10} |\text{answer}_n - \text{real value}_n|, \quad (5.1)$$

where  $n$  is the number of object presented in one trial.

The error scores of the six trials were plotted in Fig. 5.15.

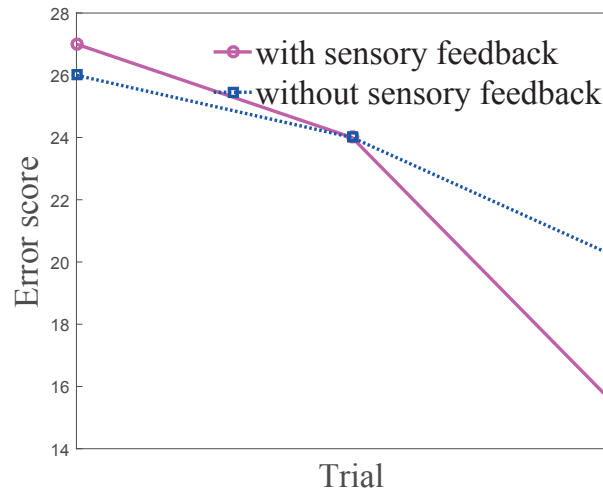


Figure 5.15 – The error scores in the absolute deformability testing with and without sensory feedback.

During the second set of experiments, the subject was presented with a pair of cubes, sequentially. He was required to identify whether the first cube was different (softer or harder) from the second one. In each trial, 25 pairs of cubes were presented, among which, 20 pairs were of different deformability and five pairs were of the same material. This trial was repeated four times, twice without sensory feedback and twice with sensory feedback.

The confusion matrix of the testing results with sensory feedback and without sensory feedback is shown in Fig. 5.16. It can be seen that the average correct rate is much higher when sensory feedback is presented (88 % when sensory feedback is present and 42 % with a lack of sensory feedback). When sensory feedback is present, the accuracy is slightly higher than random guessing (33 %) because the amputee reported that even though there was no additional sensory feedback, he could still get some feeling from the socket due to 30 years of experience using a prosthetic device.

Determining object deformability is very important for reliable and safe object handling. The way the amputee determines deformability is different from the way able-bodied subjects do. For able-bodied subjects using fingers, the process is one of direct contact. The deformability detection process can be characterized by two parameters: a) the rate of contact area increase and b) the rate of strain energy increase [316, 317]. For an amputee subject contacting the object with a prosthesis, it is an indirect skin contact scenario, because the touch is through a rigid surface. Some cutaneous information (skin deformation, contact area change, etc) is missing. In this case, the detection relies on the force and displacement. In the indirect contact scenario, the discrimination performance showed a significant reduction, compared to that of direct skin contact [318]. In our case, the amputee subject was able to estimate the hand position through the EMG control signal and combined it with the force feedback to estimate the deformability of the test material.

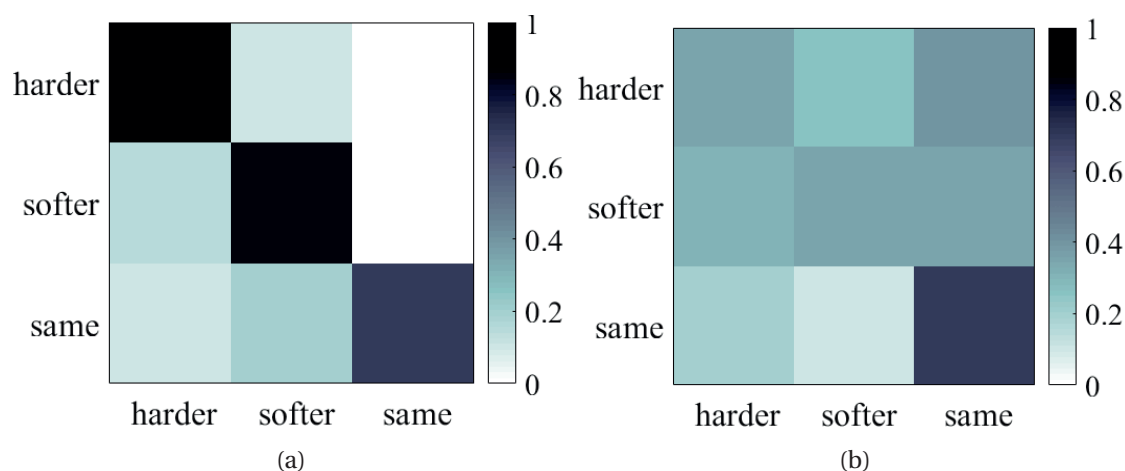


Figure 5.16 – The confusion matrix of the comparative deformability test (a) with sensory feedback and (b) without sensory feedback.

### Moving heavy and fragile objects

One of the challenges of using prostheses is to control the applied force. The typical grasping force of the prosthetic hand can reach 100 N [21, 18, 23]. Depending on the design of the prostheses, it is reported that prosthetic hands can apply up to 6 times the contact force of that applied by natural hands [319] This experiment is designed to test the effectiveness of the sensory feedback in regulating the applied force.

The experiment required the testing subject to move the heavy but fragile objects from one wooden stand to another 10 times without breaking any. The heavy and fragile objects were 3D printed hollow balls with a heavy piece of metal glued inside. The subject was first given five minutes to learn to adjust the force accordingly. Then he was given eight trials, half of which were with sensory feedback provided. The time needed to move the object 10 times was listed in Table 5.9. It can be observed that the time needed to perform the task become shorter after each trial. And the time needed when sensory feedback is present was shorter than when the amputee was deprived of sensory feedback.

Trial number	Time (s)	
	without sensory feedback	with sensory feedback
1	31.3	28.7
2	31.0	25.5
3	23.80	23.5
4	20.5	18.0
Average	26.7	23.9

Table 5.9 – Time needed to move the fragile objects for 10 times.

### 5.4.4 Summary

The sensory feedback system presented in this section is a ‘bare minimum’ system. It is compact, relatively fast, and suitable for integrating into the prosthesis. The testing results indicated that the sensory feedback device is indeed helpful for object discrimination and manipulation even with limited training. Moreover, the amputee expressed his appreciation for this system by saying that it was the first time he could feel his hand since he lost it 30 years ago.

## 5.5 Conclusion

This chapter presents three types of sensory feedback systems: one with advanced wireless sensory node and flexible skin, one with multi-modal stimulation, and one with only one vibrator representing the grasping force. The three systems were designed with different goals. The first system explores the possibility of applying advanced wireless communication technology to the tactile sensors. It shows the potential to incorporate dense sensory networks in the prosthetic hands of the future. The second system was developed to investigate possible ways to increase haptic communication channels. The third system was designed to fit the real world user scenario and to start examining the minimal requirement for a sensory feedback system to improve the amputees’ qualities of life.

All three system have demonstrated their effectiveness in their respective testing. The first two systems underwent psychophysical evaluation and the third system demonstrated the usefulness of sensory feedback in object deformability identification and object manipulation. The existing prosthetic hands vary in their mechanical designs and control strategies. The next step is to investigate the optimal sensory feedback system for different types of prostheses.



## 6 Conclusions

Hand amputation is a traumatic event that has a high impact on the amputee's life. Humans have been searching for functional replacement since the middle ages. The development of the active prosthesis started around the 1900s, with body-powered prostheses. Then, after the Second World War, myoelectric prostheses were developed and have evolved since then. Even though they are the most advanced prostheses in the market, they are still far from being a complete replacement for the natural hand. The applicability of the myoelectric prostheses relies on a closed-loop control, which contains both the feed-forward control path and the sensory feedback path. This thesis addressed both aspects in Chapter 2 and from Chapter 3 to Chapter 5, respectively.

### 6.1 Summary of the thesis work

#### 6.1.1 EMG classification

The first step towards guaranteeing the functionality of a prosthesis is to ensure natural and dexterous multifunctional control. The commercial prosthesis normally applies two EMG channels, and the control methods are limited to proportional control for 1-DoF hand and state machine control (sequential) for multi-DoF prostheses. The control methods are not as natural as pattern recognition based control methods. Chapter 2 of the thesis explored real-time control of the prosthesis by employing three types of datasets.

During this study, three aspects were investigated: the influence of commonly used time domain features and their combinations, the influence of overlapping window and increment sizes, and the influence of the proposed algorithms.

The empirical results indicate that the choice of classification algorithms depends on the dataset (the number of channels and the EMG signal quality), as well as the features intended to be used. However, there are some findings that were consistent through the datasets we tested: combined features generally produce better results than single feature, and the

increment size should be as small as computational power allows, to ensure good results.

### 6.1.2 Automatic phantom map detection

The first step in designing the sensory feedback system is to define the phantom map distribution. The current methods for phantom map detection are based on palpation, and roughly drawing the phantom finger edges on the skin of the remaining stumps. During this work, automatic phantom map detection algorithms were proposed, employing SVMs with different decomposition architectures. Fuzzy logic and active learning were also added to the SVMs.

In the absence of wearable dense stimulation arrays, the accuracy and timing aspects were tested on a) 400 flexible and realistic generated phantom map models, b) five reported phantom map images, and c) transformed phantom map images from the reported ones.

Among all the tested decomposition architectures, OVO-SVMs generally have higher classification accuracy, with a training time of less than 1 s. The added fuzzy logic further reduces the error rate by decreasing the influence of noisy data and unclassified regions. Moreover, active SVMs can interactively select samples for training, thus potentially providing more representative training data and increasing the detection accuracy when the initial size and batch size are chosen properly.

The potential performance using coarse stimulation arrays, designed primarily to provide sensory feedback, was also evaluated and found to be much lower than that of a dense array. They are thus unsuitable for refined phantom map shape detection. We therefore propose a two-step approach, firstly using a non-wearable dense array to detect an accurate phantom map shape, then applying a wearable coarse stimulation array, customized according to the detection results.

To the best of our knowledge, it is the first attempt at systematic phantom map shape detection. The proposed method can help optimize sensory feedback array arrangements, as well as tracking the changes of the phantom maps.

### 6.1.3 Non-invasive tactile displays

The next part of the thesis focused on the design and testing of the non-invasive tactile displays. Two types of modalities were considered: vibrotactile and multimodal.

For the vibrotactile modality, first, two types of commonly used vibrators were compared regarding their psychophysical properties using classical psychophysical methods. To the best of our knowledge, this is the first attempt to compare the performance of similar sized LRA and ERM types of vibrators. The results have shown the LRAs are suitable for conveying binary information (on and off) while ERMs are more effective in conveying multi-level information. Since providing contact force information is essential, ERMs are chosen for further integration.

The ERMs are then used to develop a tactile glove. The developed tactile glove was tested regarding their localization and force level detection ability. The experimental results indicated that tactile information applied to the back of the fingers was easy to interpret even without training. Another finding is that when the stimulation duration is less than 100 ms, the testing subjects tended to make more detection mistakes.

The third experiment focused on the testing of multimodal tactile displays. The display consists of five multimodal stimulation devices providing vibrotactile and mechanotactile stimulation modalities. The scaling testing results of localization and intensity level identification did not show any significant advantage of using multimodal devices, however, the multimodal devices provided higher information capacity, compared to that of the single modality. Moreover, testing subjects reported lower mental load when adding an extra modality.

The knowledge gained by testing the tactile displays were very useful in choosing the modality and devices used to develop sensory feedback systems.

### 6.1.4 Sensory feedback system integration and testing

Three types of sensory feedback systems were developed and tested during this preparation of this thesis. The first one is an exploratory system, integrated with advanced wireless sensory nodes embedded in the stretchable artificial skin and vibrotactile stimulation array. The second one is embedded with multimodal tactile display. The third one is a basic and cost-effective system with only one stimulation device in the socket to represent the grasping force.

Each of the systems serves a different purpose. The first system explored the possibility of incorporating wireless technology for the tactile sensors and indicated the potential to introduce a dense sensor network in the prosthetic hand. The second system shows possible ways to increase haptic perception by providing multimodal stimulation. The testing results on the most basic system has shown that even simple sensory feedback can improve some functionality of the prosthesis.

## 6.2 Outlook

This thesis aims at addressing the bi-directional control of the prostheses by investigating both the pattern-recognition based myoelectric control and the non-invasive sensory feedback. Many issues that still need to be addressed in order to provide practical wearable sensory feedback systems for upper limb amputees.

The first issue is the number of feedback devices. In this research, the testing subjects prefer one actuator representing the grasping force, instead of five actuators representing the contact force from five fingers. It is not clear whether this preference was due to the limitation of

## Chapter 6. Conclusions

---

the prosthesis (the testing prosthesis was a gripper with 1-DoF) or the sensory limitation of the user. With the limited number of testing subjects, it is hard to draw a conclusion at the moment. In the future, it would be very interesting to find out the optimum sensory feedback paradigm for different types of prostheses.

The second possible research direction is to test sensory feedback in a clinical setting. Most of the tests on sensory feedback systems were based on psychophysical measurement, which are mostly passive tests. However, in order to test whether sensory feedback is truly helpful, it is necessary to test the sensory feedback systems in activities of daily living (ADL) scenarios. There are many clinical tests for upper limb prostheses and hand rehabilitation. These tests could be adapted for sensory feedback evaluation.

## Bibliography

- [1] K. A. Raichle, M. A. Hanley, I. Molton, N. J. Kadel, K. Campbell, E. Phelps, D. Ehde, and D. G. Smith, "Prosthesis use in persons with lower-and upper-limb amputation," *Journal of rehabilitation research and development*, vol. 45, no. 7, p. 961, 2008.
- [2] F. Cordella, A. L. Ciancio, R. Sacchetti, A. Davalli, A. G. Cutti, E. Guglielmelli, and L. Zollo, "Literature review on needs of upper limb prosthesis users," *Frontiers in neuroscience*, vol. 10, 2016.
- [3] K. Østlie, I. M. Lesjø, R. J. Franklin, B. Garfelt, O. H. Skjeldal, and P. Magnus, "Prosthesis use in adult acquired major upper-limb amputees: patterns of wear, prosthetic skills and the actual use of prostheses in activities of daily life," *Disability and Rehabilitation: Assistive Technology*, vol. 7, no. 6, pp. 479–493, 2012.
- [4] M. T. Vincenzo P. Castelli, *Grasping the Future: Advances in Powered Upper Limb Prosthetics*. Bentham eBooks, 2017.
- [5] "6a: Upper limb prosthetics: O and p virtual library." [Online]. Available: <http://www.oandplibrary.org/alp/chap06-01.asp>
- [6] K. Berning, S. Cohick, R. Johnson, and C. Laura Ann Miller PhD, "Comparison of body-powered voluntary opening and voluntary closing prehensor for activities of daily life," *Journal of rehabilitation research and development*, vol. 51, no. 2, p. 253, 2014.
- [7] Hosmer | prosthetics and orthotics. [Online]. Available: <http://hosmer.com/>
- [8] "Revolutionizing Prosthetics." [Online]. Available: <http://www.jhuapl.edu/prosthetics/scientists/mpl.asp>
- [9] C. Guger, W. Harkam, C. Hertnaes, and G. Pfurtscheller, "Prosthetic control by an eeg-based brain-computer interface (bci)," in *Proc. aaate 5th european conference for the advancement of assistive technology*, 1999, pp. 3–6.
- [10] V. Aggarwal, A. Chatterjee, Y. Cho, R. Rasmussen, S. Acharya, and N. Thakor, "Non-invasive cortical control of a prosthetic hand with local machine control and haptic feedback," in *Meeting Biomed. Eng. Soc.(BMES 2006)*, 2006.

## Bibliography

---

- [11] M. Ortiz-Catalan, B. Håkansson, and R. Brånemark, "An osseointegrated human-machine gateway for long-term sensory feedback and motor control of artificial limbs," *Science translational medicine*, vol. 6, no. 257, pp. 257re6–257re6, 2014.
- [12] S. Raspopovic, M. Capogrosso, F. M. Petrini, M. Bonizzato, J. Rigosa, G. Di Pino, J. Carpaneto, M. Controzzi, T. Boretius, E. Fernandez *et al.*, "Restoring natural sensory feedback in real-time bidirectional hand prostheses," *Science translational medicine*, vol. 6, no. 222, pp. 222ra19–222ra19, 2014.
- [13] G. S. Dhillon and K. W. Horch, "Direct neural sensory feedback and control of a prosthetic arm," *IEEE transactions on neural systems and rehabilitation engineering*, vol. 13, no. 4, pp. 468–472, 2005.
- [14] G. Di Pino, A. Benvenuto, G. Cavallo, L. Denaro, V. Denaro, F. Ferreri, L. Rossini, M. Tombini, D. Accoto, M. Carrozza *et al.*, "In human implant of intraneural multielectrodes for controlling a 5-fingered hand prosthesis and delivering sensorial feedback," *Grasping the future: advances in powered upper limb prosthetics*, pp. 28–38, 2012.
- [15] C. M. Oddo, S. Raspopovic, F. Artoni, A. Mazzoni, G. Spigler, F. Petrini, F. Giambattistelli, F. Vecchio, F. Miraglia, L. Zollo *et al.*, "Intraneural stimulation elicits discrimination of textural features by artificial fingertip in intact and amputee humans," *Elife*, vol. 5, p. e09148, 2016.
- [16] K. Horch, S. Meek, T. G. Taylor, and D. T. Hutchinson, "Object discrimination with an artificial hand using electrical stimulation of peripheral tactile and proprioceptive pathways with intrafascicular electrodes," *IEEE Transactions on Neural Systems and Rehabilitation Engineering*, vol. 19, no. 5, pp. 483–489, 2011.
- [17] M. B. Reaz, M. Hussain, and F. Mohd-Yasin, "Techniques of emg signal analysis: detection, processing, classification and applications," *Biological procedures online*, vol. 8, no. 1, pp. 11–35, 2006.
- [18] "Ottobock, Sensor Hand Speed," <https://professionals.ottobockus.com/c/Sensor-Hand-Speed-w-Flex/p/8E41~58-R7%201~24-F>, accessed: 2017-02-02.
- [19] F. Tenore, A. Ramos, A. Fahmy, S. Acharya, R. Etienne-Cummings, and N. V. Thakor, "Towards the control of individual fingers of a prosthetic hand using surface emg signals," in *Engineering in Medicine and Biology Society, 2007. EMBS 2007. 29th Annual International Conference of the IEEE*. IEEE, 2007, pp. 6145–6148.
- [20] S. L. Carey, D. J. Lura, and M. J. Highsmith, "Differences in myoelectric and body-powered upper-limb prostheses: Systematic literature review." *Journal of Rehabilitation Research & Development*, vol. 52, no. 3, 2015.
- [21] "Ottobock, Michelangelo," <http://www.ottobockus.com/prosthetics/upper-limb-prosthetics/solution-overview/michelangelo-prosthetic-hand/>, accessed: 2017-02-02.

- [22] O. Bock, "Myoelectric compared to body-powered prostheses: clinical study summaries," <http://www.ottobock.pl/media/local-media/pdf/clinical-res/final-myoelectric-compared-to-body-powered-prostheses-study-summaries.pdf>, accessed: 2017-08-14.
- [23] "Touch Bionics, i-Limb," <http://www.touchbionics.com/products/active-prostheses/i-limb-ultra>, accessed: 2017-02-02.
- [24] "OttoBock, Bebionic," <http://bebionic.com/>, accessed: 2017-09-20.
- [25] "Vincent Systems, Vincent Evolution 2," <http://vincentsystems.de/en/prosthetics/vincent-evolution-2/>, accessed: 2017-02-02.
- [26] P. J. Kyberd, A. S. Poulton, L. Sandsjö, S. Jönsson, B. Jones, and D. Gow, "The tompaw modular prosthesis: A platform for research in upper-limb prosthetics," *JPO: Journal of Prosthetics and Orthotics*, vol. 19, no. 1, pp. 15–21, 2007.
- [27] "LUKE arm, Mobius Bionics," <http://www.mobiusbionics.com/the-luke-arm.html>, accessed: 2017-08-08.
- [28] J. W. Michael and J. H. Bowker, *Atlas of amputations and limb deficiencies: surgical, prosthetic, and rehabilitation principles*. American Academy of Orthopaedic Surgeons, 2004.
- [29] J. T. Belter, J. L. Segil, and B. SM, "Mechanical design and performance specifications of anthropomorphic prosthetic hands: a review," *Journal of rehabilitation research and development*, vol. 50, no. 5, p. 599, 2013.
- [30] M. C. Carrozza, G. Cappiello, S. Micera, B. B. Edin, L. Beccai, and C. Cipriani, "Design of a cybernetic hand for perception and action," *Biological cybernetics*, vol. 95, no. 6, p. 629, 2006.
- [31] S. A. Dalley, T. E. Wiste, H. A. Varol, and M. Goldfarb, "A multigrasp hand prosthesis for transradial amputees," in *2010 Annual International Conference of the IEEE Engineering in Medicine and Biology Society (EMBC)*,. IEEE, 2010, pp. 5062–5065.
- [32] M. G. Catalano, G. Grioli, E. Farnioli, A. Serio, C. Piazza, and A. Bicchi, "Adaptive synergies for the design and control of the pisa/iit soft hand," *The International Journal of Robotics Research*, vol. 33, no. 5, pp. 768–782, 2014.
- [33] N. Dechev, W. Cleghorn, and S. Naumann, "Multiple finger, passive adaptive grasp prosthetic hand," *Mechanism and machine theory*, vol. 36, no. 10, pp. 1157–1173, 2001.
- [34] C. Light and P. Chappell, "Development of a lightweight and adaptable multiple-axis hand prosthesis," *Medical engineering & physics*, vol. 22, no. 10, pp. 679–684, 2000.

## Bibliography

---

- [35] J. Pons, E. Rocon, R. Ceres, D. Reynaerts, B. Saro, S. Levin, and W. Van Moorlegghem, "The manus-hand dextrous robotics upper limb prosthesis: mechanical and manipulation aspects," *Autonomous Robots*, vol. 16, no. 2, pp. 143–163, 2004.
- [36] P. Kyberd and B. Jones, "The use of underactuation in prosthetic grasping," in *IFTOM-M/ASME International Workshop*, 2011.
- [37] C. L. Ventola, "Medical applications for 3d printing: current and projected uses," *Pharmacy and Therapeutics*, vol. 39, no. 10, p. 704, 2014.
- [38] "Open Bionics: 3D-printed prostheses," <https://www.openbionics.com>, accessed: 2017-08-14.
- [39] P. Slade, A. Akhtar, M. Nguyen, and T. Bretl, "Tact: Design and performance of an open-source, affordable, myoelectric prosthetic hand," in *Robotics and Automation (ICRA), 2015 IEEE International Conference on*. IEEE, 2015, pp. 6451–6456.
- [40] "Limbless Solutions: providing children with 3D-printed bionic limbs at affordable costs," <http://limbless-solutions.org/>, accessed: 2017-08-14.
- [41] J. Zuniga, D. Katsavelis, J. Peck, J. Stollberg, M. Petrykowski, A. Carson, and C. Fernandez, "Cyborg beast: a low-cost 3d-printed prosthetic hand for children with upper-limb differences," *BMC research notes*, vol. 8, no. 1, p. 10, 2015.
- [42] "Enabling the future: a global network of passionate volunteers using 3D printing to give the world a 'helping hand'," <http://enablingthefuture.org/>, accessed: 2017-08-14.
- [43] L. H. Smith, T. A. Kuiken, and L. J. Hargrove, "Real-time simultaneous and proportional myoelectric control using intramuscular emg," *Journal of neural engineering*, vol. 11, no. 6, p. 066013, 2014.
- [44] E. N. Kamavuako, D. Farina, K. Yoshida, and W. Jensen, "Relationship between grasping force and features of single-channel intramuscular emg signals," *Journal of neuroscience methods*, vol. 185, no. 1, pp. 143–150, 2009.
- [45] J. Rafiee, M. Rafiee, F. Yavari, and M. Schoen, "Feature extraction of forearm emg signals for prosthetics," *Expert Systems with Applications*, vol. 38, no. 4, pp. 4058–4067, 2011.
- [46] S. Micera, J. Carpaneto, and S. Raspopovic, "Control of hand prostheses using peripheral information," *IEEE Reviews in Biomedical Engineering*, vol. 3, pp. 48–68, 2010.
- [47] G. Staude, C. Flachenecker, M. Daumer, and W. Wolf, "Onset detection in surface electromyographic signals: a systematic comparison of methods," *EURASIP Journal on Applied Signal Processing*, vol. 2001, no. 1, pp. 67–81, 2001.
- [48] D. Cotton, A. Cranny, P. Chappell, N. White, and S. Beeby, "Control strategies for a multiple degree of freedom prosthetic hand," 2006.

- 
- [49] J. L. Segil, M. Controzzi *et al.*, “Comparative study of state-of-the-art myoelectric controllers for multigrasp prosthetic hands,” *Journal of rehabilitation research and development*, vol. 51, no. 9, p. 1439, 2014.
- [50] A. Hiraiwa, K. Shimohara, and Y. Tokunaga, “EMG pattern analysis and classification by neural network,” in *Conference Proceedings., IEEE International Conference on Systems, Man and Cybernetics*, pp. 1113–1115 vol.3.
- [51] N. Uchida, A. Hiraiwa, N. Sonehara, and K. Shimohara, “EMG pattern recognition by neural networks for multi fingers control,” in *1992 14th Annual International Conference of the IEEE Engineering in Medicine and Biology Society*, vol. 3, pp. 1016–1018.
- [52] T. Gupta, J. Yadav, S. Chaudhary, and U. Agarwal, “EMG pattern classification using neural networks,” in *Intelligent Systems Technologies and Applications*, ser. Advances in Intelligent Systems and Computing. Springer, Cham, pp. 232–242. [Online]. Available: [https://link.springer.com/chapter/10.1007/978-3-319-68385-0\\_20](https://link.springer.com/chapter/10.1007/978-3-319-68385-0_20)
- [53] F. H. Chan, Y.-S. Yang, F. Lam, Y.-T. Zhang, and P. A. Parker, “Fuzzy emg classification for prosthesis control,” *IEEE transactions on rehabilitation engineering*, vol. 8, no. 3, pp. 305–311, 2000.
- [54] S. Micera, A. M. Sabatini, P. Dario, and B. Rossi, “A hybrid approach to emg pattern analysis for classification of arm movements using statistical and fuzzy techniques,” *Medical engineering & physics*, vol. 21, no. 5, pp. 303–311, 1999.
- [55] M. A. Oskoei and H. Hu, “Support vector machine-based classification scheme for myoelectric control applied to upper limb,” *IEEE transactions on biomedical engineering*, vol. 55, no. 8, pp. 1956–1965, 2008.
- [56] S. Hendry and S. Hsiao, “Chapter 24 - the somatosensory system,” in *Fundamental Neuroscience (Fourth Edition)*, L. R. Squire, D. Berg, F. E. Bloom, S. d. Lac, A. Ghosh, and N. C. Spitzer, Eds. Academic Press, pp. 531–551.
- [57] M. Grey, “Proprioceptive sensory feedback,” *eLS*, 2010.
- [58] P. R. Burgess and E. R. Perl, “Cutaneous mechanoreceptors and nociceptors,” in *Somatosensory System*, ser. Handbook of Sensory Physiology, A. Iggo, Ed. Springer Berlin Heidelberg, 1973, no. 2, pp. 29–78.
- [59] C. L. Reed, “Tactile perception,” in *Encyclopedia of the Human Brain*, V. S. Ramachandran, Ed. Academic Press, pp. 545–556, DOI: 10.1016/B0-12-227210-2/00343-5.
- [60] K. O. Johnson, “The roles and functions of cutaneous mechanoreceptors,” *Current opinion in neurobiology*, vol. 11, no. 4, pp. 455–461, 2001.
- [61] A. Blank, A. M. Okamura, and K. J. Kuchenbecker, “Identifying the role of proprioception in upper-limb prosthesis control: Studies on targeted motion,” *ACM Transactions on Applied Perception (TAP)*, vol. 7, no. 3, p. 15, 2010.

## Bibliography

---

- [62] R. L. Sainburg, M. F. Ghilardi, H. Poizner, and C. Ghez, "Control of limb dynamics in normal subjects and patients without proprioception," *Journal of neurophysiology*, vol. 73, no. 2, pp. 820–835, 1995.
- [63] O. Favorov, T. Sakamoto, and H. Asanuma, "Functional role of corticoperipheral loop circuits during voluntary movements in the monkey: a preferential bias theory," *Journal of Neuroscience*, vol. 8, no. 9, pp. 3266–3277, 1988.
- [64] C.-F. Ekerot, B. Larson, and O. Oscarsson, "Information carried by the spinocerebellar paths," *Progress in brain research*, vol. 50, pp. 79–90, 1979.
- [65] C. Pylatiuk, S. Schulz, and L. Döderlein, "Results of an internet survey of myoelectric prosthetic hand users," *Prosthetics and orthotics international*, vol. 31, no. 4, pp. 362–370, 2007.
- [66] F. Clemente, M. D'Alonzo, M. Controzzi, B. B. Edin, and C. Cipriani, "Non-invasive, temporally discrete feedback of object contact and release improves grasp control of closed-loop myoelectric transradial prostheses," *IEEE Transactions on Neural Systems and Rehabilitation Engineering*, vol. 24, no. 12, pp. 1314–1322, 2016.
- [67] P. D. Marasco, K. Kim, J. E. Colgate, M. A. Peshkin, and T. A. Kuiken, "Robotic touch shifts perception of embodiment to a prosthesis in targeted reinnervation amputees," *Brain*, vol. 134, no. 3, pp. 747–758, 2011.
- [68] M. R. Mulvey, H. Fawcner, H. Radford, and M. Johnson, "The use of transcutaneous electrical nerve stimulation (tens) to aid perceptual embodiment of prosthetic limbs," *Medical hypotheses*, vol. 72, no. 2, pp. 140–142, 2009.
- [69] K. L. Collins, A. Guterstam, J. Cronin, J. D. Olson, H. H. Ehrsson, and J. G. Ojemann, "Ownership of an artificial limb induced by electrical brain stimulation," *Proceedings of the National Academy of Sciences*, p. 201616305, 2016.
- [70] C. Dietrich, K. Walter-Walsh, S. Preißler, G. O. Hofmann, O. W. Witte, W. H. Miltner, and T. Weiss, "Sensory feedback prosthesis reduces phantom limb pain: proof of a principle," *Neuroscience letters*, vol. 507, no. 2, pp. 97–100, 2012.
- [71] M. R. Mulvey, H. E. Radford, H. J. Fawcner, L. Hirst, V. Neumann, and M. I. Johnson, "Transcutaneous electrical nerve stimulation for phantom pain and stump pain in adult amputees," *Pain Practice*, vol. 13, no. 4, pp. 289–296, 2013.
- [72] P. Svensson, U. Wijk, A. Björkman, and C. Antfolk, "A review of invasive and non-invasive sensory feedback in upper limb prostheses," *Expert Review of Medical Devices*, no. just-accepted, 2017.
- [73] H. Yamada, Y. Yamanoi, K. Wakita, and R. Kato, "Investigation of a cognitive strain on hand grasping induced by sensory feedback for myoelectric hand," in *Robotics and Automation (ICRA), 2016 IEEE International Conference on*. IEEE, 2016, pp. 3549–3554.

- 
- [74] G. A. Tabot, J. F. Dammann, J. A. Berg, F. V. Tenore, J. L. Boback, R. J. Vogelstein, and S. J. Bensmaia, "Restoring the sense of touch with a prosthetic hand through a brain interface," *Proceedings of the National Academy of Sciences*, vol. 110, no. 45, pp. 18 279–18 284, 2013.
- [75] G. A. Tabot, S. S. Kim, J. E. Winberry, and S. J. Bensmaia, "Restoring tactile and proprioceptive sensation through a brain interface," *Neurobiology of disease*, vol. 83, pp. 191–198, 2015.
- [76] D. W. Tan, M. A. Schiefer, M. W. Keith, J. R. Anderson, J. Tyler, and D. J. Tyler, "A neural interface provides long-term stable natural touch perception," *Science translational medicine*, vol. 6, no. 257, pp. 257ra138–257ra138, 2014.
- [77] T. Davis, H. Wark, D. Hutchinson, D. Warren, K. O'Neill, T. Scheinblum, G. Clark, R. Normann, and B. Greger, "Restoring motor control and sensory feedback in people with upper extremity amputations using arrays of 96 microelectrodes implanted in the median and ulnar nerves," *Journal of neural engineering*, vol. 13, no. 3, p. 036001, 2016.
- [78] N. Lago, D. Ceballos, F. J. Rodriguez, T. Stieglitz, and X. Navarro, "Long term assessment of axonal regeneration through polyimide regenerative electrodes to interface the peripheral nerve," *Biomaterials*, vol. 26, no. 14, pp. 2021–2031, 2005.
- [79] W. Penfield and E. Boldrey, "Somatic motor and sensory representation in the cerebral cortex of man as studied by electrical stimulation," *Brain*, vol. 60, no. 4, pp. 389–443, 1937.
- [80] S. N. Flesher, J. L. Collinger, S. T. Foldes, J. M. Weiss, J. E. Downey, E. C. Tyler-Kabara, S. J. Bensmaia, A. B. Schwartz, M. L. Boninger, and R. A. Gaunt, "Intracortical microstimulation of human somatosensory cortex," *Science translational medicine*, vol. 8, no. 361, pp. 361ra141–361ra141, 2016.
- [81] M. Ortiz-Catalan, R. Brånemark, B. Håkansson, and J. Delbeke, "On the viability of implantable electrodes for the natural control of artificial limbs: review and discussion," *Biomedical engineering online*, vol. 11, no. 1, p. 33, 2012.
- [82] B. P. Christie, M. Freeberg, W. D. Mernberg, G. J. C. Pinault, H. A. Hoyen, D. J. Tyler, and R. J. Triolo, "“long-term stability of stimulating spiral nerve cuff electrodes on human peripheral nerves,”" vol. 14, p. 70. [Online]. Available: <https://doi.org/10.1186/s12984-017-0285-3>
- [83] D. J. Tyler and D. M. Durand, "Functionally selective peripheral nerve stimulation with a flat interface nerve electrode," *IEEE Transactions on Neural Systems and Rehabilitation Engineering*, vol. 10, no. 4, pp. 294–303, 2002.
- [84] T. A. Kuiken, A. E. S. Feuser, and A. K. Barlow, *Targeted muscle reinnervation: a neural interface for artificial limbs*. Taylor & Francis, 2013.

## Bibliography

---

- [85] K. Kim and J. E. Colgate, "Haptic feedback enhances grip force control of semg-controlled prosthetic hands in targeted reinnervation amputees," *IEEE Transactions on Neural Systems and Rehabilitation Engineering*, vol. 20, no. 6, pp. 798–805, 2012.
- [86] L. A. Miller, K. A. Stubblefield, R. D. Lipschutz, B. A. Lock, and T. A. Kuiken, "Improved myoelectric prosthesis control using targeted reinnervation surgery: a case series," *IEEE Transactions on Neural Systems and Rehabilitation Engineering*, vol. 16, no. 1, pp. 46–50, 2008.
- [87] T. A. Kuiken, G. Dumanian, R. Lipschutz, L. Miller, and K. Stubblefield, "The use of targeted muscle reinnervation for improved myoelectric prosthesis control in a bilateral shoulder disarticulation amputee," *Prosthetics and Orthotics International*, vol. 28, no. 3, pp. 245–253, 2004.
- [88] J. Gonzalez, H. Soma, M. Sekine, and W. Yu, "Psycho-physiological assessment of a prosthetic hand sensory feedback system based on an auditory display: a preliminary study," *Journal of neuroengineering and rehabilitation*, vol. 9, no. 1, p. 33, 2012.
- [89] S. Wilson and S. Dirven, "Audio sensory substitution for human-in-the-loop force feedback of upper limb prosthetics," in *Mechatronics and Machine Vision in Practice (M2VIP), 2016 23rd International Conference on.* IEEE, 2016, pp. 1–6.
- [90] G. Lundborg, B. Rosén, and S. Lindberg, "Hearing as substitution for sensation: a new principle for artificial sensibility," *The Journal of hand surgery*, vol. 24, no. 2, pp. 219–224, 1999.
- [91] J. González, W. Yu, and A. Hernandez Arieta, "Multichannel audio biofeedback for dynamical coupling between prosthetic hands and their users," *Industrial Robot: An International Journal*, vol. 37, no. 2, pp. 148–156, 2010.
- [92] D. S. Childress, "Closed-loop control in prosthetic systems: historical perspective," *Annals of biomedical engineering*, vol. 8, no. 4, pp. 293–303, 1980.
- [93] C. Antfolk, M. D'Alonzo, B. Rosen, G. Lundborg, F. Sebelius, and C. Cipriani, "Sensory feedback in upper limb prosthetics," *Expert review of medical devices*, vol. 10, no. 1, pp. 45–54, 2013.
- [94] J. S. Schofield, K. R. Evans, J. P. Carey, and J. S. Hebert, "Applications of sensory feedback in motorized upper extremity prosthesis: a review," *Expert review of medical devices*, vol. 11, no. 5, pp. 499–511, 2014.
- [95] S. G. Meek, S. C. Jacobsen, and P. P. Goulding, "Extended physiologic tacton: design and evaluation of a proportional force feedback system," *J Rehabil Res Dev*, vol. 26, no. 3, pp. 53–62, 1989.
- [96] E. Acoustics, "Engineering acoustics: C2 tacton," <https://www.eaiinfo.com/>, accessed: 2017-08-15.

- 
- [97] P. Microdrives, "Linear resonant actuators - LRAs," <https://www.precisionmicrodrives.com/vibration-motors/linear-resonant-actuators-lras>, accessed: 2017-08-15.
- [98] I. Poupyrev, S. Maruyama, and J. Rekimoto, "Ambient touch: designing tactile interfaces for handheld devices," in *Proceedings of the 15th annual ACM symposium on User interface software and technology*. ACM, 2002, pp. 51–60.
- [99] H. Taniguchi, "Flexible artificial muscle actuator using coiled shape memory alloy wires," *APCBEE Procedia*, vol. 7, pp. 54–59, 2013.
- [100] H. Sawada, "Tactile display using the micro-vibration of shape-memory alloy wires and its application to tactile interaction systems," in *Pervasive Haptics*. Springer, 2016, pp. 57–77.
- [101] P. E. Patterson and J. A. Katz, "Design and evaluation of a sensory feedback system that provides grasping pressure in a myoelectric hand," *J Rehabil Res Dev*, vol. 29, no. 1, pp. 1–8, 1992.
- [102] C. E. Stepp and Y. Matsuoka, "Vibrotactile sensory substitution for object manipulation: amplitude versus pulse train frequency modulation," *IEEE Transactions on Neural Systems and Rehabilitation Engineering*, vol. 20, no. 1, pp. 31–37, 2012.
- [103] C. Cipriani, M. D'Alonzo, and M. C. Carrozza, "A miniature vibrotactile sensory substitution device for multifingered hand prosthetics," *IEEE Transactions on Biomedical Engineering*, vol. 59, no. 2, pp. 400–408, 2012.
- [104] M. D'Alonzo and C. Cipriani, "Vibrotactile sensory substitution elicits feeling of ownership of an alien hand," *PloS one*, vol. 7, no. 11, p. e50756, 2012.
- [105] M. D'Alonzo, F. Clemente, and C. Cipriani, "Vibrotactile stimulation promotes embodiment of an alien hand in amputees with phantom sensations," *IEEE Transactions on Neural Systems and Rehabilitation Engineering*, vol. 23, no. 3, pp. 450–457, 2015.
- [106] A. Anani and L. Körner, "Discrimination of phantom hand sensations elicited by afferent electrical nerve stimulation in below-elbow amputees," *Medical progress through technology*, vol. 6, no. 3, pp. 131–135, 1979.
- [107] G. Shannon, "A myoelectrically-controlled prosthesis with sensory feedback," *Medical and Biological Engineering and Computing*, vol. 17, no. 1, pp. 73–80, 1979.
- [108] R. Scott, R. Brittain, R. Caldwell, A. Cameron, and V. Dunfield, "Sensory-feedback system compatible with myoelectric control," *Medical and Biological Engineering and Computing*, vol. 18, no. 1, pp. 65–69, 1980.
- [109] K. Choi, P. Kim, K.-S. Kim, and S. Kim, "Mixed-modality stimulation to evoke two modalities simultaneously in one channel for electrocutaneous sensory feedback," *IEEE Transactions on Neural Systems and Rehabilitation Engineering*, 2017.

## Bibliography

---

- [110] H. Kajimoto, "Electro-tactile display: principle and hardware," in *Pervasive Haptics*. Springer, 2016, pp. 79–96.
- [111] I. Saunders and S. Vijayakumar, "The role of feed-forward and feedback processes for closed-loop prosthesis control," *Journal of Neuroengineering and Rehabilitation*, vol. 8, no. 60, pp. 1–12, 2011.
- [112] M. D'Alonzo, S. Dosen, C. Cipriani, and D. Farina, "Hyve—hybrid vibro-electrotactile stimulation—is an efficient approach to multi-channel sensory feedback," *IEEE transactions on haptics*, vol. 7, no. 2, pp. 181–190, 2014.
- [113] H. Huang, T. Li, C. Bruschini, C. Enz, J. Justiz, C. Antfolk, and V. M. Koch, "Multi-modal sensory feedback system for upper limb amputees," in *CAS (NGCAS), 2017 New Generation of*. IEEE, 2017, pp. 193–196.
- [114] M. C. Jimenez and J. A. Fishel, "Evaluation of force, vibration and thermal tactile feedback in prosthetic limbs," in *Haptics Symposium (HAPTICS), 2014 IEEE*. IEEE, 2014, pp. 437–441.
- [115] H.-N. Ho and L. A. Jones, "Development and evaluation of a thermal display for material identification and discrimination," *ACM Transactions on Applied Perception (TAP)*, vol. 4, no. 2, p. 13, 2007.
- [116] Y. Ueda and C. Ishii, "Development of a feedback device of temperature sensation for a myoelectric prosthetic hand by using peltier element," in *2016 International Conference on Advanced Mechatronic Systems (ICAMechS)*. IEEE, 2016, pp. 488–493.
- [117] M. Nakatani, K. Sato, K. Sato, Y. Kawana, D. Takai, K. Minamizawa, and S. Tachi, "A novel multimodal tactile module that can provide vibro-thermal feedback," in *International AsiaHaptics conference*. Springer, 2016, pp. 437–443.
- [118] K. Kim, J. E. Colgate, and M. A. Peshkin, "On the design of a thermal display for upper extremity prosthetics," in *Haptic interfaces for virtual environment and teleoperator systems, 2008. haptics 2008. symposium on*. IEEE, 2008, pp. 413–419.
- [119] D. Simpson *et al.*, "The choice of control system for the multimovement prosthesis: extended physiological proprioception (epp)," *The control of upper-extremity prostheses and orthoses*, pp. 146–150, 1974.
- [120] T. Pistohl, D. Joshi, G. Ganesh, A. Jackson, and K. Nazarpour, "Artificial proprioceptive feedback for myoelectric control," *IEEE Transactions on Neural Systems and Rehabilitation Engineering*, vol. 23, no. 3, pp. 498–507, 2015.
- [121] P. Kapur, M. Jensen, L. J. Buxbaum, S. A. Jax, and K. J. Kuchenbecker, "Spatially distributed tactile feedback for kinesthetic motion guidance," in *Haptics Symposium, 2010 IEEE*. IEEE, 2010, pp. 519–526.

- 
- [122] H. J. Witteveen, H. S. Rietman, and P. H. Veltink, "Vibrotactile grasping force and hand aperture feedback for myoelectric forearm prosthesis users," *Prosthetics and orthotics international*, vol. 39, no. 3, pp. 204–212, 2015.
- [123] K. Bark, J. W. Wheeler, S. Premakumar, and M. R. Cutkosky, "Comparison of skin stretch and vibrotactile stimulation for feedback of proprioceptive information," in *Haptic interfaces for virtual environment and teleoperator systems, 2008. haptics 2008. symposium on*. IEEE, 2008, pp. 71–78.
- [124] M. Mulas, M. Folgheraiter, and G. Gini, "An emg-controlled exoskeleton for hand rehabilitation," in *Rehabilitation Robotics, 2005. ICORR 2005. 9th International Conference on*. IEEE, 2005, pp. 371–374.
- [125] H. Woodford and C. Price, "Emg biofeedback for the recovery of motor function after stroke," *Cochrane Database Syst Rev*, vol. 2, 2004.
- [126] Y. H. Yin, Y. J. Fan, and L. D. Xu, "Emg and epp-integrated human-machine interface between the paralyzed and rehabilitation exoskeleton," *IEEE Transactions on Information Technology in Biomedicine*, vol. 16, no. 4, pp. 542–549, 2012.
- [127] J.-S. Han, Z. Z. Bien, D.-J. Kim, H.-E. Lee, and J.-S. Kim, "Human-machine interface for wheelchair control with emg and its evaluation," in *Engineering in Medicine and Biology Society, 2003. Proceedings of the 25th Annual International Conference of the IEEE*, vol. 2. IEEE, 2003, pp. 1602–1605.
- [128] L. Padua, I. Aprile, M. L. Monaco, L. Fenicia, F. Anniballi, F. Pauri, and P. Tonali, "Neurophysiological assessment in the diagnosis of botulism: Usefulness of single-fiber emg," *Muscle & nerve*, vol. 22, no. 10, pp. 1388–1392, 1999.
- [129] S. Kumar and A. Mital, *Electromyography in ergonomics*. CRC Press, 1996.
- [130] G. N. Saridis and T. P. Gootee, "Emg pattern analysis and classification for a prosthetic arm," *IEEE Transactions on Biomedical Engineering*, no. 6, pp. 403–412, 1982.
- [131] D. Graupe and W. K. Cline, "Functional separation of emg signals via arma identification methods for prosthesis control purposes," *IEEE Transactions on Systems, Man, and Cybernetics*, no. 2, pp. 252–259, 1975.
- [132] N. Hogan, "A review of the methods of processing emg for use as a proportional control signal," *Biomedical engineering*, vol. 11, no. 3, pp. 81–86, 1976.
- [133] D. Childress, "Upper-limb prosthetics: control of limb prostheses," *American Academy of Orthopaedic Surgeons. Atlas of limb prosthetics: surgical, prosthetics, and rehabilitation principles. 2nd edition*. St. Louis: Mosby-Year Book, pp. 175–198, 1992.
- [134] M. Z. Jamal, "Signal acquisition using surface emg and circuit design considerations for robotic prosthesis," in *Computational Intelligence in Electromyography Analysis-A Perspective on Current Applications and Future Challenges*. InTech, 2012.

## Bibliography

---

- [135] G. R. Kanitz, C. Antfolk, C. Cipriani, F. Sebelius, and M. C. Carrozza, "Decoding of individuated finger movements using surface emg and input optimization applying a genetic algorithm," in *Engineering in Medicine and Biology Society, EMBC, 2011 Annual International Conference of the IEEE*. IEEE, 2011, pp. 1608–1611.
- [136] M. Zardoshti-Kermani, B. C. Wheeler, K. Badie, and R. M. Hashemi, "Emg feature evaluation for movement control of upper extremity prostheses," *IEEE Transactions on Rehabilitation Engineering*, vol. 3, no. 4, pp. 324–333, 1995.
- [137] Y. Huang, K. B. Englehart, B. Hudgins, and A. D. Chan, "A gaussian mixture model based classification scheme for myoelectric control of powered upper limb prostheses," *IEEE Transactions on Biomedical Engineering*, vol. 52, no. 11, pp. 1801–1811, 2005.
- [138] S. Ferguson and G. R. Dunlop, "Grasp recognition from myoelectric signals," in *Proceedings of the Australasian Conference on Robotics and Automation, Auckland, New Zealand*, vol. 1, 2002.
- [139] M.-F. Lucas, A. Gaufriau, S. Pascual, C. Doncarli, and D. Farina, "Multi-channel surface emg classification using support vector machines and signal-based wavelet optimization," *Biomedical Signal Processing and Control*, vol. 3, no. 2, pp. 169–174, 2008.
- [140] S. Bitzer and P. Van Der Smagt, "Learning emg control of a robotic hand: towards active prostheses," in *Proceedings 2006 IEEE International Conference on Robotics and Automation, 2006. ICRA 2006*. IEEE, 2006, pp. 2819–2823.
- [141] A. J. Young, L. H. Smith, E. J. Rouse, and L. J. Hargrove, "Classification of simultaneous movements using surface emg pattern recognition," *IEEE Transactions on Biomedical Engineering*, vol. 60, no. 5, pp. 1250–1258, 2013.
- [142] A. Alkan and M. Günay, "Identification of emg signals using discriminant analysis and svm classifier," *Expert Systems with Applications*, vol. 39, no. 1, pp. 44–47, 2012.
- [143] C. Cipriani, C. Antfolk, M. Controzzi, G. Lundborg, B. Rosen, M. C. Carrozza, and F. Sebelius, "Online myoelectric control of a dexterous hand prosthesis by transradial amputees," *IEEE Transactions on Neural Systems and Rehabilitation Engineering*, vol. 19, no. 3, pp. 260–70, 2011.
- [144] C. Antfolk, C. Cipriani, M. Controzzi, M. C. Carrozza, G. Lundborg, B. Rosen, and F. Sebelius, "Using EMG for Real-time Prediction of Joint Angles to Control a Prosthetic Hand Equipped with a Sensory Feedback System," *Journal of Medical and Biological Engineering*, vol. 30, no. 6, SI, pp. 399–405, 2010.
- [145] K. Englehart and B. Hudgins, "A robust, real-time control scheme for multifunction myoelectric control," *IEEE transactions on biomedical engineering*, vol. 50, no. 7, pp. 848–854, 2003.

- 
- [146] H. Xu, C. Caramanis, and S. Mannor, "Robustness and regularization of support vector machines," *Journal of Machine Learning Research*, vol. 10, no. Jul, pp. 1485–1510, 2009.
- [147] S. Balakrishnama and A. Ganapathiraju, "Linear discriminant analysis-a brief tutorial," *Institute for Signal and information Processing*, vol. 18, 1998.
- [148] C. M. Bishop, *Pattern Recognition and Machine Learning*. New York, USA: Springer, 2006.
- [149] P. Bartlett and J. Shawe-Taylor, "Generalization performance of support vector machines and other pattern classifiers," *Advances in Kernel methods—support vector learning*, pp. 43–54, 1999.
- [150] S.-i. Amari and S. Wu, "Improving support vector machine classifiers by modifying kernel functions," *Neural Networks*, vol. 12, no. 6, pp. 783–789, 1999.
- [151] G. E. Hinton, "Deep belief networks," *Scholarpedia*, vol. 4, no. 5, p. 5947, 2009.
- [152] M. Sabzevar, M. GhasemiGol, M. Naghibzadeh, and H. Sadoghi Yazdi, "Improved dag svm: a new method for multi-class svm classification," in *Int. Conf. Artificial Intelligence ICAI 2009*, 2009.
- [153] R. Rifkin and A. Klautau, "In defense of one-vs-all classification," *Journal of machine learning research*, vol. 5, no. Jan, pp. 101–141, 2004.
- [154] M. Pal and P. Mather, "Support vector machines for classification in remote sensing," *International Journal of Remote Sensing*, vol. 26, no. 5, pp. 1007–1011, 2005.
- [155] J. C. Platt, N. Cristianini, and J. Shawe-Taylor, "Large margin dags for multiclass classification," in *Advances in neural information processing systems*, 2000, pp. 547–553.
- [156] S. Cheong, S. H. Oh, and S.-Y. Lee, "Support vector machines with binary tree architecture for multi-class classification," *Neural Information Processing-Letters and Reviews*, vol. 2, no. 3, pp. 47–51, 2004.
- [157] Y. Du, W. Jin, W. Wei, Y. Hu, and W. Geng, "Surface EMG-based inter-session gesture recognition enhanced by deep domain adaptation," *Sensors*, vol. 17, no. 3, p. 458, 2017.
- [158] A. D. Chan and G. C. Green, "Myoelectric control development toolbox," *CMBES Proceedings*, vol. 30, no. 1, 2017.
- [159] W. Geng, Y. Du, W. Jin, W. Wei, Y. Hu, and J. Li, "Gesture recognition by instantaneous surface emg images," *Scientific reports*, vol. 6, p. 36571, 2016.
- [160] S. Shin, R. Tafreshi, and R. Langari, "A performance comparison of hand motion emg classification," in *Biomedical engineering (mechme), 2014 middle east conference on*. IEEE, 2014, pp. 353–356.

## Bibliography

---

- [161] G. Wu and E. Y. Chang, "Adaptive feature-space conformal transformation for imbalanced-data learning," in *Proceedings of the 20th International Conference on Machine Learning (ICML-03)*, 2003, pp. 816–823.
- [162] A. Björkman, A. Weibull, J. Olsrud, H. Henrik Ehrsson, B. Rosén, and I. M. Björkman-Burtscher, "Phantom digit somatotopy: a functional magnetic resonance imaging study in forearm amputees," *European Journal of Neuroscience*, vol. 36, no. 1, pp. 2098–2106, 2012.
- [163] P. W. Halligan, J. C. Marshall, D. T. Wade, J. Davey, and D. Morrison, "Thumb in cheek? sensory reorganization and perceptual plasticity after limb amputation." *Neuroreport*, vol. 4, no. 3, pp. 233–236, 1993.
- [164] V. S. Ramachandran and W. Hirstein, "The perception of phantom limbs. the do hebb lecture." *Brain*, vol. 121, no. 9, pp. 1603–1630, 1998.
- [165] A. Woodhouse, "Phantom limb sensation," *Clinical and experimental pharmacology and physiology*, vol. 32, no. 1-2, pp. 132–134, 2005.
- [166] C. M. Kooijman, P. U. Dijkstra, J. H. Geertzen, A. Elzinga, and C. P. van der Schans, "Phantom pain and phantom sensations in upper limb amputees: an epidemiological study," *Pain*, vol. 87, no. 1, pp. 33–41, 2000.
- [167] P. Carlen, P. Wall, H. Nadvorna, and T. Steinbach, "Phantom limbs and related phenomena in recent traumatic amputations," *Neurology*, vol. 28, no. 3, pp. 211–211, 1978.
- [168] D. Zhang, H. Xu, P. B. Shull, J. Liu, and X. Zhu, "Somatotopical feedback versus non-somatotopical feedback for phantom digit sensation on amputees using electrotactile stimulation," *Journal of neuroengineering and rehabilitation*, vol. 12, no. 1, p. 44, 2015.
- [169] C. Antfolk, M. D'Alonzo, M. Controzzi, G. Lundborg, B. Rosén, F. Sebelius, and C. Cipriani, "Artificial redirection of sensation from prosthetic fingers to the phantom hand map on transradial amputees: vibrotactile versus mechanotactile sensory feedback," *IEEE transactions on neural systems and rehabilitation engineering*, vol. 21, no. 1, pp. 112–120, 2013.
- [170] C. Antfolk, A. Björkman, S.-O. Frank, F. Sebelius, G. Lundborg, and B. Rosen, "Sensory feedback from a prosthetic hand based on air-mediated pressure from the hand to the forearm skin," *Journal of rehabilitation medicine*, vol. 44, no. 8, pp. 702–707, 2012.
- [171] L. G. Cohen, S. Bandinelli, T. W. Findley, and M. Hallett, "Motor reorganization after upper limb amputation in man," *Brain*, vol. 114, no. 1, pp. 615–627, 1991.
- [172] W. Penfield and T. Rasmussen, *The cerebral cortex of man; a clinical study of localization of function*. Macmillan, 1950.

- 
- [173] A. Pirowska, T. Wloch, R. Nowobilski, M. Plaszewski, A. Hocini, and D. Ménager, “Phantom phenomena and body scheme after limb amputation: A literature review,” *Neurologia i Neurochirurgia Polska*, vol. 48, no. 1, pp. 52–59, Jan. 2014.
- [174] M. Kass, A. Witkin, and D. Terzopoulos, “Snakes: Active contour models,” *International Journal of Computer Vision*, vol. 1, no. 4, pp. 321–331, 1988.
- [175] L. Schmalzl, E. Thomke, C. Ragnö, M. Nilseryd, A. Stockselius, and H. H. Ehrsson, ““pulling telescoped phantoms out of the stump”: Manipulating the perceived position of phantom limbs using a full-body illusion,” *Frontiers in human neuroscience*, vol. 5, 2011.
- [176] G. Chai, X. Sui, S. Li, L. He, and N. Lan, “Characterization of evoked tactile sensation in forearm amputees with transcutaneous electrical nerve stimulation,” *Journal of neural engineering*, vol. 12, no. 6, p. 066002, 2015.
- [177] A. Björkman, U. Wijk, C. Antfolk, I. Björkman-Burtscher, and B. Rosén, “Sensory qualities of the phantom hand map in the residual forearm of amputees,” *Journal of rehabilitation medicine*, vol. 48, no. 4, pp. 365–370, 2016.
- [178] Y.-L. Boureau, J. Ponce, and Y. LeCun, “A theoretical analysis of feature pooling in visual recognition,” in *Proceedings of the 27th International Conference on Machine Learning (ICML-10)*, 2010, pp. 111–118.
- [179] Z. Wu, H. Zhang, and J. Liu, “A fuzzy support vector machine algorithm for classification based on a novel PIM fuzzy clustering method,” *Neurocomputing*, vol. 125, pp. 119–124, 2014.
- [180] C.-F. Lin and S.-D. Wang, “Fuzzy support vector machines,” *IEEE Transactions on Neural Networks*, vol. 13, no. 2, pp. 464–471, 2002.
- [181] A. Calma, T. Reitmaier, B. Sick, P. Lukowicz, and M. Embrechts, “A new vision of collaborative active learning,” *arXiv preprint arXiv:1504.00284*, 2015.
- [182] D. Tuia, M. Volpi, L. Copa, M. Kanevski, and J. Munoz-Mari, “A survey of active learning algorithms for supervised remote sensing image classification,” *IEEE Journal of Selected Topics in Signal Processing*, vol. 5, no. 3, pp. 606–617, 2011.
- [183] K. Brinker, “Incorporating diversity in active learning with support vector machines,” in *ICML*, vol. 3, 2003, pp. 59–66.
- [184] B. Demir, C. Persello, and L. Bruzzone, “Batch-mode active-learning methods for the interactive classification of remote sensing images,” *IEEE Transactions on Geoscience and Remote Sensing*, vol. 49, no. 3, pp. 1014–1031, 2011.
- [185] T. Li, H. Huang, J. Justiz, and V. M. Koch, “A miniature multimodal actuator for effective tactile feedback: Design and characterization,” *Procedia Engineering*, vol. 168, pp. 1547–1550, 2016.

## Bibliography

---

- [186] S. Abe and T. Inoue, "Fuzzy support vector machines for multiclass problems." in *ESANN*, 2002, pp. 113–118.
- [187] T. Inoue and S. Abe, "Fuzzy support vector machines for pattern classification," in *International Joint Conference on Neural Networks, 2001. IJCNN'01.*, vol. 2. IEEE, 2001, pp. 1449–1454.
- [188] K. S. Hale and K. M. Stanney, "Deriving haptic design guidelines from human physiological, psychophysical, and neurological foundations," *IEEE computer graphics and applications*, vol. 24, no. 2, pp. 33–39, 2004.
- [189] V. G. Chouvardas, A. N. Miliou, and M. K. Hatalis, "Tactile display applications: A state of the art survey," in *Proceedings of the 2nd Balkan Conference in Informatics*. Citeseer, 2005, pp. 290–303.
- [190] L. A. Jones and N. B. Sarter, "Tactile displays: Guidance for their design and application," *Human factors*, vol. 50, no. 1, pp. 90–111, 2008.
- [191] S. Choi and K. Kuchenbecker, "Vibrotactile display: Perception, technology, and applications," *Proceedings of the IEEE*, vol. 101, no. 9, pp. 2093–2104, Sep. 2013.
- [192] T. G. Wilson, "Advancement of technology and its impact on urologists: release of the da vinci xi, a new surgical robot," *European urology*, vol. 66, no. 5, pp. 793–794, 2014.
- [193] J. B. Van Erp, H. A. Van Veen, C. Jansen, and T. Dobbins, "Waypoint navigation with a vibrotactile waist belt," *ACM Transactions on Applied Perception (TAP)*, vol. 2, no. 2, pp. 106–117, 2005.
- [194] "Steam controller," <http://store.steampowered.com/app/353370/>, accessed: 2016-10-13.
- [195] T. Iwamoto, M. Tatezono, T. Hoshi, and H. Shinoda, "Airborne ultrasound tactile display," in *ACM SIGGRAPH 2008 new tech demos*. ACM, 2008, p. 1.
- [196] "NullSpace VR," <http://nullspacevr.com/>, accessed: 2016-10-13.
- [197] I. S. MacKenzie and A. Oniszczak, "The tactile touchpad," in *CHI'97 Extended Abstracts on Human Factors in Computing Systems*. ACM, 1997, pp. 309–310.
- [198] V. G. Chouvardas, A. N. Miliou, and M. K. Hatalis, "Tactile displays: Overview and recent advances," *Displays*, vol. 29, no. 3, pp. 185–194, 2008.
- [199] C. Ramstein, "Combining haptic and braille technologies: design issues and pilot study," in *Proceedings of the second annual ACM conference on Assistive technologies*. ACM, 1996, pp. 37–44.
- [200] H.-C. Cho, B.-S. Kim, J.-J. Park, and J.-B. Song, "Development of a braille display using piezoelectric linear motors," in *SICE-ICASE, 2006. International Joint Conference*. IEEE, 2006, pp. 1917–1921.

- 
- [201] C. Ho, H. Z. Tan, and C. Spence, "Using spatial vibrotactile cues to direct visual attention in driving scenes," *Transportation Research Part F: Traffic Psychology and Behaviour*, vol. 8, no. 6, pp. 397–412, 2005.
- [202] J. B. Van Erp and H. A. Van Veen, "Vibrotactile in-vehicle navigation system," *Transportation Research Part F: Traffic Psychology and Behaviour*, vol. 7, no. 4, pp. 247–256, 2004.
- [203] B. D. Nordwall, "Vest enables pilots to feel aircraft attitude," *Aviation Week & Space Technology*, vol. 152, no. 17, p. 69, 2000.
- [204] I. R. Summers, P. G. Cooper, P. Wright, D. A. Gratton, P. Milnes, and B. H. Brown, "Information from time-varying vibrotactile stimuli," *The Journal of the Acoustical Society of America*, vol. 102, no. 6, pp. 3686–3696, 1997.
- [205] M. Rothenberg, R. T. Verrillo, S. A. Zahorian, M. L. Brachman, and S. J. Bolanowski Jr, "Vibrotactile frequency for encoding a speech parameter," *The Journal of the Acoustical Society of America*, vol. 62, no. 4, pp. 1003–1012, 1977.
- [206] M. Tommerdahl, K. Hester, E. Felix, M. Hollins, O. V. Favorov, P. Quibrera, and B. Whitsel, "Human vibrotactile frequency discriminative capacity after adaptation to 25 hz or 200 hz stimulation," *Brain research*, vol. 1057, no. 1, pp. 1–9, 2005.
- [207] H. Pongrac, "Vibrotactile perception: Differential effects of frequency, amplitude, and acceleration," in *2006 IEEE International Workshop on Haptic Audio Visual Environments and their Applications (HAVE 2006)*. IEEE, 2006, pp. 54–59.
- [208] —, "Vibrotactile perception: examining the coding of vibrations and the just noticeable difference under various conditions," *Multimedia systems*, vol. 13, no. 4, pp. 297–307, 2008.
- [209] H. Tang and D. J. Beebe, "Design and microfabrication of a flexible oral electrotactile display," *Journal Of Microelectromechanical Systems*, vol. 12, no. 1, pp. 29–36, 2003.
- [210] H. Kajimoto, N. Kawakami, S. Tachi, and M. Inami, "Smarttouch: Electric skin to touch the untouchable," *IEEE computer graphics and applications*, vol. 24, no. 1, pp. 36–43, 2004.
- [211] M. Bergamasco, A. A. Alessi, and M. Calcara, "Thermal feedback in virtual environments," *Presence: Teleoperators and Virtual Environments*, vol. 6, no. 6, pp. 617–629, 1997.
- [212] M. Ottensmeyer and J. K. Salisbury, "Hot and cold running vr: adding thermal stimuli to the haptic experience," *Proceedings of the PHANToM Users Group*, 1997.
- [213] G. Wilson, M. Halvey, S. A. Brewster, and S. A. Hughes, "Some like it hot: thermal feedback for mobile devices," in *Proceedings of the SIGCHI Conference on Human Factors in Computing Systems*. ACM, 2011, pp. 2555–2564.

## Bibliography

---

- [214] L. A. Jones and M. Berris, "Material discrimination and thermal perception," in *11th Symposium on Haptic Interfaces for Virtual Environment and Teleoperator Systems, 2003. HAPTICS 2003. Proceedings.* IEEE, 2003, pp. 171–178.
- [215] G. J. Monkman and P. Taylor, "Thermal tactile sensing," *IEEE Transactions on Robotics and Automation*, vol. 9, no. 3, pp. 313–318, 1993.
- [216] J. C. Baird and E. J. Noma, *Fundamentals of scaling and psychophysics.* John Wiley & Sons, 1978.
- [217] L. A. Jones and H. Z. Tan, "Application of psychophysical techniques to haptic research," *IEEE transactions on haptics*, vol. 6, no. 3, pp. 268–284, 2013.
- [218] A. M. Colman, *A dictionary of psychology.* Oxford University Press, USA, 2015.
- [219] K. O. Johnson and J. R. Phillips, "Tactile spatial resolution. i. two-point discrimination, gap detection, grating resolution, and letter recognition," *Journal of neurophysiology*, vol. 46, no. 6, pp. 1177–1192, 1981.
- [220] O. M. JonathanTong and D. Goldreich, "Two-point orientation discrimination versus the traditional two-point test for tactile spatial acuity assessment," 2013.
- [221] N. A. Macmillan and C. D. Creelman, *Detection theory: A user's guide.* Psychology press, 2004.
- [222] E. H. Weber, *The sense of touch.* Academic Press for Experimental Psychology Society, 1978.
- [223] R. W. Cholewiak and A. A. Collins, "Vibrotactile localization on the arm: Effects of place, space, and age," *Perception & psychophysics*, vol. 65, no. 7, pp. 1058–1077, 2003.
- [224] R. W. Cholewiak, J. C. Brill, and A. Schwab, "Vibrotactile localization on the abdomen: Effects of place and space," *Perception & Psychophysics*, vol. 66, no. 6, pp. 970–987, 2004.
- [225] L. A. Jones, J. Kunkel, and E. Piatetski, "Vibrotactile pattern recognition on the arm and back," *Perception*, vol. 38, no. 1, pp. 52–68, 2009.
- [226] J. Biggs and M. A. Srinivasan, "Tangential versus normal displacements of skin: Relative effectiveness for producing tactile sensations," in *Haptic Interfaces for Virtual Environment and Teleoperator Systems, 2002. HAPTICS 2002. Proceedings. 10th Symposium on.* IEEE, 2002, pp. 121–128.
- [227] P. Microdrives, "Eccentric rotating masses - ERMs," <https://www.precisionmicrodrives.com/vibration-motors/eccentric-rotating-masses-erms>, accessed: 2017-08-15.
- [228] J. Raisamo, "TACTILE SENSING & FEEDBACK," University Lecture, 2007.
- [229] S. Stevens, "On the psychophysical law," *Psychological Review*, vol. 64, no. 3, pp. 153–181, 1957.

- 
- [230] O. Franzén and J. Nordmark, "Vibrotactile frequency discrimination," *Perception & Psychophysics*, vol. 17, no. 5, pp. 480–484, 1975.
- [231] D. Mahns, N. Perkins, V. Sahai, L. Robinson, and M. Rowe, "Vibrotactile frequency discrimination in human hairy skin," *Journal of Neurophysiology*, vol. 95, no. 3, pp. 1442–1450, 2006.
- [232] K. O. Sofia and L. Jones, "Mechanical and psychophysical studies of surface wave propagation during vibrotactile stimulation," *IEEE transactions on haptics*, vol. 6, no. 3, pp. 320–329, 2013.
- [233] R. W. Cholewiak, A. A. Collins, and J. C. Brill, "Spatial factors in vibrotactile pattern perception," in *Proceedings of Eurohaptics*, 2001, pp. 41–47.
- [234] H. von Gierke, E. Franke, and H. Oestreicher, "The propagation velocity of surface waves over the human body," *The Journal of the Acoustical Society of America*, vol. 26, no. 5, pp. 943–943, 1954.
- [235] V. Hayward, "A brief taxonomy of tactile illusions and demonstrations that can be done in a hardware store," *Brain research bulletin*, vol. 75, no. 6, pp. 742–752, 2008.
- [236] F. Vega-Bermudez and K. Johnson, "Surround suppression in the responses of primate sa1 and ra mechanoreceptive afferents mapped with a probe array," *Journal of neurophysiology*, vol. 81, no. 6, pp. 2711–2719, 1999.
- [237] M. Wickremaratchi and J. Llewelyn, "Effects of ageing on touch," *Postgraduate medical journal*, vol. 82, no. 967, pp. 301–304, 2006.
- [238] R. T. Verrillo, "Age related changes in the sensitivity to vibration," *Journal of Gerontology*, vol. 35, no. 2, pp. 185–193, 1980.
- [239] M. Stuart, A. B. Turman, J. Shaw, N. Walsh, and V. Nguyen, "Effects of aging on vibration detection thresholds at various body regions," *BMC Geriatrics*, vol. 3, no. 1, p. 1, 2003.
- [240] G. Gescheider, S. Bolanowski, K. Hall, K. Hoffman, and R. Verrillo, "The effects of aging on information-processing channels in the sense of touch: I. absolute sensitivity," *Somatosensory & motor research*, vol. 11, no. 4, pp. 345–357, 1994.
- [241] R. T. Verrillo, "Comparison of vibrotactile threshold and suprathreshold responses in men and women," *Perception & Psychophysics*, vol. 26, no. 1, pp. 20–24, 1979.
- [242] M. Bikah, M. S. Hallbeck, and J. H. Flowers, "Supracutaneous vibrotactile perception threshold at various non-glabrous body loci," *Ergonomics*, vol. 51, no. 6, pp. 920–934, 2008.
- [243] P. G. Wiles, S. M. Pearce, P. J. S. Rice, and J. M. O. Mitchell, "Vibration perception threshold: Influence of age, height, sex, and smoking, and calculation of accurate centile values," *Diabetic Medicine*, vol. 8, no. 2, pp. 157–161, 1991.

## Bibliography

---

- [244] R. T. Verrillo, "Effect of contactor area on the vibrotactile threshold," *The Journal of the Acoustical Society of America*, vol. 35, no. 12, pp. 1962–1966, 1963.
- [245] G. A. Gescheider, J. H. Wright, and R. T. Verrillo, *Information-processing channels in the tactile sensory system: A psychophysical and physiological analysis*. Psychology Press, 2010.
- [246] G. A. Gescheider, S. J. Bolanowski, J. V. Pope, and R. T. Verrillo, "A four-channel analysis of the tactile sensitivity of the fingertip: frequency selectivity, spatial summation, and temporal summation," *Somatosensory & motor research*, vol. 19, no. 2, pp. 114–124, 2002.
- [247] A. Gescheider, S. J. Bolanowski, and K. R. Hardick, "The frequency selectivity of information-processing channels in the tactile sensory system," *Somatosensory & Motor Research*, vol. 18, no. 3, pp. 191–201, 2001.
- [248] B. G. Green, "The effect of skin temperature on vibrotactile sensitivity," *Perception & Psychophysics*, vol. 21, no. 3, pp. 243–248, 1977.
- [249] S. Bolanowski and R. Verrillo, "Temperature and criterion effects in a somatosensory subsystem: a neurophysiological and psychophysical study," *Journal of Neurophysiology*, vol. 48, no. 3, pp. 836–855, 1982.
- [250] D. G. Caldwell and C. Gosney, "Enhanced tactile feedback (tele-taction) using a multi-functional sensory system," in *Robotics and Automation, 1993. Proceedings., 1993 IEEE International Conference on*. IEEE, 1993, pp. 955–960.
- [251] *BMS Sub-Micro Servo*, Blue Bird, Inc., 3 2018. [Online]. Available: <https://servodatabase.com/servo/blue-bird/bms-303>
- [252] H. Z. Tan, C. M. Reed, and N. I. Durlach, "Optimum information transfer rates for communication through haptic and other sensory modalities," *IEEE Transactions on Haptics*, vol. 3, no. 2, pp. 98–108, 2010.
- [253] H. Yousef, M. Boukallel, and K. Althoefer, "Tactile sensing for dexterous in-hand manipulation in robotics—a review," *Sensors and Actuators A: physical*, vol. 167, no. 2, pp. 171–187, 2011.
- [254] J. Tegin and J. Wikander, "Tactile sensing in intelligent robotic manipulation—a review," *Industrial Robot: An International Journal*, vol. 32, no. 1, pp. 64–70, 2005.
- [255] P. Puangmali, K. Althoefer, L. D. Seneviratne, D. Murphy, and P. Dasgupta, "State-of-the-art in force and tactile sensing for minimally invasive surgery," *IEEE Sensors Journal*, vol. 8, no. 4, pp. 371–381, 2008.
- [256] L. Zhang, F. Ju, Y. Cao, Y. Wang, and B. Chen, "A tactile sensor for measuring hardness of soft tissue with applications to minimally invasive surgery," *Sensors and Actuators A: Physical*, vol. 266, pp. 197–204, 2017.

- 
- [257] M. Eltaib and J. Hewit, "Tactile sensing technology for minimal access surgery—a review," *Mechatronics*, vol. 13, no. 10, pp. 1163–1177, 2003.
- [258] L. D. Harmon, "Automated tactile sensing," *The International Journal of Robotics Research*, vol. 1, no. 2, pp. 3–32, 1982.
- [259] G. Gale, "Automatic height control of a stripper harvester using a tactile sensor to detect the crop," *Journal of agricultural engineering research*, vol. 61, no. 4, pp. 217–226, 1995.
- [260] R. Stone and P. Brett, "A sensing technique for the measurement of tactile forces in the gripping of dough-like materials," *Proceedings of the Institution of Mechanical Engineers, Part B: Journal of Engineering Manufacture*, vol. 210, no. 3, pp. 261–269, 1996.
- [261] G. Mattiazzo, S. Mauro, T. Raparelli, and M. Velardocchia, "A fuzzy controlled pneumatic gripper for asparagus harvesting," in *Intelligent Components and Instruments for Control Applications 1994*. Elsevier, 1994, pp. 119–124.
- [262] S. Yamamoto, O. Nakao, and H. Nishimura, "Touch mode capacitive pressure sensor for passive tire monitoring system," in *Sensors, 2002. Proceedings of IEEE*, vol. 2. IEEE, 2002, pp. 1582–1586.
- [263] G. B. Langford, C. A. Montano, D. Odom, T. Danielson, R. Allen, G. Putnam, D. Beck *et al.*, "System for measuring parameters related to automobile seat," 2000, uS Patent 6,015,163.
- [264] M. Asadnia, A. G. P. Kottapalli, Z. Shen, J. Miao, and M. Triantafyllou, "Flexible and surface-mountable piezoelectric sensor arrays for underwater sensing in marine vehicles," *IEEE Sensors Journal*, vol. 13, no. 10, pp. 3918–3925, 2013.
- [265] W. Hu, X. Niu, R. Zhao, and Q. Pei, "Elastomeric transparent capacitive sensors based on an interpenetrating composite of silver nanowires and polyurethane," *Applied Physics Letters*, vol. 102, no. 8, p. 38, 2013.
- [266] J. Zimmerman and J. A. Martino, "Touch-screen image scrolling system and method," Feb. 10 2004, uS Patent 6,690,387.
- [267] M. C. Carrozza, F. Vecchi, F. Sebastiani, G. Cappiello, S. Roccella, M. Zecca, R. Lazzarini, and P. Dario, "Experimental analysis of an innovative prosthetic hand with proprioceptive sensors," in *Robotics and Automation, 2003. Proceedings. ICRA'03. IEEE International Conference on*, vol. 2. IEEE, 2003, pp. 2230–2235.
- [268] M. C. Carrozza, P. Dario, F. Vecchi, S. Roccella, M. Zecca, and F. Sebastiani, "The cyber-hand: on the design of a cybernetic prosthetic hand intended to be interfaced to the peripheral nervous system," in *IEEE/RSJ International Conference on Intelligent Robots and Systems, 2003.(IROS 2003). Proceedings. 2003*, vol. 3. IEEE, 2003, pp. 2642–2647.

## Bibliography

---

- [269] M. I. Tiwana, S. J. Redmond, and N. H. Lovell, "A review of tactile sensing technologies with applications in biomedical engineering," *Sensors and Actuators A: physical*, vol. 179, pp. 17–31, 2012.
- [270] I. Gaiser, S. Schulz, A. Kargov, H. Klosek, A. Bierbaum, C. Pylatiuk, R. Oberle, T. Werner, T. Asfour, G. Bretthauer *et al.*, "A new anthropomorphic robotic hand," in *Humanoid Robots, 2008. Humanoids 2008. 8th IEEE-RAS International Conference on*. IEEE, 2008, pp. 418–422.
- [271] K. Andrianesis and A. Tzes, "Development and control of a multifunctional prosthetic hand with shape memory alloy actuators," *Journal of Intelligent & Robotic Systems*, vol. 78, no. 2, p. 257, 2015.
- [272] M. V. Weghe, M. Rogers, M. Weissert, and Y. Matsuoka, "The act hand: Design of the skeletal structure," in *Robotics and Automation, 2004. Proceedings. ICRA'04. 2004 IEEE International Conference on*, vol. 4. IEEE, 2004, pp. 3375–3379.
- [273] P. J. Kyberd, O. E. Holland, P. H. Chappell, S. Smith, R. Tregidgo, P. J. Bagwell, and M. Snaith, "Marcus: A two degree of freedom hand prosthesis with hierarchical grip control," *IEEE Transactions on Rehabilitation Engineering*, vol. 3, no. 1, pp. 70–76, 1995.
- [274] S. Schulz, C. Pylatiuk, and G. Bretthauer, "A new ultralight anthropomorphic hand," in *Robotics and Automation, 2001. Proceedings 2001 ICRA. IEEE International Conference on*, vol. 3. IEEE, 2001, pp. 2437–2441.
- [275] H. Sugiuchi, S. Watanabe, Y. Hasegawa, and M. Nornoto, "A control system for multi-fingered robotic hand with distributed touch sensor," in *Industrial Electronics Society, 2000. IECON 2000. 26th Annual Conference of the IEEE*, vol. 1. IEEE, 2000, pp. 434–439.
- [276] Y. Kamikawa and T. Maeno, "Underactuated five-finger prosthetic hand inspired by grasping force distribution of humans," in *Intelligent Robots and Systems, 2008. IROS 2008. IEEE/RSJ International Conference on*. IEEE, 2008, pp. 717–722.
- [277] C. Cipriani, M. Controzzi, and M. C. Carrozza, "The smarthand transradial prosthesis," *Journal of neuroengineering and rehabilitation*, vol. 8, no. 1, p. 29, 2011.
- [278] T. Maeno and T. Hino, "Miniature five-fingered robot hand driven by shape memory alloy actuators," in *Proceedings of the 12th IASTED International Conference on Robotics and Applications*, 2006, pp. 174–179.
- [279] D. Langan and Y. Tadesse, "Low cost robotic hand that senses heat and pressure," in *2017 ASEE Gulf-Southwest Section Annual Conference*, 2017.
- [280] E. Ramsden, *Hall-effect sensors: theory and application*. Newnes, 2011.
- [281] H.-K. Lee, J. Chung, S.-I. Chang, and E. Yoon, "Normal and shear force measurement using a flexible polymer tactile sensor with embedded multiple capacitors," *Journal of Microelectromechanical Systems*, vol. 17, no. 4, pp. 934–942, 2008.

- 
- [282] B. L. Hutchings, A. R. Grahn, and R. J. Petersen, "Multiple-layer cross-field ultrasonic tactile sensor," in *Robotics and Automation, 1994. Proceedings., 1994 IEEE International Conference on*. IEEE, 1994, pp. 2522–2528.
- [283] G. Milighetti, T. Emter, H.-B. Kuntze, D. Bechler, and K. Kroschel, "Combined visual-acoustic grasping for humanoid robots," in *Multisensor Fusion and Integration for Intelligent Systems, 2006 IEEE International Conference on*. IEEE, 2006, pp. 1–6.
- [284] R. Dahiya, "Piezoelectric tactile sensors," *Wiley Encyclopedia of Electrical and Electronics Engineering*, 2015.
- [285] J. Wheeler, K. Bark, J. Savall, and M. Cutkosky, "Investigation of rotational skin stretch for proprioceptive feedback with application to myoelectric systems," *IEEE Transactions on Neural Systems and Rehabilitation Engineering*, vol. 18, no. 1, pp. 58–66, 2010.
- [286] K. Bark, J. Wheeler, P. Shull, J. Savall, and M. Cutkosky, "Rotational skin stretch feedback: A wearable haptic display for motion," *IEEE Transactions on Haptics*, vol. 3, no. 3, pp. 166–176, 2010.
- [287] A. Akhtar, M. Nguyen, L. Wan, B. Boyce, P. Slade, and T. Bretl, "Passive mechanical skin stretch for multiple degree-of-freedom proprioception in a hand prosthesis," in *International Conference on Human Haptic Sensing and Touch Enabled Computer Applications*. Springer, 2014, pp. 120–128.
- [288] M. Marković, L. Engels, M. Schweisfurth, S. Došen, D. Wüstefeld, and D. Farina, "Does sensory feedback in prosthetic hands provide functional benefits in daily activities of amputees?" in *Converging Clinical and Engineering Research on Neurorehabilitation II*. Springer, 2017, pp. 589–593.
- [289] "Southampton hand assessment procedure (shap)," University of Southampton, 2 2018.
- [290] "NASA task load index," NASA, 2 2018.
- [291] P. Huguelet, A. Zanello, and R. Nicastro, "A study of visual and auditory verbal working memory in schizophrenic patients compared to healthy subjects," *European Archives of Psychiatry and Clinical Neuroscience*, vol. 250, no. 2, pp. 79–85, 2000.
- [292] M. R. Yuce, S. W. Ng, N. L. Myo, J. Y. Khan, and W. Liu, "Wireless body sensor network using medical implant band," *Journal of Medical Systems*, vol. 31, no. 6, pp. 467–474, 2007.
- [293] H. Alemdar and C. Ersoy, "Wireless sensor networks for healthcare: A survey," *Computer networks*, vol. 54, no. 15, pp. 2688–2710, 2010.
- [294] E. Jovanov, A. Milenkovic, C. Otto, and P. C. De Groen, "A wireless body area network of intelligent motion sensors for computer assisted physical rehabilitation," *Journal of NeuroEngineering and rehabilitation*, vol. 2, no. 1, p. 6, 2005.

## Bibliography

---

- [295] “Mems pressure sensor: 260-1260 hpa absolute digital output barometer,” ST Microelectronics, 4 2016, rev. 5.
- [296] V. Peiris, M. Kucera, N. Scolari, A. Vouilloz, and E. L. Roux, “An ultra-low power bluetooth smart integrated solution,” in *CSEM Scientific and Technical Report 2012*, 01 2012, p. 97. [Online]. Available: <http://www.csem.ch>
- [297] P. Cerveri, M. Quinzi, D. Bovio, and C. A. Frigo, “A novel wearable apparatus to measure fingertip forces in manipulation tasks based on mems barometric sensors,” *IEEE transactions on haptics*, vol. 10, no. 3, pp. 317–324, 2017.
- [298] L. P. Jentoft, Y. Tenzer, D. Vogt, J. Liu, R. J. Wood, and R. D. Howe, “Flexible, stretchable tactile arrays from mems barometers,” in *Advanced Robotics (ICAR), 2013 16th International Conference on*. IEEE, 2013, pp. 1–6.
- [299] M. Zillich and W. Feiten, “A versatile tactile sensor system for covering large and curved surface areas,” in *Intelligent Robots and Systems (IROS), 2012 IEEE/RSJ International Conference on*. IEEE, 2012, pp. 20–24.
- [300] Y. Tenzer, L. P. Jentoft, and R. D. Howe, “The feel of mems barometers: Inexpensive and easily customized tactile array sensors,” *IEEE Robotics & Automation Magazine*, vol. 21, no. 3, pp. 89–95, 2014.
- [301] “Tango black,” <http://www.stratasys.com/materials/search/tango>, accessed: 2018-01-29.
- [302] *MTS Criterion C42*, MTS, 1 2018. [Online]. Available: <https://www.mts.com/en/products/producttype/test-components/grips-fixtures-accessories/load-cells-force-transducers/index.htm>
- [303] H. Huang, T. Li, C. Antfolk, C. Enz, J. Justiz, and V. M. Koch, “Experiment and investigation of two types of vibrotactile devices,” in *Biomedical Robotics and Biomechatronics (BioRob), 2016 6th IEEE International Conference on*. IEEE, 2016, pp. 1266–1271.
- [304] C. Cipriani, M. Controzzi, and M. C. Carrozza, “The SmartHand transradial prosthesis,” *Journal of NeuroEngineering and Rehabilitation*, vol. 8, no. 1, p. 29, May 2011.
- [305] C. Sollerman and A. Ejeskär, “Sollerman hand function test: a standardised method and its use in tetraplegic patients,” *Scandinavian Journal of Plastic and Reconstructive Surgery and Hand Surgery*, vol. 29, no. 2, pp. 167–176, 1995.
- [306] C. Antfolk, V. Kopta, J. Farserotu, J.-D. Decotignie, and C. Enz, “The WiseSkin artificial skin for tactile prosthetics: A power budget investigation,” in *2014 8th International Symposium on Medical Information and Communication Technology (ISMICT)*, Apr. 2014, pp. 1–4.
- [307] “Touch bionics product catalog,” Touch Bionics, 1 2015, issue No. 1.

- 
- [308] “Ottobock MyoEnergy Integral,” Ottobock, 3 2017.
- [309] “Ottobock VariPlus Speed,” [https://media.ottobock.com/\\_web-site/prosthetics/upper-limb/myoelectric\\_devices/files/prosthesis\\_systems\\_information\\_for\\_practitioners.pdf](https://media.ottobock.com/_web-site/prosthetics/upper-limb/myoelectric_devices/files/prosthesis_systems_information_for_practitioners.pdf), accessed: 2018-01-29.
- [310] “Mpl115a2, miniature i2c digital barometer,” NXP Semiconductor N.V, 2 2013, rev. 9.
- [311] “Cc2640 simplelink bluetooth wireless mcu,” Texas Instrument, 7 2016, rev. B.
- [312] R. C. Carrano, D. Passos, L. C. Magalhaes, and C. V. Albuquerque, “Survey and taxonomy of duty cycling mechanisms in wireless sensor networks,” *IEEE Communications Surveys and Tutorials*, vol. 16, no. 1, pp. 181–194, 2014.
- [313] “2.9g linear long throw servo,” <https://www.spektrumrc.com/Products>, SPEKTRUM, 11 2017.
- [314] “Cylinder type vibration motor with lead wire, 6mm diameter,” <http://shenzhen-ineed.manufacturer.globalsources.com/si/6008842912027/pdtl/Vibration-motors/1044744055/Cylinder-Type-Vibration-Motor.htm>, INEED, 11 2017.
- [315] *Force sensing resistors*, Interlink Electronics, Inc., 1 2018. [On-line]. Available: [https://cdn2.hubspot.net/hubfs/3899023/Interlinkelectronics%20November2017/Docs/Datasheet\\_FSR.pdf](https://cdn2.hubspot.net/hubfs/3899023/Interlinkelectronics%20November2017/Docs/Datasheet_FSR.pdf)
- [316] A. Bicchi, E. P. Scilingo, and D. De Rossi, “Haptic discrimination of softness in teleoperation: the role of the contact area spread rate,” *IEEE Transactions on Robotics and Automation*, vol. 16, no. 5, pp. 496–504, 2000.
- [317] E. P. Scilingo, M. Bianchi, G. Grioli, and A. Bicchi, “Rendering softness: Integration of kinesthetic and cutaneous information in a haptic device,” *IEEE Transactions on Haptics*, vol. 3, no. 2, pp. 109–118, 2010.
- [318] M. A. Srinivasan and R. H. LaMotte, “Tactual discrimination of softness,” *Journal of Neurophysiology*, vol. 73, no. 1, pp. 88–101, 1995.
- [319] A. Kargov, C. Pylatiuk, J. Martin, S. Schulz, and L. Döderlein, “A comparison of the grip force distribution in natural hands and in prosthetic hands,” *Disability and Rehabilitation*, vol. 26, no. 12, pp. 705–711, 2004.



# Huaiqi Huang

Huaiqi.huang@gmail.com  
LinkedIn : [huaiqi.huang](#)



## Work Experience

### **Dialog Semiconductor, Munich, Germany – Analog design internship**

10.2012 – 06.2011 Building device models using Verilog-A to be used in power management chip design simulation.

### **Nanjing University of Science and Technology – Research assistant**

08.2005 – 08.2009

## Education

### **Swiss Federal Institute of Technology (EPFL), Neuchâtel, Switzerland – PhD in microelectronics, project in rehabilitation**

09.2013 – 06.2018 Designing sensory feedback system for upper limb amputees, focusing on human machine interface, biomedical device development, and clinical testing.

### **Swiss Federal Institute of Technology (EPFL), Lausanne, Switzerland – Master in microelectronics**

09.2011 – 06.2013 Trained in analog/mixed signal circuit design and semiconductor processing. Master thesis: 'Design and implementation of 4T APS CMOS image sensors'

### **Nanjing University of Science and Technology – Bachelor in electrical engineering**

09.2011 – 06.2013 Trained in semiconductor modeling, processing, and semiconductor physics. Bachelor thesis: Resolution of GaAs sPhotocathode and Image Intensifier

## Skills

**Technical skills** VHDL, VHDL-AMS, C++, assembler, Java, Groovy, Matlab, R  
Cadence, SPSS, Protel, Altera Quartus II, TetraMAX, SQL  
COMSOL Multiphysics, Materials Studio, ModelSim

**Transferable skills** Time management, interpersonal communication,

**Language** Chineses (Native speaker)  
English (full professional proficiency, TOEFL:110/120, master taught in English)  
German (limited working proficiency)  
French (elementary proficiency)

## Publication List

### Journal paper

Huang, H., Bruschini, C., Antfolk, C., Enz, C., Li, T., Justiz, J., & Koch, V. M. (2018). Automatic hand phantom map generation and detection using decomposition support vector machines. *Biomedical engineering online*, 17(1), 74.

Li, T., Huang, H., Antfolk, C., Justiz, J., & Koch, V. M. (2016). Tactile display on the remaining hand for unilateral hand amputees. *Current Directions in Biomedical Engineering*, 2(1), 399-403.

### Conference paper

Huang, H., Li, T., Bruschini, C., Antfolk, C., Justiz, J., Enz, C., & Koch, V. M. (2018). Design and Evaluation of Miniaturized Solenoid Actuators for Providing Sensory Feedback for Upper Limb Amputee. In *Actuator*, Bremen, Germany.

Ren, J., Li, C., Huang, H., Wang, P., Zhu, Y., Wang, B., & An, K. (2017). Grasping Force Control of Prosthetic Hand Based on PCA and SVM. In *Advanced Computational Methods in Life System Modeling and Simulation* (pp. 222-230). Springer, Singapore.

Huang, H., Li, T., Bruschini, C., Enz, C., Justiz, J., Antfolk, C., & Koch, V. M. (2017, September). Multi-modal Sensory Feedback System for Upper Limb Amputees. In *IEEE 2017 New Generation of CAS (NGCAS)* (pp. 193-196). IEEE.

Li, T., Huang, H., Justiz, J., & Koch, V. M. (2016). A miniature multimodal actuator for effective tactile - feedback: design and characterization. In *Proceedings of The 30Th Anniversary Euroensors Conference- Euroensors 2016* (Vol. 168, No. CONF). Elsevier Science Bv.

Huang, H., Li, T., Bruschini, C., Antfolk, C., Justiz, J., Enz, C., & Koch, V. M. (2016). Hybrid Stimulation Device for Providing Sensory Feedback. In *Actuator*, Bremen, Germany.

Huang, H., Li, T., Antfolk, C., Enz, C., Justiz, J., & Koch, V. M. (2016, June). Experiment and investigation of two types of vibrotactile devices. In *2016 6th IEEE International Conference on Biomedical Robotics and Biomechatronics (BioRob)*, (pp. 1266-1271). IEEE.

Huang, H., Li, T., Antfolk, C., Enz, C., Justiz, J., & Koch, V. M. (2016, June). EMG pattern recognition using decomposition techniques for constructing multiclass classifiers. In *2016 6th IEEE International Conference on Biomedical Robotics and Biomechatronics (BioRob)*, (pp. 1296-1301). IEEE.

Huang, H., Antfolk, C., Enz, C., Justiz, J., Li, T., & Koch, V. M. (2014, October). Automatic Hand Phantom Map Detection Methods. In *2015 IEEE Biomedical Circuits and Systems Conference (BioCAS)*, (pp. 604-607). IEEE.

Huang, H., Enz, C., Grambone, M., Justiz, J., Li, T., Ünsal, O., & Koch, V. M. (2014, October). Data fusion for a hand prosthesis tactile feedback system. In *2014 IEEE Biomedical Circuits and Systems Conference (BioCAS)*, IEEE.

